OPTIMAL CONTROL BASED METHOD FOR DESIGN AND ANALYSIS OF CONTINUOUS DESCENT ARRIVALS

A Thesis
Presented to
The Academic Faculty

by

Sang Gyun Park

In Partial Fulfillment
of the Requirements for the Degree
Doctor of Philosophy in the
School of Aerospace Engineering

Georgia Institute of Technology
December 2014

OPTIMAL CONTROL BASED METHOD FOR DESIGN AND ANALYSIS OF CONTINUOUS DESCENT ARRIVALS

Approved by:

Professor John-Paul B. Clarke, Advisor
School of Aerospace Engineering
Georgia Institute of Technology

Professor Eric Feron
School of Aerospace Engineering
Georgia Institute of Technology

Professor J.V.R. Prasad
School of Aerospace Engineering
Georgia Institute of Technology

Professor Panagiotis Tsiotras
School of Aerospace Engineering
Georgia Institute of Technology

Professor Magnus Egerstedt
School of Electrical and Computer Engineering
Georgia Institute of Technology

Date Approved: August 2014

To my family

ACKNOWLEDGEMENTS

First and foremost, I would like to thank my advisor, Professor John-Paul B. Clarke, for giving me the opportunity to work in Air Transportation Lab with an excellent environment for research and study. It always have been enjoyable to work in ATL under his great and clear guidance with keen insight and knowledge.

I also would like to thank my thesis committee; Professor Eric Feron, Professor Panagiotis Tsiotras, Professor J.V.R. Prasad, and Professor Magnus Egerstedt. Their invaluable comments and guidance helped me to enhance my insights and knowledge on optimal control and air transportation systems.

I would like to especially thank Jim Brooks. He taught me the practical knowledge on the air traffic operation, English and life wisdom to make me a better engineer and human being.

Next, I want to thank my ATL fellows; Bosung Kim, Suwon Bae, Jong Wook Park, Dr. Adan Vela, Dr. Clayton Tino, Dr. Evan McClain, Isacc Robenson, Anwesha Roy Paladhi, Harold Nikoue, Gustavo Lee, Parth Shah, Hasan Tawab. I have enjoyed conversation and discussion on various topics with them. I would like to thank my Korean friends for helping me a lot whenever I need. They made my Gatech life rich and happy. Especially I want to thank Bosung Kim and Dr. Jongki Moon for their tremendous help when I started the new life in 2009.

Last but the most, my thanks go to my family. I would like to thank my parents and parents in law for their love and support. I also would like to especially thank my wife, Hye Jung, for always being beside me and supporting me through the most challenging and exciting journey in my life.

TABLE OF CONTENTS

LIST OF TABLES

LIST OF FIGURES

LIST OF ABBREVIATIONS

ATC	Air Traffic Control
CAS	Calibrated Airspeed
CDA	Continuous Descent Arrival
CTA	Controlled Time of Arrival
DOC	Direct Operating Cost
EDA	Efficient Descent Advisor
EIS	Environmental Impact Statement
FAA	Federal Aviation Administration
FMS	Flight Management System
FPA	Flight Path Angle
IAS	Indicated Airspeed
LNAV	Lateral Navigation
NASA	National Aeronautics and Space Administration
RNAV	Area Navigation
ROD	Rate of Descent
RTA	Required Time of Arrival
STA	Scheduled Time of Arrival
STAR	Standard Terminal Arrival Route
TAS	True Airspeed
TASAT	Tool for Analysis of Separation and Throughput
TBO	Trajectory Based Operation
TMA	Traffic Management Advisor
TOD	Top of Descent
TRACON	Terminal Radar Approach Control
VNAV	Vertical Navigation

SUMMARY

The purpose of the Next Generation Air Transportation System (NextGen) is to enhance the efficiency and safety of air transportation and reduce the associated environmental impacts such as noise and aircraft engine gaseous emissions. One promising procedure for reducing these environmental impacts is the Continuous Descent Arrival (CDA), in which aircraft, at or near idle thrust, descend from their cruise altitude to their Final Approach Fix (FAF) without leveling off. CDA flight trials and implementations at several airports indicate that CDAs also provide fuel and flight time savings.

The first operational CDA in the U.S. was introduced in 2007 at the Los Angeles International Airport (LAX) where CDAs are flown at all times by aircraft arriving from the East. Since then, CDA/OPD procedures have been added to 28 airports. However, at many of these airports, usage of CDAs has to date been limited to periods when air traffic controllers are not required to achieve near minimum separation. This is in large part due to the reduction in runway throughput that results when controllers add buffers to compensate for their inability to accurately predict the trajectory variations of the different aircraft types in stochastic wind conditions.

The task of predicting the future trajectory of aircraft would be significantly easier if all aircraft were able to perform their CDA over the same duration. Such a procedure, a specific instantiation of the proposed concept of Trajectory Based Operations (TBO), requires that each aircraft be given Required Time of Arrival (RTA) and duration constraints, and that the Flight Management System (FMS) onboard the aircraft be able to generate a trajectory that satisfies the given constraints.

In this thesis, a novel design and analysis method for CDA is proposed. The methodology is developed within the context of an optimal control framework as follows.

The CDA trajectory optimization problem is first formulated as a multi-phase optimal control problem with several constraints (including flight envelope and flap setting constraints, and constraints due to FAA regulations), and optimality is evaluated with respect to two performance indices: flight time and fuel consumption.

An en route CDA trajectory generation algorithm is then developed for minimizing the environmental impact given an RTA at a meter fix. The trajectory generation method in the FMS is modeled as a hybrid system that has both a continuous state and a discrete state. Therefore, the optimal trajectory generation problem is the optimal control problem of the hybrid system, and this problem can be solved using a sequential method that performs the mode sequence estimation and parameter optimization, sequentially. The semi-analytic solution with the simplified aircraft dynamics is obtained from the necessary conditions of the path constrained optimal control problem. The optimal switching structure of the semi-analytic solution is used for the mode sequence estimation, thereby reducing the computational time significantly.

Finally, a performance-bound analysis framework is developed using optimal control techniques to help controllers or traffic management advisors make a feasible schedule for CDA operations at a meter fix. This tool is then used to analyze a feasible time range for a wide variety of aircraft and propose a single flight time strategy for the application of CDA in high traffic conditions. Using simulation, we show that this strategy guarantees conflict free flight during the descent phase.

CHAPTER I

INTRODUCTION

1.1 Continuous Descent Arrival Procedures

The purpose of Next Generation Air Transportation System (NextGen) is to enhance the efficiency and safety of the future air transportation system while reducing the environmental impact such as noise and aircraft engine gaseous emissions. One promising approach to reduce the environmental impact is the Continuous Descent Arrival (CDA); where arriving aircraft descend from cruise altitude to a Final Approach Fix (FAF) without level flight segments and with the engines operating at or near flight idle thrust [11]. Level flight segments occur frequently during the arrival and approach phases as aircraft are vectored by Air Traffic Control(ATC). These segments serve two purposes; the use of speed control to manage the required separation, and to create a "bridge" for the routing of departing aircraft. Since an increase in engine power or thrust is needed to maintain level flight, a CDA can reduce the environmental impacts of both noise and emissions which has been demonstrated by analysis and flight demonstrations. CDA procedures are typically constructed by modifying the vertical descent path along an existing Standard Terminal Arrival Route (STAR) lateral path. These lateral paths are normally chosen for the CDA to prevent the possibility of generating a requirement for an Environmental Impact Statement (EIS). The vertical path is constructed with altitude and speed constraints, where necessary, along the lateral path waypoints to allow the aircraft to continuously descend with the engines at or near flight idle power or thrust. The initial flight trials evaluating CDA procedures were conducted during late night landing operations by UPS at Louisville International Airport (KSDF) in 2004[13]. This flight trial, leveraging the capability of the Flight Management System (FMS), proved the stated benefits of a CDA procedure. Following the flight demonstration at KSDF, additional flight trials by several researchers also confirmed the environmental benefits of CDA at several airports: Los Angeles (KLAX) in 2007[12], Atlanta (KATL) and

Miami (KMIA) in 2008[65].

Despite the proven benefits of CDA procedures, implementation of the procedure, with the exception of KLAX, has been limited to relatively low density arrival traffic. The problem is, with existing airborne and ground equipage, managing the required aircraft spacing while they are continuously descending and decelerating as they approach the runway. In addition, there are variations in the CDA vertical profile that are the result of differences in aircraft specific aerodynamic characteristics, wind, weight, and pilot response times to flap extensions as the aircraft decelerates. These trajectory variations are problematic for ATC with regard to maintaining the separation minimums, and additional spacing is applied which degrades the runway throughput. Both the required airborne and ground equipage and their capability are the subject of a number of research efforts.

1.2 Trajectory Based Operations

Trajectory Based Operations (TBO) is also a NextGen initiative and accurate trajectory prediction is one of the key technologies required to address the ATC problem of managing minimum separation for CDAs. Using TBO for CDA consists of identifying one of the waypoints along the CDA ground path as a metering fix and determining the spacing at the metering fix that would result in the arrival stream of aircraft successfully flying a CDA while maintaining the required minimum spacing or separation.

1.2.1 Separation Management

Several decision support tools for ATC have been developed to support TBO. Ren and Clarke[55, 56] developed the Tool for Analysis of Separation and Throughput (TASAT), that is used to determine the required minimum separation between leading and trailing aircraft, when the leading aircraft is at a metering fix, to successfully conduct CDA. TASAT is a high fidelity descent analysis model that uses proprietary aircraft performance data and embedded FMS logic to construct a descent path. The TASAT airframe/engine specific analysis begins with a chosen cruise altitude and lateral path to a terminating waypoint. Numerous descent paths are generated by using a Monte Carlo simulation to randomly vary the aircraft weight and wind derived from the airport historical data for each descent. In addition to weight and wind, a pilot response time is injected to vary the time associated with flap extension. With the descent analysis complete, TASAT then determines the required spacing, with a chosen confidence interval, at a selected metering point along the lateral path to result in the regulatory minimum spacing at the runway threshold. TASAT has been validated by the flight test demonstrations described above and during full flight simulator testing in support of CDA development in the United States and Europe [59, 60, 10].

NASA Ames research center developed the Traffic Management Advisor (TMA) that produces a Required Time of Arrival (RTA) at a metering fix to achieve a target separation[66]. NASA Ames also developed the Efficient Descent Advisor (EDA) that combines a ground trajectory generation tool with a specific RTA[15]. This combination was used to demonstrate the proposed tailored arrival concept for flight trials at San Francisco airport (KSFO) in 2007[14].

1.2.2 Trajectory Generation

Another key component of TBO is the capability of the FMS to generate a 4D trajectory for the anticipated arrival and approach operation. In this scenario, ATC will transmit to inbound aircraft an RTA to a metering fix, determined by analysis from TMA, TASAT, or a similar tool, that will result in the arrival stream maintaining the required minimum separation for the intended flight path to the runway threshold. Therefore, optimal trajectory generation subject to a given RTA in the FMS is essential for maximizing the benefits associated with the successful implementation of CDAs.

Many researchers have applied optimal control techniques to the trajectory generation problem of the arrival and approach phase because trajectories generated via the optimal control problem provide both feasible solutions that satisfy various constraints, and optimal trajectories with respect to various performance indices such as: time and fuel cost[18, 64, 8, 9, 62, 49, 48], energy consumption cost[76], emission cost[73], maximum glide[22] and noise cost[69].

In the 1980s, to reduce the computational time, most researchers replaced aircraft dynamics equations with simplified energy state equations with energy as the independent variable instead of time[18, 64, 8, 9, 62]. Erzberger and Lee[18] proposed a specified range optimal trajectory by using Direct Operational Cost (DOC) combining time and fuel cost as a performance index. Sorrenson and Waters[64] addressed a fuel optimal trajectory problem with a fixed arrival time and analyzed a time delay performance by using a negative time cost. Burrows[8] converted a fixed arrival time fuel optimal control problem to a free final time DOC problem with an unknown time cost. In this way, they solved the DOC optimal control problem with a one time cost parameter, which should be determined to satisfy the arrival time constraint. Chakravarty[9] used a singular perturbation method as well as an energy state approximation to investigate the sensitivity of fuel optimal trajectories to wind. Shultz[62] addressed a three dimensional minimum time problem with a fixed initial and final point. These approaches which used an energy state approximation have advantages in terms of calculation time and computational load. However, since the model is oversimplified and some constraints required in an actual procedure are not considered, the resulting trajectories do not have the accuracy for application in real air traffic situations.

Since the early 2000s, several studies have been conducted to produce an optimized trajectory for minimizing the environmental impact. Visser and Wijnen [69] researched an optimized noise abatement trajectory. They formulated the problem as a multi-phase optimal control problem and solved it by using a chosen direct numerical method. However a fixed RTA at a meter fix was not taken into account. Wu and Zhao [73] assumed a multi-segmented descent trajectory and optimized the segments using fuel and emission costs. Few researchers have used the CDA trajectory structure assuming flight idle thrust [22, 49, 48]. Franco and et al. [22] solved a maximum descent range problem by a singular arc analysis. Zhao and Tsiotras [76] proposed an optimal speed profile generation method for minimizing energy for a given RTA and path using a singular arc analysis. However, they did not consider factors such as wind and flap extensions.

Another proposed development for producing an RTA is one in which a descent trajectory is constructed of varying flight segments which can be generated with the FMS Vertical

Navigation (VNAV) capability[75, 63]. In this development, multiple segments were created by switching between the various available FMS mode capabilities (flight path angle, vertical speed, vertical path, etc.). While the resulting flight path segments and subsequent RTA could be generated by this iterative technique, it should be noted that these trajectories were feasible, not optimal.

1.3 Thesis Objectives

To achieve the environmental goals of NextGen by enabling CDA arrivals, there is a need to expand the use of the procedure into increasing traffic conditions. For this purpose, it is necessary to resolve the existing barriers of CDA implementation, and in particular, the inherent variation in the CDA trajectories which contribute to the separation issue. Furthermore, to enhance traffic efficiency with TBO, the FMS must have the capability of commanding an optimal trajectory with a given RTA in order to achieve the CDA benefits. The objective of this thesis is to achieve the following:

- Maximize the benefits of a CDA by formulating the trajectory optimization problem with respect to the various performance indices.
- With existing FMS capability, develop a fast trajectory optimization algorithm with consideration of an RTA constraint.
- Develop a tool to analyze the performance bounds of a CDA trajectory considering varying aircraft types and wind conditions for TBO.
- Develop a time based CDA operation concept that can be implemented in dense traffic conditions.

By achieving the goals above, 1) an optimal 4D trajectory can be generated in the FMS, and hence the fundamental requirement for a time based CDA operation can be achieved. 2) Without degrading the runway throughput, a feasible time scheduling at a meter fix can be established by the analysis of the performance bounds associated with a CDA 3) Ensure a conflict free descent flight path can be achieved.

1.4 Thesis Outline

This thesis consists of two major parts. Part 1 consists of Chapters 2, 3, and 4 describing the CDA optimum trajectory problem. Part 2 is the development of a CDA performance bound analysis tool for a time based CDA.

Chapter 2 formulates the CDA trajectory optimization problem as a multi-phase optimal control problem, considering a number of constraints such as FAA regulations, flight envelope protection, and flap extension or schedule speeds. In Chapter 3, since the FMS trajectory generation has a finite automaton, which is a directed graph representing the mode transitions, and the aircraft has continuous dynamics; trajectory generation with the FMS can be modeled as a hybrid system. This chapter also includes an algorithm to solve this hybrid optimal control problem. Chapter 4 analyzes the optimal CDA solution using the necessary condition of the optimality. Based on this analysis, we derive an algorithm for the optimal switching structure and by using this algorithm we discuss a means of reducing the computational time for the hybrid optimal control problem algorithm presented in Chapter 3.

The second major part, Chapter 5, proposes a framework for the trajectory performance bound analysis using the optimal control technique presented. We analyze the performance bound of a defined aircraft fleet mix using the proposed framework. Based on the analyses, we propose a concept for a time based CDA operation which guarantees a conflict free descent during the procedure. In this manner, we can transfer the issue of runway separation to the cruise portion of the flight, which is much easier to resolve for ATC.

CHAPTER II

UNCONSTRAINED CDA TRAJECTORY OPTIMIZATION

2.1 Introduction

In this chapter, we address the vertical trajectory optimization problem for Continuous Descent Arrival (CDA) procedures. Since the successful CDA provides flight time and fuel savings[13], we solve the minimum time and minimum fuel CDA to maximize the benefits of the CDA. To this end, we first investigate the CDA trajectory structure of current CDA procedures. Based on the structure of the CDA trajectory, we then formulate the unconstrained CDA trajectory optimization problems with respect to the performance indices of flight time and fuel consumption. An ‘unconstrained’ CDA is a defined flight path than has no altitude or speed constraints other than those for the terminating waypoint of the procedure. Therefore, the ‘unconstrained’ optimal CDA trajectory provides the lower bound performances in terms of flight time and fuel.

The final formulation for the CDA trajectory optimization problem is a multi-phase optimal control problem with a fixed range and several constraints for both operating conditions and the speed bound. The trajectory is optimized from cruise altitude to the intercept of the Instrumental Landing System (ILS) glide slope. By dividing the optimal trajectory into two flight segments, cruise and descent, we can simultaneously obtain both the position of the Top of Descent (TOD) and the subsequent optimal descent path. Furthermore, we develop suboptimal trajectories for a VNAV CDA based on the optimal trajectory results. These VNAV CDA profiles can be implemented in the onboard FMS computer without additional equipment.

The remainder of this chapter is organized as follows. In section 2.2, we derive the equations of motion of the aircraft and formulate a multiple-phase Bolza optimal control problem for CDA. In section 2.3, we provide numerical optimization results and sensitivity analyses of the optimal trajectories for a B737-500 and B767-400. In section 2.4, we propose two suboptimal VNAV CDA trajectories, which are constructed using the existing VNAV descent algorithms in the FMS: flight idle thrust constant CAS/MACH descent, constant rate of descent, and constant flight path angle. The conclusions of this study are summarized in section 2.5.

2.2 Optimal Control Problem Formulation

Initially we derive a point mass flight dynamics model. Then, we introduce the CDA trajectory structure based on the flight trials of a CDA. Based on the CDA structure, we formulate a CDA trajectory optimization problem with various path constraints for the flight envelope protection, passenger comfort, and regulations of the Federal Aviation Administration (FAA).

2.2.1 Flight Dynamic Model

The dynamic model of the aircraft greatly influences the optimization results, and an accurate model is necessary to obtain realistic results. While a high order dynamics model can capture accurate aircraft behaviors, a simplified dynamics model, on the other hand, can reduce computational time by reducing the order of equations. After considering this trade-off, we decided to use a 3D point mass flight dynamics model, in which moment equations are ignored by assuming that the attitude of the aircraft is controlled by an autopilot. Therefore, only force equations are used to describe the aircraft's vertical and lateral movement or motion.

The aircraft's equations of motion are derived by using the following right-hand coordinate frames:

- North-East-Down (NED) frame: the origin of this frame is the runway threshold with the North-East plane tangent to the Earth's surface at the origin of the frame. The X axis points to the North, the Y axis points to the East, and the Z axis points downward.

- Relative wind frame: the origin of this frame is the aircraft center of gravity. The X_w axis points in the direction of the true airspeed.

The relative wind frame is obtained by three consecutive 3-2-1 rotations from the NED frame. The 3-2-1 rotation angles from the NED frame to the relative wind frame are aerodynamic heading angle χ, aerodynamic flight path angle γ, and aerodynamic roll angle μ, respectively. The resulting rotation matrix from the NED frame to the relative wind frame is

$$\mathbf{R_W} = \begin{bmatrix} \cos\gamma\cos\chi & \cos\gamma\sin\chi & -\sin\gamma \\ \sin\mu\sin\gamma\cos\chi - \cos\mu\sin\chi & \sin\mu\sin\gamma\sin\chi + \cos\mu\cos\chi & \sin\mu\cos\gamma \\ \cos\mu\sin\gamma\cos\chi + \sin\mu\sin\chi & \cos\mu\sin\gamma\sin\chi - \sin\mu\cos\chi & \cos\mu\cos\gamma \end{bmatrix} \tag{1}$$

To simplify the dynamics model, we use the following assumptions: 1) The wind has no vertical component in the NED frame. 2) The sideslip angle β is zero. 3) The thrust vector is in the same direction as the true airspeed vector. 4) The mass of the aircraft remains constant during the arrival procedure. Assumption 1) means that the wind speed vector in the NED frame can be expressed as follows:

$$\mathbf{V_W} = \begin{bmatrix} U_W \\ V_W \\ 0 \end{bmatrix} \tag{2}$$

The zero side slip angle in assumption 2) indicates a coordinated flight, during which the Y component of the aerodynamic force in the relative wind frame is zero. Assumption 4), which results in us ignoring the effect mass changes, is quite reasonable since the fuel consumption during the arrival procedure is below 0.5% of the total mass[13]. The velocity vector is the vector sum of the true airspeed and wind speed vectors as

$$\mathbf{V} = \mathbf{V_T} + \mathbf{V_W} = \mathbf{R}_\mathbf{W}^T \mathbf{V}_\mathbf{T}^\mathbf{W} + \mathbf{V_W}. \tag{3}$$

The angular velocity expressed in the relative wind frame is

$$\omega^\mathbf{W} = \begin{bmatrix} \dot{\mu} - \dot{\chi}\sin\gamma \\ \dot{\gamma}\cos\mu + \dot{\chi}\cos\gamma\sin\mu \\ -\dot{\gamma}\sin\mu + \dot{\chi}\cos\gamma\cos\mu \end{bmatrix}. \tag{4}$$

The time derivative of true airspeed expressed in the relative wind frame is:

$$\dot{\mathbf{V}}_{\mathbf{T}}^{W} = \frac{d}{dt}(V_T \mathbf{w_1}) = \dot{V}_T \mathbf{w_1} + V_T \dot{\mathbf{w}}_{\mathbf{1}} = \dot{V}_T \mathbf{w_1} + \omega^W \times \mathbf{V}_{\mathbf{T}}^{W}$$

$$= \dot{V}_T \begin{bmatrix} 1 \\ 0 \\ 0 \end{bmatrix} + V_T \begin{bmatrix} 0 \\ -\dot{\gamma}\sin\mu + \dot{\chi}\cos\gamma\cos\mu \\ -\dot{\gamma}\cos\mu - \dot{\chi}\cos\gamma\sin\mu \end{bmatrix}. \tag{5}$$

Hence,

$$\dot{\mathbf{V}}^{W} = \dot{\mathbf{V}}_{\mathbf{T}}^{W} + \dot{\mathbf{V}}_{\mathbf{W}}^{W} = \frac{1}{m}\sum \mathbf{F}^{W} = \frac{1}{m}(\mathbf{F}_{\mathbf{A}}^{W} + \mathbf{T}^{W} + m\mathbf{g}^{W}), \tag{6}$$

where $\mathbf{F_A}$ and $\mathbf{T}$ are the aerodynamic force and thrust vector, respectively. Assumptions 1), 2) and 3), can be used to rewrite Eq. (6) in the relative wind frame as

$$\dot{\mathbf{V}}_{\mathbf{T}}^{W} = \frac{1}{m}\left(\begin{bmatrix} T - D \\ 0 \\ -L \end{bmatrix} + \mathbf{R_W} \begin{bmatrix} 0 \\ 0 \\ mg \end{bmatrix} \right) - \mathbf{R_W} \begin{bmatrix} \dot{U}_W \\ \dot{V}_W \\ 0 \end{bmatrix}. \tag{7}$$

By combining Eq. (5) and Eq. (7), we obtain the equations of motion for the aircraft. In addition, by using Eq. (3) and (4), we obtain the navigation equations. Finally, the equations of motion of aircraft are expressed as follows:

$$\dot{V}_T = \frac{1}{m}(T - D) - g\sin\gamma - \cos\gamma(\dot{U}_w\cos\chi + \dot{V}_w\sin\chi) \tag{8}$$

$$\dot{\gamma} = \frac{1}{mV_T}L\cos\mu - \frac{1}{V_T}g\cos\gamma + \frac{\sin\gamma}{V_T}\left(\dot{U}_w\cos\chi + \dot{V}_w\sin\chi\right) \tag{9}$$

$$\dot{\chi} = \frac{1}{mV_T\cos\gamma}L\sin\mu + \frac{1}{V_T\cos\gamma}\left(\dot{U}_w\sin\chi - \dot{V}_w\cos\chi\right) \tag{10}$$

$$\dot{x} = V_T\cos\gamma\cos\chi + U_w \tag{11}$$

$$\dot{y} = V_T\cos\gamma\sin\chi + V_w \tag{12}$$

$$\dot{h} = V_T\cos\gamma \tag{13}$$

Combining Eq. (11) and (12), we obtain the following along track distance equation:

$$\dot{x}_s = \sqrt{\dot{x}^2 + \dot{y}^2} \tag{14}$$

In the above equations of motion, we define state $\mathbf{x} = [V_T \quad \gamma \quad \chi \quad x_s \quad h]^T$, and control input $\mathbf{u} = [L \quad T \quad \mu]^T$.

To reduce the order of the state and control variables for computational effectiveness, we add the following assumption on the lift force:

$$L = \frac{mg\cos\gamma}{\cos\mu}. \tag{15}$$

From Eq. (15), the first two terms in Eq. (9) are canceled, and hence only the third term remains. Since the flight path angle is small ($sin\gamma \approx \gamma$), and the time derivative of the wind is divided by V_T, which is much larger than $\dot{U}_w$ and $\dot{V}_w$, γ has very slow dynamics. Hence, we can neglect the flight path angle and the heading angle dynamics.

Lateral path of CDA procedures are determined by Standard Terminal Arrival Route (STAR). Therefore, the aerodynamic heading angle can be calculated using the lateral path, wind profile, and true airspeed. Using this information, we calculate the aerodynamic roll angle and ignore the aerodynamic heading angle dynamics. Finally, we obtain the order reduced equations of motion as Eq. (8), (13), and (14) for a vertical profile optimization with reduced state $\mathbf{x} = [V_T \quad x_s \quad h]^T$ and a newly defined control input $\mathbf{u} = [T \quad \gamma]^T$.

2.2.2 CDA Trajectory Structure

In this chapter, the flight range covers some portion of the cruise segment, which is from an initial waypoint to the TOD, and a flight idle descent segment, which is from the TOD to IAF as shown in Figure 1. In the first segment, which is the cruise segment, it is assumed that the aircraft flies at its cruise altitude at a constant speed. In order to get the optimal TOD point, the initial waypoint should be far enough from the runway threshold, and hence some range of cruise segment should be included. The reason for this condition follows lemma 2.1. The fixed range d_{max} is defined as the along track distance of the initial waypoint on the defined lateral path to the runway threshold. The second segment is from the TOD point to a final point, in other words, the termination point of the CDA procedure. In this segment, the aircraft descends continuously at flight idle thrust, and flaps are extended in accordance with the aircraft specific flap speed schedule as specified by the airframe manufacturer. While the maximum and minimum airspeeds for each flap setting are defined to prevent any structural damage and provide a stall margin respectively, the flap extension speed can be optimized within the speed bound of two adjacent flap settings[31].

However, in this chapter, to reflect what is done in actual operation, we use a specific flap extension speed within the speed bound for each flap extension, as is typically the case in commercial air carrier operations.

Since the C_D varies with flap setting, the aircraft dynamics changes, and it is therefore necessary to distinguish the phase based on flap setting. In addition, an interior point constraint is required due to the FAA speed limitation, which limits aircraft to an indicated air speed of 250 knots at or below 10,000 ft. In order to handle such an interior point constraint, it is necessary to distinguish the phase before and after the interior point constraint even though flaps are not extended. For this reason, as shown in Figure 1, the second segment is divided into several separate phases. The first phase is from the TOD point to an altitude of 10,000 ft. Subsequent phases start from the 10,000 ft altitude and are separated at the points where the aircraft reaches each required flap extension speed. Each segment of flap extension and its associated speed depends on the aircraft type and weight. The final phase terminates upon the aircraft reaching the final point of the CDA procedure.

An example of the required phases for three segments of flap extension is shown in Fig. 1. According to the segment and phase split in Fig. 1, we can define the performance index and various constraints to formulate a CDA trajectory optimization problem.

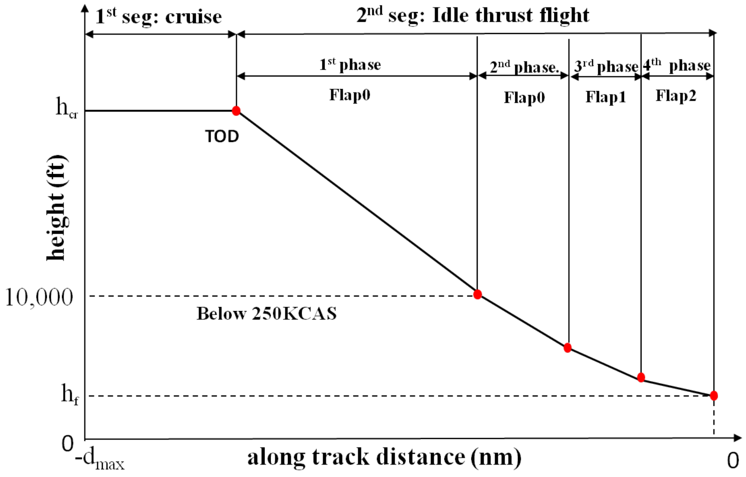

Figure 1: Phase condition of CDA trajectory optimization

2.2.3 Multi-phase Optimal Control Problem Formulation

A multi-phase optimal control problem formulation may be used to obtain both the optimal TOD point and the optimal descent vertical profile of a CDA. In general, the trajectory optimization can be formulated as a multi-phase continuous Bolza optimal control problem[4]. To obtain a realistic trajectory, we consider several practical constraints such as the speed limitation of FAA regulation 91.117 and aircraft operating constraints including their flap speed schedule. Including all practical constraints in the optimal control problem for a CDA requires a multi-phase continuous Bolza optimal control problem formulation. The general formulation of multi-phase optimal control problem is as follows:

$$J = \sum_{p=1}^{N} \left[\Phi^{(p)}(x_0^{(p)}, t_0^{(p)}, x_f^{(p)}, t_f^{(p)}) + \int_{t_0^{(p)}}^{t_f^{(p)}} L^{(p)}(x^{(p)}, u^{(p)}, t) dt \right] \tag{16}$$

subject to the dynamic constraint

$$\dot{x}^{(p)} = f^{(p)}(x^{(p)}, u^{(p)}, t) \tag{17}$$

subject to the event constraint of each phase

$$\phi_{min}^{(p)} \leq \phi(x_0^{(p)}, t_0^{(p)}, x_f^{(p)}, t_f^{(p)}) \leq \phi_{max}^{(p)} \tag{18}$$

subject to the path constraint

$$g_{min}^{(p)} \leq g^{(p)}(x^{(p)}, u^{(p)}, t) \leq g_{max}^{(p)} \tag{19}$$

subject to phase link constraint

$$P^{(s)}(x_f^{(p-1)}, t_f^{(p-1)}, x_0^{(p)}, t_0^{(p)}) = 0 \tag{20}$$

where N is the number of phases; $\Phi^{(p)}$ and $L^{(p)}$ are the Mayer cost and Lagrangian of the p^{th} phase, respectively. The detailed description of each component in Eq. (16) $\sim$ (20) will be explained in the subsequent subsections.

2.2.3.1 Performance Index

CDA procedures provide significant benefits relative to a conventional arrival/approach with level flight segments. In addition to the noise reduction, CDA procedures enable reductions in fuel consumption and flight time[13]. To maximize the benefits of a CDA, fuel consumption and flight time for the fixed range CDA were selected as the performance indices. Through the thesis, the wind is assumed to be a function of altitude, which means that wind speed is constant at the same altitude with regardless of the lateral position. From this assumption, the performance indices can be expressed as the following simple formulations:

- Flight time performance index

$$\begin{aligned} J &= \Phi^{(1)}(x_s^{(1)}(t_0), V_t{}^{(1)}(t_0)) + t_f^{(N)} \\ &= \underbrace{\left(x_s^{(1)}(t_0) - d_{\max}\right)/V_G^{(1)}}_{1^{st}\, segment\, flight\ time} + \underbrace{t_f^{(N)}}_{2^{nd}\, segment\, flight\, time} \end{aligned} \tag{21}$$

- Fuel consumption performance index

$$\begin{aligned} J &= \Phi^{(1)}(x_s^{(1)}(t_0), V_T{}^{(1)}(t_0), h^{(1)}(t_0)) + \sum_{p=1}^{N} \int_{t_0}^{t_f{}^{(p)}} L^{(p)}\, dt \\ &= \underbrace{\dot{f}_{cr,cruise} \times \left(x_s^{(1)}(t_0) - d_{\max}\right)/V_G^{(1)}}_{1^{st}\, segment\, fuel\, consumption} + \underbrace{\sum_{p=1}^{N} \int_{t_0}^{t_f{}^{(p)}} \dot{f}_{cr}^{(p)}\, dt}_{2^{nd}\, segment\, fuel\, consumption} \end{aligned} \tag{22}$$

where d_{max}, $\dot{f}_{cr,cruise}$ and $\dot{f}_{cr}$ are the maximum range, fuel flow rate at cruise at a given cruise speed and idle thrust fuel flow rate, respectively.

As shown in Eq. (21) and (22), both the flight time and fuel consumption performance indices are divided into two parts; one for each segment. The first Mayer cost represents a cost during the cruise segment, and the second cost term is for the flight idle descent segment.

By defining the performance index in two parts as shown above, with the free TOD condition, we can transform a fixed range optimal control problem into a free initial condition optimal control problem. Hence, we can obtain both the optimal TOD point and the optimal vertical trajectory for CDA procedures regarding both minimum flight time and minimum fuel consumption. Furthermore, d_{max} does not affect the optimal TOD point and vertical profile from the following lemma.

Lemma 2.1. *Let's assume that the optimal solution with respect to the performance index in Eq. (21) or (22) exists with a given* d_{max}*, which is farther than* TOD_{opt} *from the runway threshold. Consider the optimal solution pair* (TOD_{opt_1}, u_{opt_1}) *associated with* d_{max_1}*. Then the optimal solution pair* (TOD_{opt_2}, u_{opt_2}) *associated with a different* d_{max_2} *is the same as* (TOD_{opt_1}, u_{opt_1}) *if* d_{max_2} *is farther than* TOD_{opt_1} *from the runway threshold.*

Proof. The TOD $x_s^{(1)}(t_0)$ is limited by d_{max} as

$$d_{max} \leq x_s^{(1)}(t_0). \tag{23}$$

We can express performance indices in Eq. (21) and (22) as follows:

$$J = J_1 + J_2 \tag{24}$$

where J_1 is the Mayer cost and J_2 is the Lagrange cost. J_1 is a function of d_{max} and TOD $x_s^{(1)}(t_0)$. Furthermore, J_1 is expressed as a summation of the TOD term $J_{1,TOD}$ and d_{max} term $J_{1,d_{max}}$. Therefore, J in Eq. (21) and (22) can be rewritten as

$$J = J_{1,d_{max}} + J_2(TOD, u) \tag{25}$$

where, $J_2(TOD, u) = J_{1,TOD} + J_2$. If d_{max} is given, $J_{1,d_{max}}$ is a constant. Therefore, the original problem is equivalent to the problem with $J_2(TOD, u)$, which is independent to d_{max}. For this reason, $(TOD_{opt_2}, u_{opt_2}) = (TOD_{opt_1}, u_{opt_1})$ if both $TOD_{opt_{1,2}}$ are interior points of Eq. (23). □

Remark 1. Lemma 2.1 provides the condition for setting d_{max}. The d_{max} value should be farther from the runway threshold than the optimal TOD. Since x_s at the runway threshold is zero, and d_{max} is always negative, farther from the runway threshold means a smaller value. We should select the smaller value if $d_{max} = TOD_{opt}$.

Remark 2. Lemma 2.1 implies that d_{max} value which satisfies Eq. (23) does not affect the optimal solution. We can select any d_{max} from TOD_{opt} as the starting point of the cruise phase. Therefore, the optimal solution can include all flight segments except climb. However, the initial waypoint must not be too far from the runway threshold because the aircraft mass is assumed to be a constant during the CDA procedure which includes some portion of cruise as shown in Figure 1. Therefore, this fact gives the minimum limit of d_{max} value.

2.2.3.2 Constraints for CDA

In order to obtain a realistic trajectory resulting from the optimal control problem, we should consider operating conditions such as the flap speed schedule, landing gear extension, regulated speed restrictions, and bounded control input constraints. These conditions can be expressed as specific constraints in Eq. (18), (19), and (20). The followings are constraints implemented in the optimal control problem for a CDA.

- Event constraint of each phase

$$d_{max} \le x_s^{(1)}(t_0) \tag{26}$$

$$V_{CAS}^{(1)}(t_f) \le 250\, KCAS \tag{27}$$

$$V_{CAS}^{(p)}(t_f) = V_{F(p)}, \quad \text{for } p = 2, 3, \cdots, N \tag{28}$$

- Path constraints of each phase

$$V_{min,CAS}^{(p)} \le V_{CAS}^{(p)}(t) \le V_{max,CAS}^{(p)} \tag{29}$$

$$\dot{h}_{min} \le \frac{dh}{dt} \le \dot{h}_{max} \tag{30}$$

$$M_{min}^{(p)} \le M^{(p)}(t) \le M_{max}^{(p)} \tag{31}$$

- Phase link constraints

$$\mathbf{x}^{(p-1)}(t_f) = \mathbf{x}^{(p)}(t_0) \tag{32}$$

- Input constraint

$$\gamma_{min} \le \gamma \le \gamma_{max} \tag{33}$$

Equation (27) is formulated to meet the FAA regulation that limits the maximum allowable CAS speed to 250 knots below 10,000 ft. Equation (28) implies that the speed at the end of the phase should be the same as the next flap extension speed, where $V_F(p)$ is the flap extension speed to $F(p)$ setting.

Equation (29) constrains the aircraft CAS to be between the published maximum and minimum flap extension speeds. Equation (30) restricts the descent rate to the maximum established for passenger comfort and the minimum to prevent level flight and also to restrict deceleration performance. Usually, the flight envelope is restricted by both CAS and the Mach number. Therefore, avoiding a violation of the flight envelope can be accomplished by using Eqs. (29) and (31) as path constraints.

To ensure state variables remain continuous, we add the phase link constraint in Eq. (32). Since we assume idle power during the second segment of the optimal trajectory, the aerodynamic flight path angle is the only control input. Equation. (33) imposes a limit on the aerodynamic flight path angle.

2.2.4 Optimal Control Problem

As a result, we can formulate the following unconstrained CDA trajectory optimization problem to be solved in this chapter.

Problem 2.1. (Unconstrained CDA Trajectory Optimization Problem)

$$\begin{aligned}
&\underset{\gamma}{\text{minimize}} \quad J_t \quad \text{or} \quad J_f \\
&\text{subject to} \\
&\qquad \dot{V}_T = \frac{1}{m}(T-D) - g\sin\gamma - \cos\gamma(\dot{U}_w\cos\chi + \dot{V}_w\sin\chi), \\
&\qquad \dot{x}_s = \sqrt{(V_T\cos\gamma)^2 - W_c^2} + W_h \\
&\qquad \dot{h} = V_T\sin\gamma \\
&\qquad \dot{h}_{min} \le \frac{dh}{dt} \le \dot{h}_{max} \\
&\qquad \gamma_{min} \le \gamma \le \gamma_{max} \\
&\qquad V^{(p)}_{min,CAS} \le V^{(p)}_{CAS}(t) \le V^{(p)}_{max,CAS} \quad p = 1,\cdots,N \\
&\qquad M^{(p)}_{min} \le M^{(p)}(t) \le M^{(p)}_{max} \qquad p = 1,\cdots,N \\
&\qquad V^{(1)}_{CAS}(t^{(1)}_f) \le 250\,KCAS \\
&\qquad V^{(p)}_{CAS}(t^{(p)}_f) = V_{F(p)} \qquad p = 2,\cdots,N \quad f = 1,\cdots,N-1 \\
&\qquad \mathbf{x}^{(p-1)}(t^{(p-1)}_f) = \mathbf{x}^{(p)}(t^{(p)}_0) \qquad p = 2,\cdots,N
\end{aligned} \tag{UCP}$$

where the flight range d_{max}, cruise speed, flap extension speed schedule, flight envelope range, and FAF conditions including speed and altitude are given, the final time at the FAF is free.

In this problem, both the cross wind and horizontal wind component are expressed as $W_c = W \sin\lambda$ and $W_h = W \cos\lambda$, where $\lambda = \Psi_w - \psi$. The relationship between true airspeed, ground speed, and wind speed with corresponding angles are depicted in Fig.2.

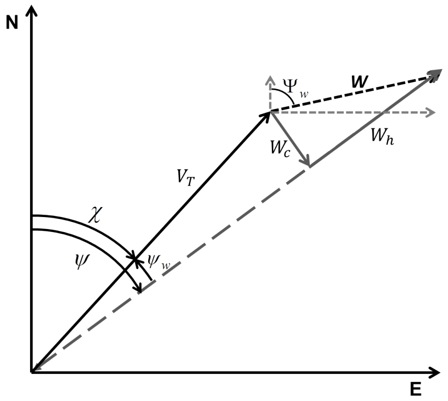

Figure 2: Relations between airspeed, ground speed, and wind speed.

2.3 Trajectory Optimization Results for CDA

In this section, we present the trajectory optimization results of an unconstrained CDA vertical trajectory optimization problem.

To simplify the unconstrained problem (UCP) and focus on only the vertical trajectory, we assume that the lateral path is essentially a straight line and that turns, if any, have very large radii. As a consequence, we ignore the aerodynamic roll angle effect, and hence only consider vertical plane dynamics. Since flight idle thrust is assumed during the second segment of the optimal trajectory, the aerodynamic flight path angle is the only control input in this problem. In the numerical experiment, a constant wind profile is considered. We also assume that wind has the same direction as true airspeed, which means that there is no cross wind component.

As seen in section II, the equations of motion are nonlinear differential equations, both drag and lift force vectors are nonlinear functions of air density, airspeed, and altitude.

Furthermore, many constraints with respect to IAS have a nonlinear relationship with true airspeed[2], making it difficult to solve the problem analytically. For this reason, we use a numerical optimization technique. A pseudospectral method is chosen for this problem to determine an optimal trajectory. A pseudospectral method is one of direct collocation methods in which the state and control input are expressed as piecewise polynomials, and the collocation points are determined by quadrature rules[20, 23, 32]. Using this assumption, we transform the optimal control problem into a nonlinear programming (NLP) problem that already has many efficient solvers. We solve the problems with GPOPS[53],the MATLAB software designed for solving multi-phase optimal control problems using the pseudospectral method in [23]. We use SNOPT[25] as the NLP solver.

2.3.1 Descent Profile Simulation

We simulate two aircraft types, B737-500 (B735) and B767-400 (B764), with predetermined flap speed schedules. In the simulation, the altitudes are specified relative to mean sea level (MSL) and the airspeed constraints in section 2.2 are given as CAS instead of indicated airspeed (IAS). We assume that CAS is equivalent to IAS by ignoring the installation error. The aircraft performance data from BADA[2] is used in the analysis. However, other general performance data can be used since the formulation is quite general. The predetermined flap speed schedules are shown in Table 1. The aircraft mass chosen is 52,000 kg for the B735 and 158,800 kg for the B764 based on BADA.

Table 1: Flap speed schedules of B737-500 and B767-400(CAS)

	B737-500			B767-400		
flap mode	Flap0	Flap1	Flap2	Flap0	Flap1	Flap2
angle(deg)	0	1	5	0	5	15
extension(kt)	-	210	190	-	230	190
min CAS(kt)	210	190	180	230	190	170

We choose the boundary condition for the numerical examples based on the CDA flight test in Louisville International Airport (KSDF) in [13]. We select a cruise altitude of 35,000 feet and a cruise speed of Mach 0.7818 (265 KCAS). The maximum allowable descent speed is 350 KCAS for both B735 and B764. As shown in Table 2, the trajectory optimization starts at the chosen cruise altitude and cruise speed and terminates at the IAF with an altitude of 3,000 feet at a track distance of 8 NM from the runway threshold and a speed of 180 knots. After this point, the aircraft captures the Instrumental Landing System (ILS) glide slope and flies the ILS approach. The initial along track distances d_{max} are set as 150 NM for both the B735 and the B764. International Standard Atmosphere (ISA) conditions are assumed for this simulation, and the air density, pressure, and temperature equations in [2] are used.

Table 2: Initial and final point conditions

	Initial condition			Final condition		
Aircraft	H (ft)	CAS (kt)	Dist. (NM)	H (ft)	CAS (kt)	Dist. (NM)
B737-500	35,000	265	-150	3,000	180	-8
B767-400	35,000	265	-150	3,000	180	-8

2.3.2 VNAV CDA

We also compare the optimal trajectories to a reference CDA trajectory generated by the FMS VNAV function. This vertical trajectory was used for a flight test conducted at KSDF in September 2004[56]. As shown in Fig. 3, the KSDF VNAV CDA profile is determined by a series of VNAV modes. The first segment of this trajectory is the cruise segment. The second segment of VNAV CDA profile is the idle thrust segment. In the second segment, the en route part, which is above 10,000 ft, is generated by constant MACH, constant CAS, and constant descent rate modes[58]. In the en route part, constant MACH/CAS is set to 0.7818/350. At the end of the en route part in the second segment, the aircraft attains the FAA regulated speed of 250 knots at 10,000 ft. From that point onwards, constant CAS at 250 knots and constant FPA segments are used to satisfy the final point conditions. The VNAV CDA profile is calculated via backward integration from the final point to TOD. The mode change between constant CAS and constant FPA occurs when the CAS reaches 250 knots during the backward integration from IAF. By this way, the engine throttle would remain at idle during the entire procedure from the TOD to the final point.

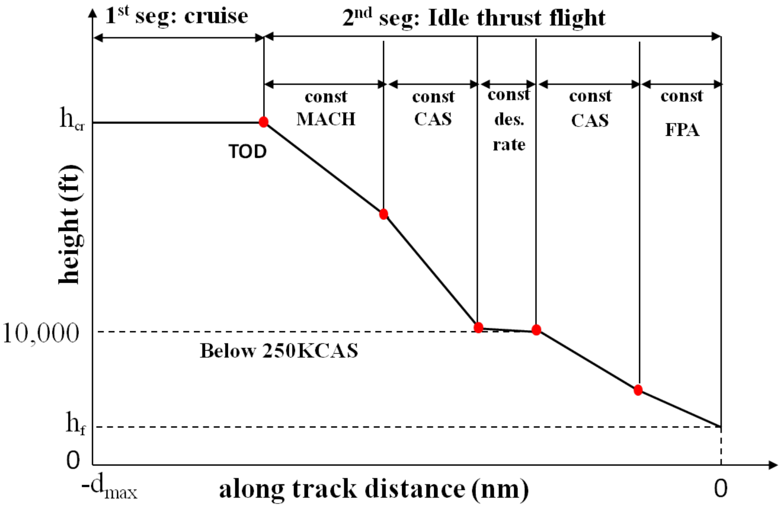

Figure 3: VNAV CDA trajectory structure

2.3.3 B737-500 Results

The results of the B735 minimum time and minimum fuel optimal trajectories are shown in Figures 4 and 5 along with the VNAV CDA trajectory. For the minimum time case shown in Figure 5, the aircraft accelerates until it reaches the 350 knot maximum allowable speed, and then descends at a constant CAS. To satisfy the FAA speed limit regulation, prior to 10,000 ft, the aircraft decelerates at the minimum descent rate. Below 10,000 ft, the aircraft flies at the maximum speed of 250 knots as long as possible before decelerating to reach the final speed and altitude conditions. The altitude and speed profiles are determined at the boundaries of several constraints. These characteristics of the minimum time profile imply that the aircraft flies with maximum performance to reduce flight time.

The minimum fuel trajectory is quite different from the minimum time trajectory. For the minimum fuel trajectory, the aircraft flies with idle power as long as possible; hence, the aircraft starts descending much earlier than in the minimum time case. From TOD to 10,000 ft, the aircraft descends with small variations in flight path angle as shown in Figure 4. Furthermore, the speed variation from TOD to the end point of the first phase is also small. The speed profile is determined to be near 250 knots, which is the maximum allowable speed below 10,000 ft.

Figures 4 and 5 reveals an interesting result. At 10,000 ft, the minimum fuel and minimum time trajectories intersect and are identical below 10,000 ft. This fact means that the noise impact is the same for both optimal trajectories since the noise impact in the vicinity of the airport is a function of the state of aircraft below 10,000 ft. Another important result is that the performance difference between the minimum time and the minimum fuel trajectories occurs only above 10,000 ft trajectory which is during the en route descent.

Table 3 reflects the numerical results of the optimal vertical profiles for the B735. As shown in the table, the optimal TOD position in the minimum time case is 89.853 NM from the runway threshold, which is about 18 NM closer to the runway threshold than the optimal TOD for the minimum fuel case, which is about 107.129 NM from the runway threshold. In addition, if the aircraft flies along the minimum fuel trajectory, as much as 54.56 kg fuels can be saved, which is about 11.88% of the total fuel burned in the minimum time case. On the other hand, if the aircraft flies along the minimum time trajectory, we can reduce flight time by 177.2 seconds, which is a 12.16% reduction in the flight time compared to the flight time needed for the minimum fuel case. The VNAV CDA case results are very similar to the results of the minimum time case with a difference in fuel burn of only 5.7 kg and a flight time difference of only 19.71 seconds.

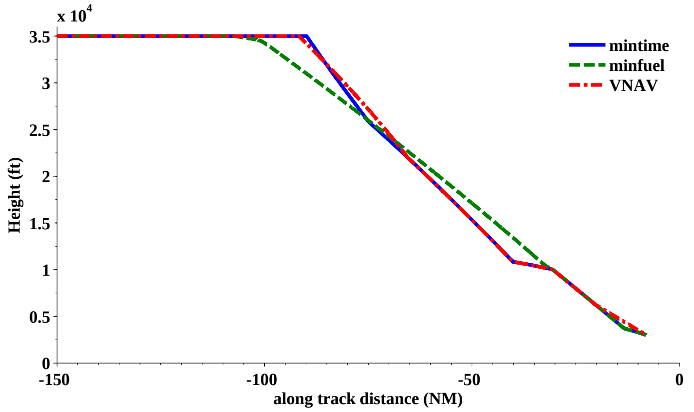

Figure 4: B737-500 optimal vertical profiles, zero wind case

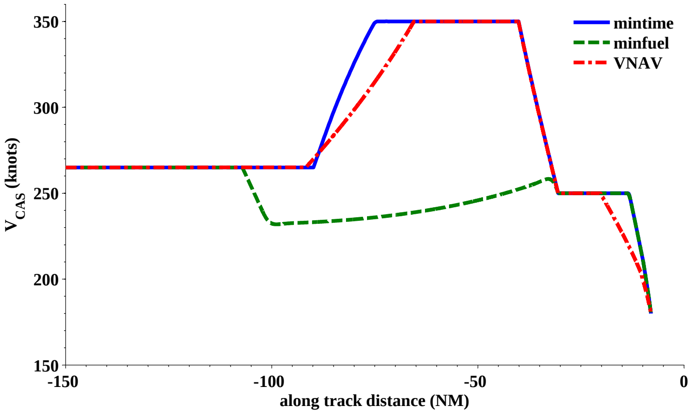

Figure 5: B737-500 optimal CAS profiles, zero wind case

Table 3: Numerical results of B737-500 optimal trajectories

Performance Index	TOD (NM)	Fuel burn (kg)	Arrival time (sec)
minimum time	-89.853	459.320	1,280.26
minimum fuel	-107.129	404.756	1,457.50
VNAV CDA	-91.714	453.640	1,299.97

2.3.4 B767-400 Results

The optimal vertical and speed profiles of a CDA procedure for the B764 with respect to minimum time and minimum fuel performance indices are shown in Figs. 6 and 7, respectively. Compared to the B735, the B764 is quite large and heavy; hence, the performance characteristics of the aircraft are quite different from those of the B735. Despite the large differences in the parameters, we can see that the tendencies of the B764 optimal trajectories are very similar to those of the B735 when comparing the trajectories and speed profiles in Figs. 4 through 7. In the minimum time case, the optimal CDA speed and altitude profiles for the B764 are determined at the boundaries of the constraints, and this tendency is the same as that for the B735 optimal profiles. The minimum fuel optimal profiles for the B764 intersect the minimum time optimal profile at 10,000 ft, and below this point, the optimal profiles of two performance indices are the same as in the B735 case. As in the B735 profiles, the noise impacts below 10,000 ft are identical between minimum fuel and minimum time trajectories.

The numerical values of the optimal vertical profiles for the B764 are shown in table 4.

Flight along the minimum fuel profile consumes 84.7 kg less fuel than in the VNAV CDA case, which is an 11.7% fuel savings when compared to the VNAV CDA case. A minimum time profile can reduce flight time by as much as 22.83 sec when compared to the VNAV CDA case and 161.32 sec when compared to the minimum fuel case.

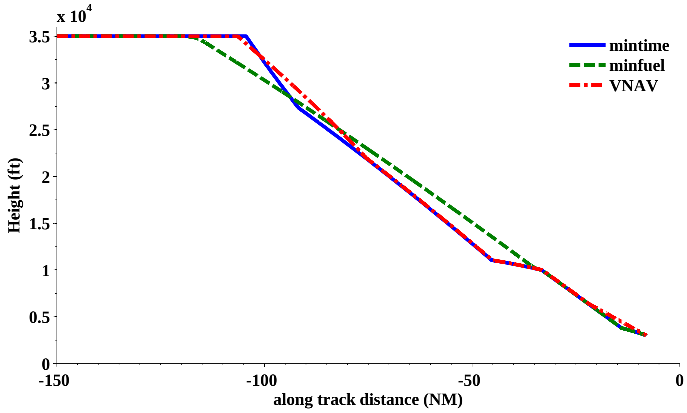

Figure 6: B767-400 optimal vertical profiles, zero wind case

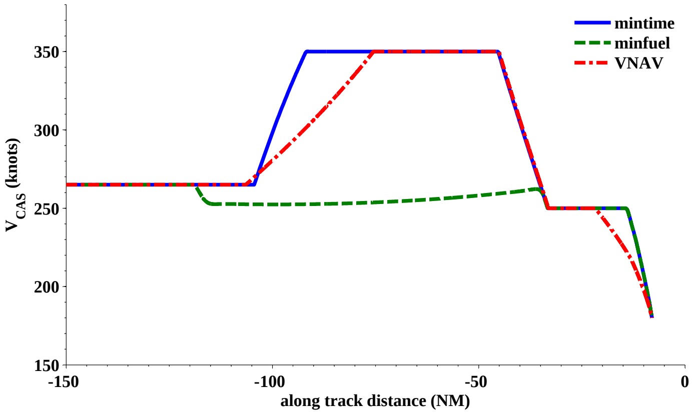

Figure 7: B767-400 optimal CAS profiles, zero wind case

Table 4: Numerical results of B767-400 optimal trajectories

Performance Index	TOD (NM)	Fuel burn (kg)	Arrival time (sec)
minimum time	-104.417	741.636	1,296.86
minimum fuel	-118.801	642.359	1,458.18
VNAV CDA	-106.445	727.074	1,319.69

2.3.5 Effect of Wind

Since the wind profile strongly affects the aircraft trajectory, it is very important to observe the sensitivity of the optimal trajectory with respect to various wind speeds and directions. To observe the wind effect on the optimal trajectory, we performed numerical experiments with various wind speeds and directions. In this study, we consider a wind speed range from -20 m/s to 20m/s, where a negative value denotes a headwind and a positive value denotes a tailwind.

The effects of wind on the B735 minimum time and minimum fuel trajectories are shown in Figures 8 and 9, respectively. As expected, the TODs in the headwind cases are more distant than they are in the zero wind case, and the TODs in the tailwind cases are closer than in the zero wind case. However, the structures of the vertical profile in all wind cases are the same as they are in the zero wind case. The wind cases also do not alter the relationship between the minimum time and minimum fuel vertical profiles. The TOD variations with respect to the wind conditions are shown in Figure 10 comparison to the zero wind case. The variations are almost linear for both the minimum time and fuel profiles. However, the slope of the TOD variation with wind for the minimum fuel trajectory is steeper than that for the minimum time trajectory. This implies that the minimum fuel optimal profile is more sensitive to wind than the minimum time optimal profile.

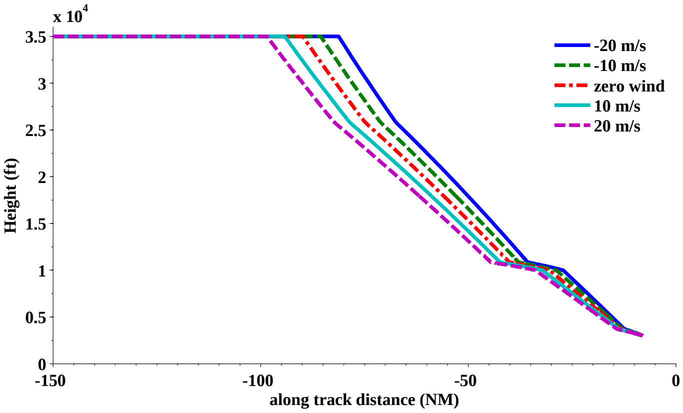

Figure 8: B737-500 minimum time trajectories for different wind conditions

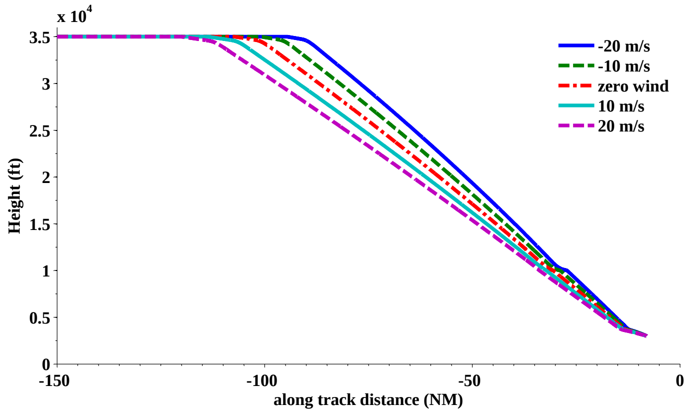

Figure 9: B737-500 minimum fuel trajectories for different wind conditions

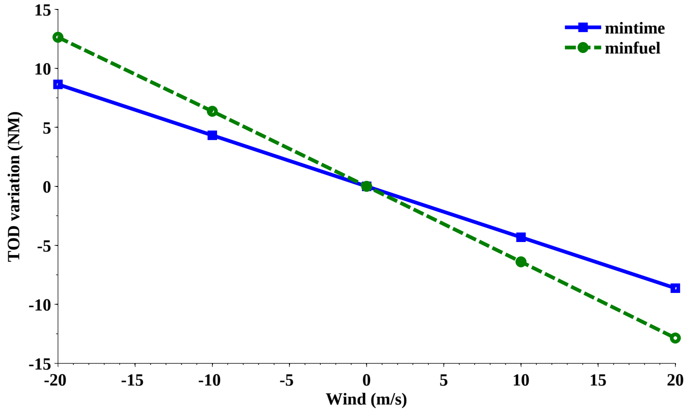

Figure 10: B737-500 TOD variations with respect to the wind conditions

2.3.6 Effect of Cross Wind

To evaluate the cross wind effects on the optimal trajectory, we compared the case in which the cross wind term W_c is zero and non-zero W_c case with the same horizontal wind speed. We simulated three different W_h cases; W_h is zero, $10m/s$, and $-10m/s$. The wind vector can be described as a combination of total wind speed and angle Ψ_w. Note that Ψ_w is the direction of the wind from the North as shown in Figure 2. For example, (10,90) means the total wind speed is 10 m/s and the Ψ_w is 90 degree. Therefore, (0/0,20/90), (10/0,20/60), and (10/180,20/120) are the cases where the W_h is the same each other, but the W_c is different. We compared the results with these wind speed pairs.

The cross wind effects on the B735 minimum time and minimum fuel CAS profiles are shown in Figures 11 and 12, respectively. These figures show that the effect of the cross wind term is relatively smaller than effect of the horizontal wind in both minimum time and minimum fuel cases.

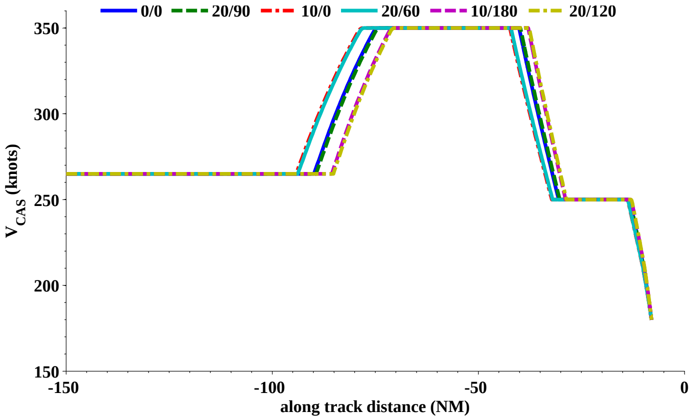

Figure 11: B737-500 minimum time CAS profiles with different cross wind conditions

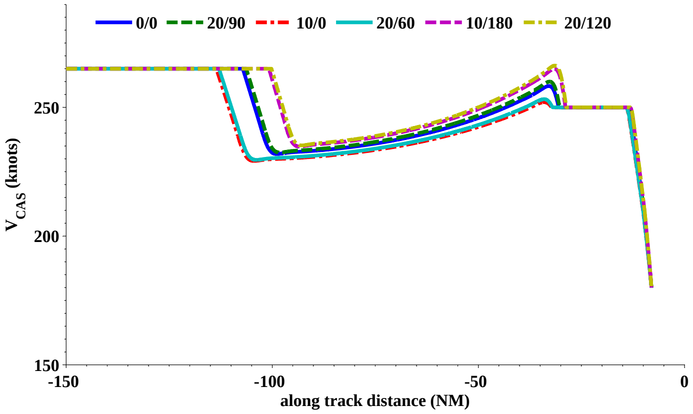

Figure 12: B737-500 minimum fuel CAS profiles with different cross wind conditions

2.3.7 Effect of Wind Shear

To evaluate the wind shear effect on the optimal trajectory, we solved the optimal control problem with the following nominal wind model:

$$W = A_0 \left(\frac{h}{h_0} \right)^{A_1} \tag{34}$$

where A_0 is the wind at h_0, A_1 represents the wind shear effect terms. We used the four different wind conditions; (A_0, A_1) are (20,0), (20,1/7), (20,3/7), and (20,1). Here, we used the cruise altitude as h_0, and hence A_0 is the wind speed at the cruise altitude.

The wind shear effects on the B735 optimal CAS profiles are shown in Figure 13. The CAS profiles in minimum time cases are the same regardless of different wind shear terms as shown in Figure 13(b). The minimum time CAS profiles in all cases are generated on the boundaries of the path constraints. In minimum fuel case in Figure 13(c), the CAS profiles are not exactly same, but they are very similar to each other. This observation means that wind shear effects on the minimum fuel trajectories are small, and the dominant wind term is the wind speed at the cruise altitude as shown in Figures 9 and 12.

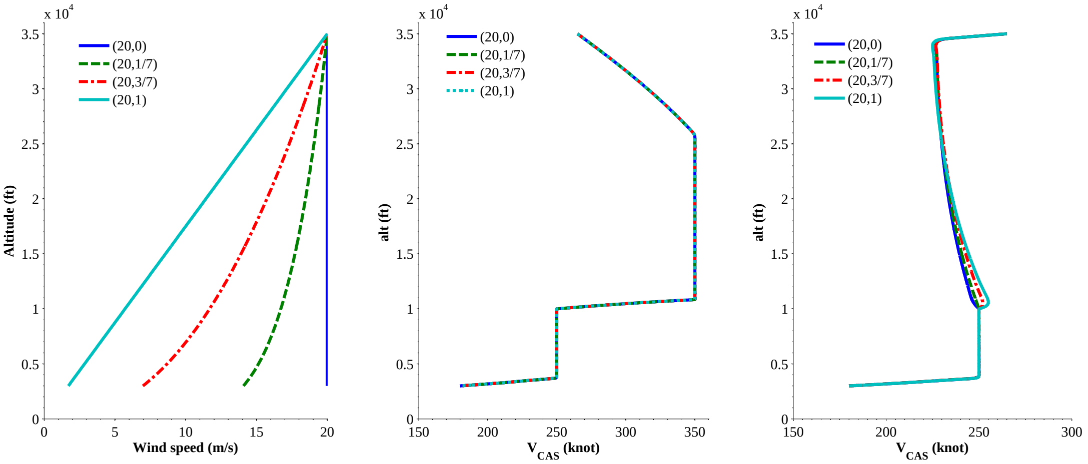

(a) Wind (b) mintime (c) minfuel

Figure 13: B737-500 optimal CAS profiles with different wind shear conditions

2.4 Suboptimal VNAV Trajectories Strategy

In the current CDA arrival procedures, the vertical flight path and speed profile are calculated by the FMS using VNAV descent algorithms that have been in use for over two decades. For this reason, an arrival procedure with FMS generated trajectory can produce many benefits including enhancement of both the pilot's and controller's situational awareness and, therefore, enhanced safety. Thus, even though some performance degradation may occur when compared to arrivals flying the optimal trajectories obtained in section 2.3, a VNAV CDA procedure can have many benefits from a practical implementation point of view.

In this section, we present suboptimal VNAV CDA trajectories in terms of minimum flight time and minimum fuel consumption. The suboptimal VNAV trajectories are divided into several segments, and each segment is built with existing VNAV descent algorithms. VNAV descent algorithms are categorized in terms of constant CAS/Mach mode, constant flight path angle (FPA) mode, and constant rate of descent (ROD) mode[58]. Since flight idle thrust setting is assumed for the purpose of reducing the noise impact, the same as with optimal trajectories in section 2.3, VNAV CDA trajectories are typically built with idle thrust assumption. Hence, each mode calculates flight path angle which is the control input of Problem 2.1.

2.4.1 Minimum Time Suboptimal VNAV CDA

In both the B735 and the B764 cases in section 2.2, the minimum time speed profiles are determined at the maximum performance bounds such as the maximum rate of descent, the maximum flight path angle, and the maximum CAS as shown in Figures 5 and 7. From this observation, we propose the minimum time suboptimal VNAV CDA trajectory structure as shown in Figure 14.

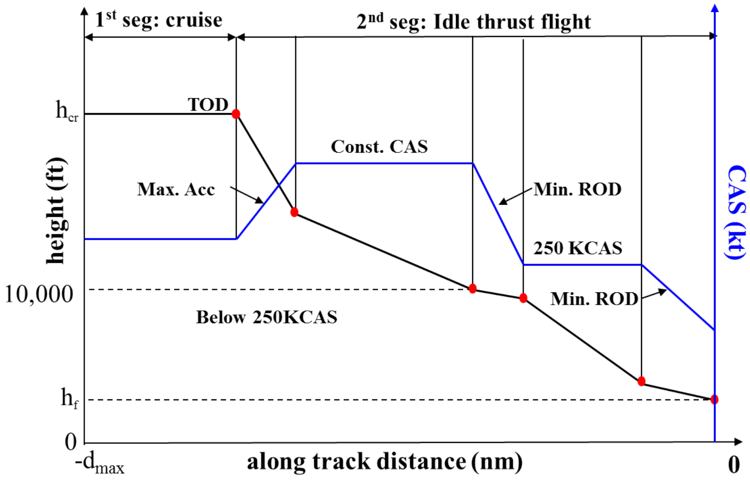

Figure 14: Proposed mintime VNAV altitude and speed profile

The proposed minimum time VNAV CDA suboptimal speed profile consists of two segments; a cruise segment and a flight idle descent segment. The idle descent segment is generated by forward and backward integration using the VNAV mode sequence: maximum acceleration - constant MACH/CAS - minimum rate of descent - constant CAS of 250 knots - minimum rate of descent. The first component of the second segment in Figure 14, which is maximum acceleration mode, starts at the TOD and is generated by the forward integration with the CAS increasing during this portion of the descent. Depending on the initial speed, this component can be generated by using either one of two modes, the maximum descent rate mode or the fixed flight path angle mode, or by using both modes. From the descent rate constraint in Eq. (30) and the control input constraint in Eq. (33), the aerodynamic flight path angle for maximum acceleration is given by

$$\gamma = max(\sin^{-1}(\dot{h}_{min}/V_T), \gamma_{min}) \tag{35}$$

The VNAV CDA trajectory from the second component of the flight idle descent segment to the last component in Figure 14 is generated by backward integration. The second component starts at the point where the CAS reaches the maximum allowable CAS and continues to fly at this CAS as long as possible. If the airspeed reaches the maximum allowable MACH before reaching the maximum CAS, the constant MACH mode with the maximum value should be inserted between the first and second segments in Figure 14. At the end of the second component, the aircraft decelerates using the minimum descent rate until reaching 250 knots, which is the maximum speed below 10,000 feet as stipulated by the FAA regulation. The rest of the trajectory below 10,000 feet is similar to the upper trajectory. Since the maximum allowable speed is 250 knots below 10,000 ft, the speed constraint in Eq.(29) is active. Therefore, the third component is generated using constant CAS. The last component is at the minimum descent rate to decelerate to the final point speed restriction at the specified altitude.

2.4.2 Numerical Results of Minimum Time VNAV CDA

To evaluate the VNAV CDA trajectory with various wind conditions, we compared three wind condition cases; (0/0), (10/0), and (20/0). The first number means the total wind speed in m/s and the second number means ψ_w in degrees. Minimum time CAS profile comparisons between an optimal minimum time CDA and a suboptimal VNAV CDA built as described above are shown in Figures 15 and 16. In both cases, the VNAV results are the same as the optimal results. Since the minimum time optimal trajectories are determined by the aircraft performance bounds such as speed limit, rate of descent limit, and control input limit, the minimum time trajectories can be generated by the combination of VNAV algorithms.

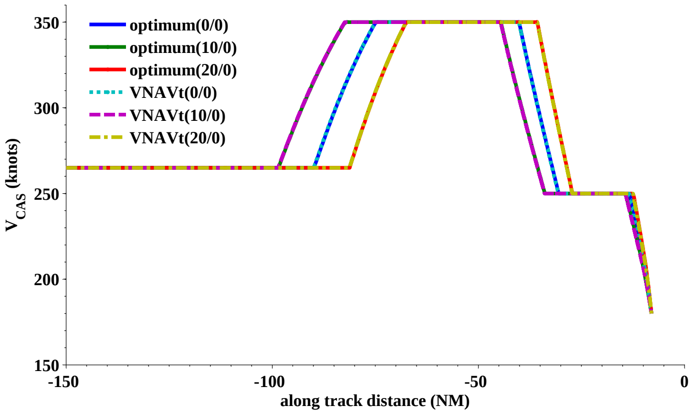

Figure 15: B737-500 minimum time CAS: true optimum and VNAV cases

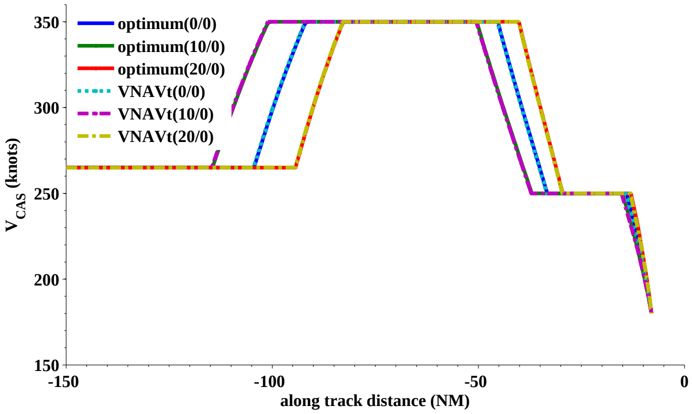

Figure 16: B767-400 minimum time CAS: true optimum and VNAV cases

2.4.3 Minimum Fuel Suboptimal VNAV CDA

While the minimum time VNAV CDA trajectory is easily built using the general aspects of the minimum time optimal control problem, the minimum fuel VNAV CDA profile cannot be determined intuitively because the profile is not determined by the boundaries of the constraints. Therefore, generating an identical profile using a combination of VNAV descent algorithms is impossible. Hence, we need to simplify the optimal profile considering the characteristics of the minimum fuel profiles.

Since the profiles below 10,000 ft are the same for both the minimum time and minimum fuel profile, we can build the same minimum fuel VNAV profile with the minimum time VNAV profile, which consists of a following series of VNAV modes; constant CAS with 250 knots - constant rate of descent with minimum value. The problem is en route descent part, which is the area above 10,000 ft. As shown in Figures 5 and 7, the minimum fuel descent profiles are not determined by the boundaries of the path constraints. Therefore, we must approximate the en-route descent profile with a series of VNAV modes. In this chapter, we use constant rate of descent - constant CAS - constant rate of descent for the en route trajectory generation since constant MACH/CAS descent is used for the current VNAV CDA trajectory generation[13, 56]. The overall structure of the minfuel VNAV CDA trajectory is shown in Figure 17.

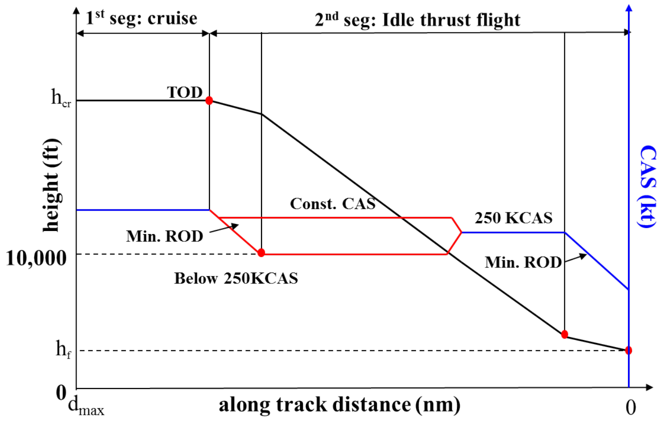

Figure 17: Proposed minfuel VNAV altitude and speed profile

Since the minimum fuel VNAV profile is simple and most of the descent is at a constant speed, the proposed VNAV trajectory has the benefit of pilot controllability. With the proposed VNAV profile, the procedure is executed and controlled by the FMS which monitors the progress of the planned descent both laterally and vertically. Control inputs are not required by the pilot unless the FMS senses that the aircraft cannot maintain the desired trajectory within its control capability and prompts the pilot that specific action is needed to maintain the profile.

The minimum fuel VNAV CDA trajectory optimization problem in Figure 17 can be solved by modifying the original optimal control problem described in section 2.2. By using the VNAV mode sequence for minimum fuel en route descent profile, we divide the en route descent phase of the idle thrust segment in Figure 2 into three phases: constant rate of descent, constant CAS, and constant rate of descent. The rate of descent values of the first and the third phases are determined by CAS value in the second phase. If the optimal CAS in the second phase is lower than cruise speed, the first rate of descent is set to the minimum rate of descent value to decelerate. On the other hand, the rate of descent is set to the maximum value to accelerate if the CAS in the second phase is larger than cruise speed. The rate of descent at the third phase is determined by comparing the optimal CAS with 250 knots, which is the CAS at 10,000 ft. Then, the minimum fuel VNAV CDA trajectory can be described only one parameter, which is the CAS value in the second phase. Therefore, the original optimal control problem can be converted to the following parameter optimization problem:

$$\begin{aligned} &min\ J(V_{CAS}) \\ &V_{min,CAS} \leq V_{CAS} \leq V_{max,CAS} \end{aligned} \tag{36}$$

2.4.4 Numerical Results of Minimum Fuel VNAV CDA

Evaluating the performance of the proposed minimum fuel VNAV profile requires a comparison with the minimum fuel optimal profile. Since the minimum VNAV CDA trajectory optimization problem in Eq. (36) is the parameter optimization problem with only one parameter, it can be solved very easily using the nonlinear programming solvers. In this section, we used an interior point method to solve this optimization problem.

Altitude and speed profile comparisons between the minimum fuel optimal CDA and the proposed VNAV CDA are shown in Figures 18 and 19. Although the speed profiles above 10,000 feet of the proposed VNAV trajectory are different from the optimal profile, we can observe that the altitude profiles of the proposed VNAV trajectory are similar for all wind cases. The CAS determined by the parameter optimization is very close to the average CAS of the en route descent segment of the true optimal trajectory in section 2.3.

The characteristics of the minfuel VNAV CDA are documented in Tables 5 and 6. As expected, there is performance degradation with regard to fuel consumption. This degradation may have occurred due to the differences in the speed profiles. Since the TOD points of VNAV trajectories are smaller than those of true optimal trajectories for all wind cases for both aircraft, the fuel burns of VNAV trajectories during the cruise are smaller than those of true optimal trajectories. Therefore, the fuel burn difference between true optimal and VNAV suboptimal trajectories comes from the descent segment.

In the B735 case, the maximum difference among the three wind cases is 1.042 kg in fuel and 7.413 sec in flight time. In the B764 case, the maximum difference in fuel consumption between the two trajectories is only 0.407 kg. As these numerical results show, we can observe that the performance degradation that results from simplifying the speed profile is very small. Therefore, by using the proposed VNAV profile, we can obtain many practical benefits of a VNAV approach while introducing only very small performance degradation when compared to the optimal trajectory.

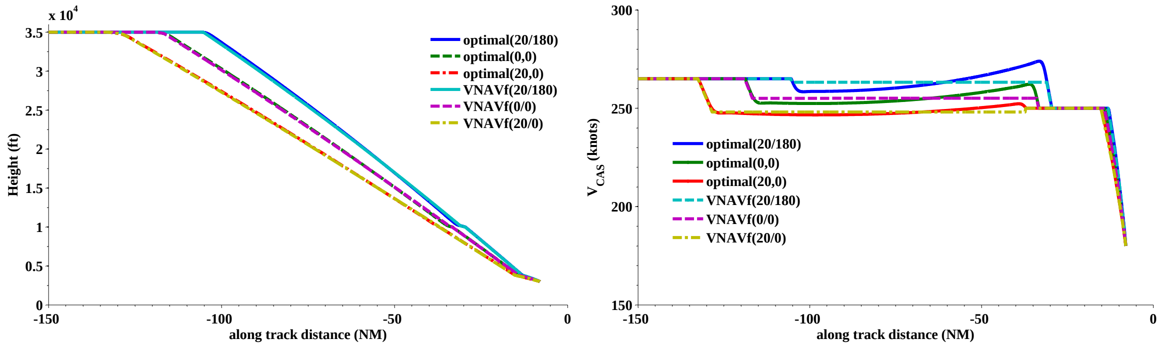

(a) altitude

(b) CAS

Figure 18: B764 minimum fuel trajectory comparison of optimal and VNAV suboptimal result

Table 5: Numerical comparison of B767-400 VNAV trajectories

	True optimal			VNAV suboptimal		
Wind(W/ψ_w)	time (sec)	Fuel (kg)	TOD (NM)	time (sec))	Fuel (kg)	TOD (NM)
(20,180)	1,570.169	825.216	-105.382	1,574.091	825.436	-105.537
(0,0)	1,458.181	642.359	-118.801	1,461.071	642.766	-118.910
(20,0)	1,362.887	486.195	-132.535	1,363.354	486.330	-132.533

The optimal CAS values of B735 and B764 for the en route descent with different wind conditions are shown in Figure 20. The optimal CAS values varies as the wind speed at

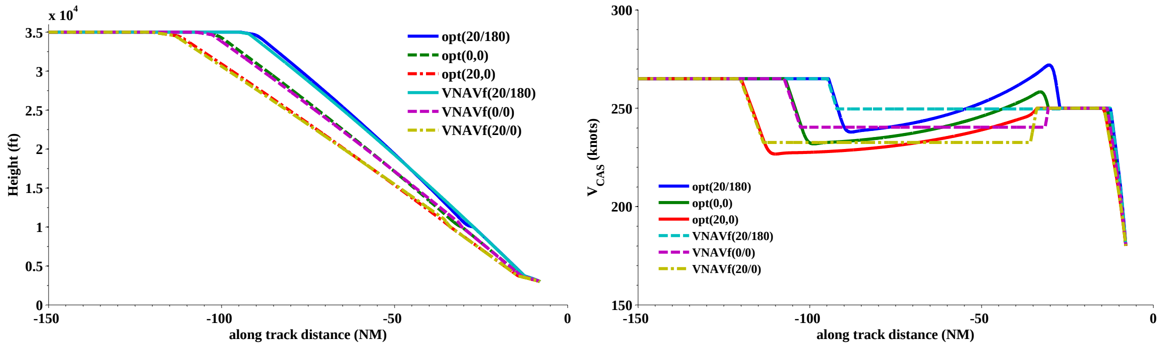

(a) altitude (b) CAS

Figure 19: B735 minimum fuel trajectory comparison of optimal and VNAV suboptimal result

Table 6: Numerical comparison of B737-500 VNAV trajectories

	True optimal			VNAV suboptimal		
Wind(W/ψ_w)	time (sec)	Fuel (kg)	TOD (NM)	time (sec))	Fuel (kg)	TOD (NM)
(20,180)	1,566.065	494.365	-94.506	1,573.478	495.407	-94.811
(0,0)	1,457.488	404.756	-107.129	1,463.787	405.380	-107.436
(20,0)	1,363.354	328.066	-119.990	1,367.821	328.395	-120.253

cruise altitude changes. The optimal CAS decreases as tailwind increases. However, the parameter A_1 in the nominal wind model in Eq. (34) does not affect the optimal CAS values. This result means that optimal CAS value is more sensitive to A_0, which is the wind speed at the cruise altitude, than the wind shear term A_1. This result is very similar to the result of the wind shear effects in section 2.3.

The cross wind effects on the optimal CAS values of B735 and B764 are shown in Figure 21. The variation of the optimal CAS due to the cross wind is much smaller than the variation due to the horizontal wind.

From the above results, we found that the horizontal wind speed at the cruise altitude is the most dominant factor to determine the optimal CAS value for minimum fuel VNAV CDA trajectory with the given structure in Figure 17. As shown in Figures 20 and 21, the differences of optimal CAS when compared to the constant horizontal wind case are less than 2 knots for all tested wind conditions. Furthermore, the optimal CAS values can be approximated by a quadratic equation with respect to the horizontal wind speed at

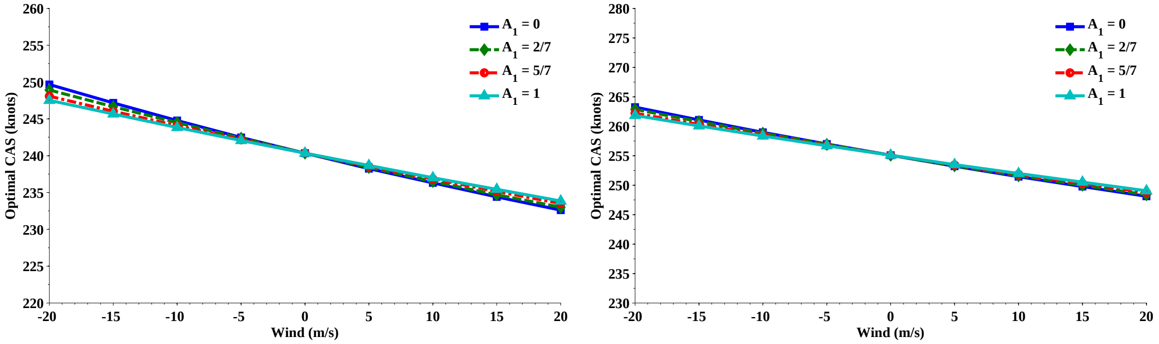

(a) B737-500

(b) B767-400

Figure 20: Minimum fuel CAS with various wind shear conditions

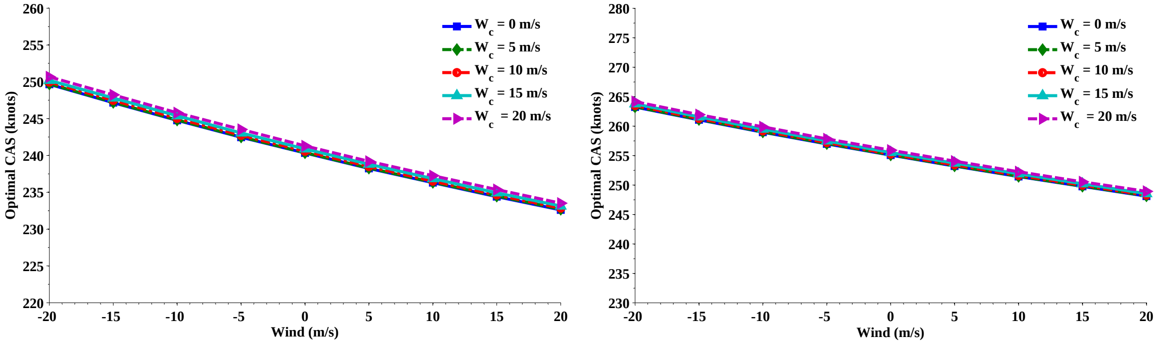

(a) B737-500

(b) B767-400

Figure 21: Minimum fuel CAS with various cross wind conditions

the cruise altitude. Therefore, if the FMS has this approximated equation, then FMS can generate minfuel VNAV CDA trajectory close to the true optimal trajectory without solving the optimization problem in Eq. (36). The approximated optimal CAS value functions for B735 and B764 are as follows:

$$V_{CAS}^{opt} = \begin{cases} 2.0305 \times 10^{-3} W_h^2 - 0.4255 W_h + 240.33 & \text{if B737-500} \\ 1.5544 \times 10^{-3} W_h^2 - 0.3770 W_h + 255.05 & \text{if B767-400} \end{cases} \quad (37)$$

2.5 Conclusion

A Continuous Descent Arrival (CDA) procedure is beneficial in that its application can reduce operating costs by reducing flight time and fuel burn and has the environmental benefits of reducing noise and gaseous emissions. To maximize these benefits, we formulated a CDA trajectory optimization problem with a specified range which includes a part of the cruise segment. The CDA trajectory optimization formulation was aided by a multiple phase optimal continuous Bolza problem framework. Each phase was divided according to the flap speed schedule and the FAA speed limit regulation. In the proposed formulation, a point mass model in a relative wind frame was used as equations of motion for the aircraft by considering the trade-off between model accuracy and computational burden. By establishing a free condition at the initial along track distance, we simultaneously obtained both an optimal Top of Descent (TOD) position and a descent trajectory.

The formulated multi-phase optimal control problems were solved using a pseudospectral method for two aircraft types: the B737-500 and the B767-400. The various numerical results presented here have led to an understanding of the characteristics of the optimal trajectories with respect to flight time and fuel consumption. The two optimal trajectories are identical below 10,000 ft while the speed and altitude profiles of the en route descent part are quite different. This result means that the possible performance variations come from the en route descent part.

Based on this analysis of true optimal trajectories, we were able to find the Vertical Navigation (VNAV) mode sequence for both minimum time and minimum fuel cases. By using these fixed mode sequence, we were able to build the suboptimal VNAV CDA profiles with objective functions of minimum flight time and minimum fuel consumption. Since the proposed VNAV CDA profiles can be calculated by onboard Flight Management System (FMS) computers without additional equipment, they represent a practical implementation. In the minimum time case, all segments of the optimal trajectory are determined at the boundary of the constraints, and the proposed VNAV CDA profile is constructed with the aircraft descending under maximum allowable operating conditions. The resulting performance of the VNAV CDA profile was identical to the optimal results. In the minimum fuel case, the suboptimal VNAV trajectory problem was converted to the parameter optimization problem, and the optimal CAS was calculated with different wind cases. The numerical results showed that the dominating factor in determining the optimal CAS is the horizontal speed at cruise altitude. Based on this result, we approximated the optimal CAS value functions using quadratic formulation.

The analysis result and the proposed VNAV trajectory generation method can be applied in both ground and airborne automation systems. If the aircraft has the capability to calculate the parameter optimization, using the proposed VNAV sequence, the optimal trajectory can be calculated very quickly, and hence realize the online trajectory planning. The alternative way is that a ground automation tool solves the parameter optimization problem using the proposed VNAV sequence and sends the optimal parameter to the aircraft via datalink.

Another application of this study is the decision supporting tool to determine the optimal scheduling of the traffic flow to the runway. To determine the optimal scheduling, which is Required Time of Arrival (RTA), air traffic controller should have to know the performance bound of the individual aircraft such as the feasible time range of CDA flight. This study provides the methodology to analyze the performance bound of individual aircraft. The performance bound analysis results can be used as constraints of the optimal scheduling problem.

CHAPTER III

EN ROUTE DESCENT TRAJECTORY OPTIMIZATION

In Chapter 2, the CDA trajectory optimization problem was formulated as a multi-phase optimal control problem from cruise altitude to a Final Approach Fix (FAF). While an unconstrained CDA trajectory was considered, it must be acknowledged that many published Standard Arrival Routes (STARs) used for CDA procedures have both speed and altitude constraints at some waypoints along the ground track inside the Terminal Radar Approach Control (TRACON) area.

The traffic efficiency problem associated with a CDA procedure comes from the difficulty in predicting the aircraft trajectory. Since the CDA trajectory is constantly descending, management of the required aircraft separation becomes problematic when compared to the existing "step-down" arrival where level flight segments and speed changes are used to manage the aircraft separation. ATC's response to CDA separation management is to apply larger separations to accommodate the change in management procedure. To address this, Ren developed the Tool for Analysis of Separation and Throughput (TASAT) [54]. TASAT is a high fidelity aircraft specific descent analysis that uses a Monte-Carlo simulation to vary aircraft weight, wind, and pilot response times. With the descent profiles resulting from TASAT, a minimum time or distance separation can be determined for any leading and trailing aircraft to produce the required minimum separation as the aircraft crosses the runway threshold. This minimum time or distance is then applied to a chosen metering fix along the intended aircraft ground track. When applied, CDA operations can be flown with a minimum of ATC intervention in the TRACON area. By using this required minimum separation at the meter fix, the ATC or Traffic Management Advisor (TMA) determines the Scheduled Time of Arrival (STA) of each aircraft to maximize runway without degrading the success rate of the CDA. Therefore, from the individual aircraft point of view, the Required Time of Arrival (RTA) at the meter fix represents the time required to ensure the minimum separation is maintained during the CDA.

To implement efficient traffic management, aircraft should have the capability to calculate the descent trajectory to meet RTA constraints or ground advisor tools should calculate the required trajectory associated with the RTA trajectory and transmit this information to the aircraft via datalink. In the onboard calculation case, the trajectory prediction issue still remains. The trajectory prediction tools assume that the aircraft vertical trajectory is generated by a combination of Vertical Navigation (VNAV) modes. Therefore, if the trajectory generated by the FMS does not comply with this assumption the errors become larger. In the latter case, for current FMS systems, ground advisory tools are required to transmit the FMS inputs such as VNAV mode sequence and mode parameters. Hence, in both instances, the trajectory generation method using VNAV modes should be maintained. Therefore, the trajectory optimization method with current VNAV modes is necessary to address this issue.

In this chapter, we address the CDA trajectory optimization problem in the en-route phase with an RTA constraint at the meter fix and propose a fixed RTA optimal trajectory generation algorithm that is possible to implement in the FMS. In the FMS, the VNAV mode transition pairs are predetermined and occur only when some components of an aircraft's state meet a certain condition. Therefore, a VNAV mode transition in the FMS can be modeled as a hybrid automaton. Hence, the vertical trajectory generation within an FMS framework is a hybrid system. Therefore, minimizing costs while satisfying RTA constraints requires solving the optimal control problem for a hybrid system. This problem is much more difficult to solve compared to typical optimal control problems of continuous systems because, in a hybrid system, the discrete state mode sequence and mode switching times are control variables as well as control inputs for the continuous state evolution[29].

The sequential method, in which the mode sequence is determined and the optimal control problem with determined mode sequence is solved, is proposed as a way to solve optimal control problems of hybrid systems. This proposed method is applied to the en-route trajectory optimization problem and evaluated with numerical examples for two aircraft types; B737-500 and B767-400.

3.1 Introduction

3.1.1 Switched Dynamical Systems

A hybrid system is a dynamical system that has both a continuous state and a discrete state, which is commonly referred to as a mode. The following definition of a hybrid automaton describes hybrid systems [43].

Definition 3.1. (Hybrid Automaton) A *hybrid automaton* H is defined by the collection $H = (Q, X, V, f, Init, Dom, E, G, R)$ where

- $Q = (q_1, q_2, \cdots)$ is a set of discrete states;
- $X = \mathbb{R}^n$ is a set of continuous states;
- V is a set of control variables;
- $f : Q \times X \times V \to X$ is a vector field;
- $Init \subseteq Q \times X$ is a set of initial states;
- $Dom : Q \to 2^X$ is a domain;
- $E \subseteq Q \times Q$ is a set of edges;
- $G : E \to 2^{X \times V}$ is a guard condition;
- $R : E \times X \times V \to 2^X$ is a reset map.

where 2^X denotes the set of all subsets of X and hence, G and R are set value maps.

Switched dynamical systems are a subset of hybrid systems that consist of several subsystems, which are referred to as modes, and switching laws that determine the active subsystem at a given time. Typically, in switched systems, there is no jump in state at the switched time, which means the reset map R in definition 3.1 has the identical mapping. The control inputs of switched systems include the sequence of modes, the duration of each mode, and the continuous input or mode parameters.

Many control systems can be modeled in a switched dynamical system framework: automotive systems with different gears[30, 52], and semi-active damping control system[52], tracking problems of mobile robots[71], and aircraft lateral/vertical trajectory generation with Lateral/Vertical Area Navigation (LNAV/VNAV) modes in Flight Management Systems (FMS)[33, 48, 67, 75].

In the literature[3, 27, 17, 38, 70, 74] , the switched system is expressed as

$$\dot{x} = f_i(x(t), u(t), t), i \in Q. \tag{38}$$

where $f_i(x(t), u(t), t)$ is a mode dynamics which is the combined formulation of a vector field f and a mode set Q in definition 3.1. However, Eq. (38) cannot express the trajectory generation problem in the FMS using the VNAV function due to the existence of mode parameters in the VNAV modes.

In this chapter, to capture the natural property of the VNAV function, we focus on the special class of switched systems in which each mode dynamics is expressed as a combination of common dynamics and a mode specific constraint with a mode parameter. The control inputs of such a system can be grouped into two categories: parameter independent inputs and parameter dependent inputs. This class of system is formulated as

$$\begin{cases} \dot{x} = f(x(t), u(t), v(t), t) \\ g_i(x, u, v, p_i) = 0 \end{cases}, i = 1, \cdots, N \tag{39}$$

where the state $x \in \mathbb{R}^n$, independent control $u \in U \subseteq \mathbb{R}^m$ and parameter dependent input $v \in \mathbb{R}^q$; the i^{th} mode parameter p_i has a same dimension with v, and N is the number of modes. The function $f : \mathbb{R}^n \times \mathbb{R}^m \times \mathbb{R}^q \times \mathbb{R} \to \mathbb{R}^n$ represents the common dynamics, and it is assumed that f is Lipschitz continuous. In addition, it is assumed that the mode constraint $g_i : \mathbb{R}^n \times \mathbb{R}^q \times \mathbb{R}^q \to \mathbb{R}^q$ is smooth and v is determined by p_i uniquely.

From Eq. (39), we can define the equivalent switched dynamical system with a parameter by combining common dynamics and mode constraints:

$$\dot{x} = f_i(x(t), u(t), v(p_i), t), i = 1, \cdots, N \tag{40}$$

where f_i is the dynamics of each mode.

The switched systems expressed with Eq. (38) also can be described in the same format as Eq. (39) in the following manner:

$$\begin{cases} \dot{x} = f(x(t), u(t), v(t), t) = \sum_{1 \leq i \leq N} v_i f_i(x(t), u(t), t) \\ g_i(x(t), v(t)) = v(t) - e_i = 0. \end{cases}$$

where v_i is the i^{th} component of v, and e_i is a unit vector that has its i^{th} component as one. Therefore, the switched system expressed as Eq. (39) includes the switched systems in [3, 17, 27, 38, 70, 74].

3.1.2 Numerical Methods for Optimal Control Problems of Hybrid Systems

Several researchers have developed various computational techniques to solve the optimal control problem of switched systems as expressed in Eq. (38). The methods in the literature can be classified as one with a fixed mode sequence[74, 17, 38] or a sequence optimization in which the optimal mode sequence is unknown[3, 27, 70]. In [74, 17, 38], the original optimal control problem was converted to an equivalent optimal control problem by the parameterization of the switching instances and developed algorithms to compute the gradient of the cost function. In [27], Gonzalez et al.developed a bi-level algorithm that divided the problem into two sub-problems. At the lower level, they assumed a fixed mode sequence and solved the optimal control problem with this sequence. At the higher level, the mode sequence was updated using a single mode insertion technique.

In [3], Bengea and DeCarlo proposed a relaxation based method in which switched dynamics were embedded into a continuous system by relaxation of the discrete input to determine the switching instance. This method has a great advantage in that it does not need to assume the mode sequence at all. Optimal mode sequence is obtained directly by solving the embedded optimal control problem. In this chapter, we will extend the relaxed based method to solve the optimal control problem of the switched system expressed in Eq. (39).

3.1.3 Chapter Outline

The remainder of this chapter is organized as follows: In section 2, we present the path constrained optimal control problem for the switched dynamical systems expressed in Eq. (39).

In Section 3, we discuss the lower bound solution of the optimal control problem. In section 4, we propose a sequential method to solve optimal control problems of switched dynamical systems. In section 5, we explain the hybrid system modeling of FMS and analyzes the properties of each VNAV mode. In section 6, we present the formulation of the en-route descent trajectory optimization problem. In section 7, we present the trajectories generated by the proposed algorithm, and compare the results to those of the lower bound solutions. Our conclusions of this study are then presented in section 8.

3.2 Problem Formulation

In this chapter, we address the path constrained optimal control problem of switched dynamical systems in Eq. (40) as follows:

Problem 3.1.

$$\min \quad J_1 = \Phi(x_0, t_0, x_f, t_f) + \int_{t_0}^{t_f} L(x(t), u(t), v(t))\,\mathrm{dt}$$

s.t.

$$\begin{cases} \dot{x} = f(x(t), u(t), v(t), t) \\ g_i(x, u, v, p_i) = 0 \end{cases}, i = 1, \cdots, N$$

$$C(x(t), u(t), v(t)) \leq 0$$

$$S(x(t)) \leq 0$$

where $C(x, u, v)$ and $S(x)$ are the mixed state-input and pure state path inequality constraints, respectively.

These inequality constraints represent the operational envelope constraints. The problem is an unknown mode sequence optimal control problem of a non-autonomous switched system with path constraints. We have to find the optimal mode parameter as well as the optimal mode sequence.

The switched dynamical system has a fully connected directed graph between modes. In addition, in some modes, self mode transition is allowed if the parameter is changed.

Therefore, the self mode transition with different parameters can be part of the optimal mode sequence.

3.3 Relaxed Optimal Control Problem

Since each mode can be expressed as a combination of a common dynamics and a mode constraint, we can formulate the relaxed optimal control problem by eliminating the mode constraint in (39). The relaxed optimal control problem is converted to a conventional optimal control problem of continuous systems as follows:

Problem 3.2.

$$\min \quad J_2 = \Phi(x_0, t_0, x_f, t_f) + \int_{t_0}^{t_f} L(x(t), u_a(t)) \, \mathrm{dt}$$

s.t.

$$\dot{x} = f(x(t), u_a(t), t)$$

$$C(x(t), u_a(t)) \leq 0$$

$$S(x(t)) \leq 0.$$

where the augmented input $u_a = [u, v]^T$.

Let F_1 and F_2 be the feasible solution set of Problem 3.1 and Problem 3.2, respectively. Since we eliminate the mode constraint in Problem 3.2, $F_1 \subseteq F_2$. Therefore,

$$J_2^{opt} \leq J_1^{opt}. \tag{41}$$

From Eq. (41), we can conclude that the optimal solution of Problem 3.2 provides the lower bound solution of the Problem 3.1. Since the relaxed optimal control problem now becomes a conventional optimal control problem, we can choose one of numerical methods which have been developed with proven performance. For this reason, we can solve Problem 3.2 more easily than the original problem.

3.3.1 Structure Analysis of Lower Bound Solution

To analyze a structure of the optimal solution, we need to investigate the necessary condition for the optimality. The Hamiltonian of the relaxed problem is defined as

$$H(t) = L(x(t), u_a(t)) + \lambda^T f(x(t), u_a(t), t). \tag{42}$$

The optimal control u_a^{opt} is determined by the minimum principle, and it has a following formulation[28]:

$$u_a^{opt}(t) = argmin_{\Omega} H(t) \tag{43}$$

where $\Omega = \{u_a \in U | C(x(t), u_a(t)) \leq 0\}$

From Eq, (104), the optimal solution $x^{opt}(t)$ is split into two categories: 1) nonsingular arc on which $H_{u_a} \neq 0$ and one of the $C(x, u_a)$ is active, and 2) singular arc on which $H_{u_a} = 0$. Since the relaxed problem has state inequality constraints, the singular arc can be further divided into two sub-categories, boundary subarc and interior subarc[35]. The boundary subarc is the arc that one of the state constraints is active, which means the optimal solution is satisfied $S_a(x^{opt}(t)) = 0$ on the boundary arc. Note that the subscript "a" denotes the active path constraint. The interior arc denotes the arc that all state inequality constraints are inactive. Therefore, $x^{opt}(t)$ consists of the several subarcs that is categorized as shown in Fig. 22. At junction points where two different subarcs intersect, the optimal control input u_a^{opt} can be discontinuous by the discontinuity of the costate variables[35].

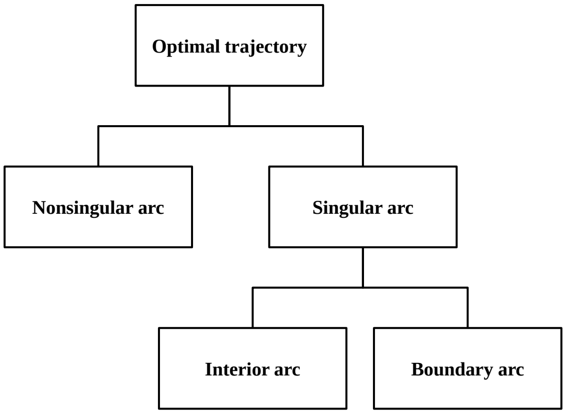

Figure 22: Tree structure of the optimal trajectory

3.4 Sequential Method

The main in this chapter is to find a mode sequence that can generate a similar trajectory when compared to the lower bound trajectory. Then, using the resulting sequence, we can solve a fixed mode sequence optimal control problem instead of an unknown sequence optimal control problem.

To find the optimal solution of problem 3.1, we propose a sequential method which consists of the following four steps.

- STEP1 : Solve the relaxed optimal control problem
- STEP2 : Partition the optimal trajectory of the Problem 3.2.
- STEP3 : Find the mode sequence with the partitioned trajectory from STEP2.
- STEP4 : Solve a multi-phase optimal control problem with the given mode sequence from STEP3.

The relaxed optimal control problem in STEP1 is described as Problem 3.2. In the next subsection, we discuss in detail the processes required to progress from STEP2 to STEP4.

3.4.1 Partition

As shown in Fig. 22, we can group the optimal trajectory $x^{opt}(t)$ of the relaxed problem into three classes: nonsingular arc, interior arc, and boundary arc. First, to distinguish between a nonsingular arc and a singular arc, we use H_v information from the optimal solution of the relaxed problem. If an analytic solution can be obtained, the singular arc segment can be found easily using the analytic value of H_v. However, as in the general case, it is very difficult to find the analytic solution of the optimal control problem with state inequality constraints. Therefore, we have to use a numerical method to solve the relaxed problem. In this case, even though a singular arc exists, the H_v value is not identical to zero and it includes some noise due to the numerical error. To handle this issue, we normalize the H_v value and use the threshold value of T_s to distinguish between a singular arc and a nonsingular arc:

$$\begin{cases} \text{singular arc} & if\, |H_v| \leq T_s \\ \text{nonsingular arc} & otherwise \end{cases} \tag{44}$$

As shown in Fig. 22, a singular arc is divided into two subarcs, boundary and interior arcs. From the discontinuity of costate variables, in Problem 3.2, the parameter dependent control v or $v^{(q)}$ is discontinuous at the junction point[35]. From the smoothness of the mode constraint, in Problem 3.1, v is continuous except for the switching instance. Since the mode constraint changes at the switching instance, v is discontinuous at that point. Therefore, the best mode that is selected from the mode estimation in STEP3 can be different before and after the junction points. For this reason, we partition the singular arc at junction points. By checking the $S(x(t))$ along the optimal trajectory, we can find the boundary subarcs of the singular arc. Due to the error issue, we use a threshold T_b. The remaining singular arc is the interior arc.

3.4.2 Mode Estimation

The key to finding the best mode sequence is a projection of the partitioned trajectory to the trajectory space of each mode. This approach is based on the assumption that if we can generate a trajectory very close to the lower bound trajectory, then its performance is also very close to the lower bound performance J_2^{opt}. Therefore, we select the mode that has the minimum projection error.

This approach is similar to the mode estimation techniques of hybrid systems. For the mode estimation of hybrid systems, many researchers have used the Interactive Multi Model (IMM) filter techniques. The IMM filter consists of the several Kalman filters and each Kalman filter uses the dynamics of the corresponding mode. Therefore, the same number of Kalman filters as the number of modes is necessary. Similar to this method, we need to calculate the projection routine N times. The overall procedure for mode estimation is described in Fig. 23.

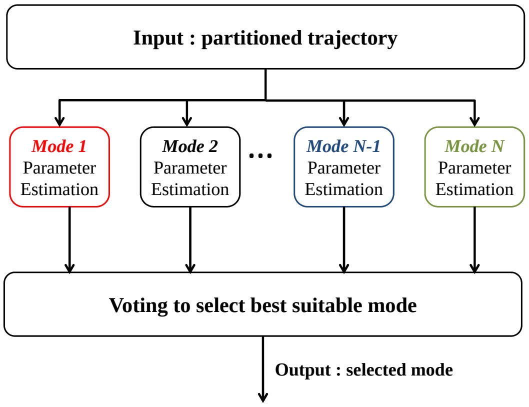

Figure 23: Concept of mode estimation

In order to find the projected trajectory of the lower bound solution into the each mode trajectory space, we have to optimize the corresponding mode parameter. The parameter optimization problem is defined as follows:

$$\begin{aligned}
&\min_{p_i} f(p_i) \\
&f(p_i) = \int_{I_s} \tilde{x}^T Q \tilde{x} + \tilde{v}^T R \tilde{v} \,\mathrm{dt} \\
&+(x_{t_0} - x_0(p_i))^T Q_0 (x_{t_0} - x_0(p_i)) + (x_{t_f} - x_f(p_i))^T Q_f (x_{t_f} - x_f(p_i))
\end{aligned} \tag{45}$$

where $\tilde{x} = x_t - x(p_i)$ and $\tilde{v} = v_t - v(p_i)$; x_t is a partitioned trajectory of the lower bound solution, and $x(p_i)$ is the i^{th} mode trajectory with parameter p_i; v_t is a parameter dependent input of the lower bound solution, and $v(p_i)$ is a parameter dependent input from the i^{th} mode constraint with p_i.

After N iterations of the parameter optimization routine, we calculate a Λ_i value for each mode and select the mode that has the largest Λ value as a mode for the corresponding partitioned trajectory. Λ is determined by the following formulation.

$$\Lambda_i = \frac{r_i}{\sum\limits_{i=1}^{4} r_i} \quad , i = 1, \cdots, N \tag{46}$$

where

$$r_i = \frac{1}{f_i(p_i^{opt})} \quad , i = 1, \cdots, N \tag{47}$$

By repeating this mode estimation process for all partitioned trajectories, we can determine the final mode sequence that is used for STEP4.

3.4.3 Multi-Phase Optimal Control

As a result of STEP3, we obtain the mode sequence for fixed mode sequence optimal control problem of switched dynamical system. Fixed mode sequence optimal control problem is expressed as a multi-phase optimal control problem. Let$\{\sigma_q\}_1^Q$ be the sequence from STEP3, and Q is the number of sequence. Then, we can define following multi-phase optimal control problem.

Problem 3.3.

$$\min \quad J_1 = \Phi_1 + \Phi_Q + \sum_{q=1}^{Q} \int_{t_0^{(q)}}^{t_f^{(q)}} L(x^{(q)}, u^{(q)}, v^{(q)})\, \mathrm{dt}$$

s.t.

$$\begin{cases} \dot{x} = f(x^{(q)}, u^{(q)}, v^{(q)}, t), \\ g_{\sigma_q}(x^{(q)}, u^{(q)}, v^{(q)}, p_{\sigma_q}) = 0 \\ C(x^{(q)}(t), u^{(q)}(t), v^{(q)}(t)) \leq 0 \\ S(x^{(q)}(t)) \leq 0 \end{cases} \quad , q = 1, \cdots, Q \tag{48}$$

$$x^{(q-1)}(t_f) = x^{(q)}(t_0) \quad , q = 1, \cdots, Q-1$$

where $\Phi_1 = \Phi(x_0^{(1)}, t_0^{(1)})$ and $\Phi_Q = \Phi(x_f^{(Q)}, t_f^{(Q)})$.

The last inequality in Problem 3.3 is the link condition for the continuity of the state. This problem also can be solved by the direct method for a conventional continuous optimal control problem. For fast convergence, we use the estimated parameter, the mode trajectory and the parameter dependent control of σ_q mode, which are the results from STEP3, for the initial guess of Problem 3.3.

3.5 Optimal Control Problem for the En Route Descent Trajectory

In this section, CDA trajectory optimization problems in the en-route descent phase are formulated to maximize the benefits of the CDA procedure. Two performance indices, minimum time and minimum fuel, are used to quantify the performance of the CDA trajectory similar to Chapter 2.

$$J_t = \left(x_s^{(1)}(t_0) - d_{\max}\right) / V_g^{(1)} \; + \; t_f^{(N)} \tag{49}$$

$$J_f = \dot{f}_{cr,cruise}\left(x_s^{(1)}(t_0) - d_{\max}\right) / V_g^{(1)} \; + \sum_{p=1}^{N} \int_{t_0^{(p)}}^{t_f^{(p)}} \dot{f}_{cr}^{(p)}\, dt \tag{50}$$

where $\dot{f}_{cr,cruise}$ and $\dot{f}_{cr}^{(p)}$ denote a fuel flow rate in the cruise segment and a flight idle descent fuel flow rate of phase p; $d_{\max}$ denotes the along track distance of the RTA frozen point.

The first term in both cost functions are the cost during the cruise segment, and the second term are for the descent segment. Here, since both constant Mach and altitude are assumed in the cruise segment, $\dot{f}_{cr,cruise}$ is constant, yet $\dot{f}_{cr}^{(p)}$ is a function of the aircraft state.

If altitude and speed constraints exist at the meter fix, they would be published in the charting of the STAR. By introducing RTA constraints, that would be determined and transmitted by ATC, thus the unconstrained CDA trajectory optimization problem 2.1 must be modified to obtain the en-route optimal descent trajectory. For this problem, the path constraints for the flight envelope protection, passenger comfort, and flight path angle limitation remain. If a crossing altitude at the meter fix is above 10,000 ft the required speed can be above 250 knots. If the crossing altitude is at or below 10,000 ft, then the ATC limitation of at or below 250 knots applies. The following is the optimal control problem formulation for the en-route CDA trajectory optimization:

Problem 3.4. (En route CDA Trajectory Optimization Problem)

$$\begin{aligned}
\underset{\gamma}{\text{minimize}} \quad & J_t \quad \text{or} \quad J_f \\
\text{subject to} \quad & \\
& \dot{V}_T = \frac{1}{m}(T - D) - g\sin\gamma - \cos\gamma(\dot{U}_w \cos\chi + \dot{V}_w \sin\chi) \\
& \dot{x}_s = \sqrt{(V_T\cos\gamma)^2 - W_c^2} + W_h \\
& \dot{h} = V_T \sin\gamma \\
& \dot{h}_{min} \le \frac{dh}{dt} \le \dot{h}_{max} \\
& \gamma_{min} \le \gamma \le \gamma_{max} \\
& V_{min,CAS}^{(p)} \le V_{CAS}^{(p)}(t) \le V_{max,CAS}^{(p)} \quad p = 1, \cdots, N \\
& M_{min}^{(p)} \le M^{(p)}(t) \le M_{max}^{(p)} \qquad p = 1, \cdots, N \\
& \mathbf{x}^{(p-1)}(t_f^{(p-1)}) = \mathbf{x}^{(p)}(t_0^{(p)}) \qquad p = 2, \cdots, N \\
& t_0^{(1)} - (x_{s_0}^{(1)} - d_{\max})/V_g^{(1)} = 0 \\
& t_f^{(N)} = t_{RTA} \text{ (if RTA is given)}
\end{aligned} \tag{ECP}$$

3.6 Flight Management System: Hybrid System Modeling

Hybrid system approaches for air traffic control applications, especially for the Conflict Detection and Resolution (CD&R), have been used by several researchers[33, 67]. Tomlin et al.[67] modeled CD&R problem as a hybrid automaton with discrete state set $Q = \{CRUISE, LEFT, STRAIGHT, RIGHT\}$ where each discrete state represents an aircraft's lateral dynamics with a specific strategy. Hwang et al.[33] used a discrete state set $Q = \{TURN, CRUISE\}$ for a hybrid automaton to model aircraft lateral maneuvers.

Similar to these approaches, vertical trajectory can be modeled as a hybrid system using VNAV modes in the FMS. FMSs from different companies have different mode sets, but there are several common VNAV modes, which are constant Mach/CAS mode(CD/CV), constant descent rate mode(CD), and constant Flight Path Angle(FPA) mode(CP) [57]. RNAV CDA trajectories used in CDA flight tests[12, 13] and those of Efficient Descent Advisor (EDA) from NASA are generated by combining these four modes. These four common VNAV modes represent the discrete state set $Q = \{CVCV, CD, CP, CM\}$ in definition 3.1. In each mode, the control input γ in Problem 3.4 is calculated by the state of the aircraft and the mode parameter with each mode assumption. Therefore, the control variable set V of each mode is a mode parameter for calculating γ. For example, target MACH/CAS speed is the mode parameter of the CM/CV mode, the target descent rate is the mode parameter of the CD mode, and the target FPA is the mode parameter of the CP mode.

The vector field f of each mode is the same as the aircraft dynamics in Problem3.4. Hence, the aircraft dynamics is a common dynamics in Eq. (39). $Init(Q, X)$ is determined by the initial conditions of Problem 3.4. $Dom(Q)$ of each mode is a subset of the range inside the flight envelope and is determined by the possible trajectory with γ calculated from the mode parameter: $Dom(Q) = \{\mathbf{x} \in \mathbb{R}^3 | \text{trajectory of Eq. (8)} \sim \text{(13) with } \gamma = \gamma(P(Q))\}$. The reset map of this problem is $R(E, X, V) = \{\mathbf{x}\}$, which means there is no jump in the continuous state when the mode transition occurs.

The mode transition is determined by E and G from the definition 3.1, and these components of a hybrid automaton are determined by the properties of each mode.

3.6.1 Mode Analysis

As stated above, the common mode dynamics of the system in Eq. (39) are the equations of motion of aircraft in Problem ECP. Therefore, in this subsection, we analyze each mode constraint and parameter only. Since this thesis focuses on the trajectory generation for CDA, idle thrust/power is assumed for all modes. Therefore, the only control input is the flight path angle.

The parameters of the four modes are the following: V_{target} for constant CAS mode, $\dot{h}_{target}$ for constant rate of descent mode, γ_{target} for constant FPA mode, and M_{target} for constant Mach mode. Each mode has different characteristics under its own strategy. Furthermore, under each mode assumption, some continuous state variables can be calculated algebraically by using other continuous state variables and γ. In this way, the dimension of the problem can be reduced. The detailed descriptions of each mode are presented below.

3.6.1.1 constant CAS mode : CV

Calibrated airspeed V_{CAS} is a function of V_T and h, so $V_{CAS} = f_V(V_T, h)$. The formulation of f_V is as follows

$$V_{CAS} = f_V(V_T, h) = \left[7R(\Theta_0)_{ISA} \left\{ \left(1 + P_\delta \left[\left(1 + \frac{V_T^2}{7R\Theta} \right)^{3.5} - 1 \right] \right)^{\frac{2}{7}} - 1 \right\} \right]^{0.5} . \quad (51)$$

where $\Theta(h)$ is an atmosphere temperature, and it is a function of an altitude.

In this mode, the mode parameter p_{CV} is V_{CAS} itself. Therefore, the following equality constraint should be hold during CV.

$$g_{CV}(V_T, h, p_{CV}) = f_V(V_T, h) - p_{CV} = 0. \quad (52)$$

Since the constraint is not an explicit function of control γ, control is determined by time derivative of (52).

$$\dot{g}_{CV}(V_T, h, p_{CV}, \gamma) = \dot{f}_V(V_T, h, \gamma) = 0 \quad (53)$$

From Eq. (51), time derivative of V_{CAS} can be obtained as:

$$\dot{V}_{CAS} = \frac{1}{f_{DA}(h, V_T)} \left(\frac{dV_T}{dh} - \left\{ \frac{V_t}{2} \left(\frac{d\Theta/dh}{\Theta} \right) + \frac{z}{(1+z)^{\frac{5}{7}}} \left[\frac{R\Theta}{V_T} \right] \left[-\frac{dP/dh}{P} \right] \right\} \right) \dot{h} \quad (54)$$

where

$$z(h, V_T) = \left[\frac{V_T^2}{7R\Theta} + 1\right]^{3.5} - 1, \tag{55}$$

$$f_{DA}(h, V_T) = \left(\frac{1 + P_\delta z}{1 + z}\right)^{\frac{5}{7}} \left(\frac{T_\theta}{P_\delta}\right) \left(\frac{V_{CAS}}{V_T}\right). \tag{56}$$

In this mode, $\dot{V}_{CAS}$ should be zero, and dV_T/dh can be calculated with Eq.(54) for maintaining the current V_{CAS}.

$$\frac{dV_T}{dh} = \frac{V_T}{2}\left(\frac{d\Theta/dh}{\Theta}\right) + \frac{z}{(1+z)^{\frac{5}{7}}}\left[\frac{R\Theta}{V_T}\right]\left[-\frac{dP/dh}{P}\right] > 0 \tag{57}$$

In Eq.(8), $\dot{V}_T = dV_T/dh \cdot \dot{h}$, and flight idle thrust is assumed. Hence, the only unknown variable is FPA γ and it can be solved algebraically by using Eq. (8) and (57).

Two observations can be made regarding this mode. The first observation is that descending at constant CAS results in a decelerating descent mode in terms of true airspeed. The true airspeed gradient during the flight in this mode is given in Eq. (57). The true airspeed range in which Eq. (57) is positive can be obtained by substituting Eq. (55) and the ISA pressure equation into Eq. (57). This range covers the entire operating speed range for all aircraft. Hence, the result of Eq. (57) is always positive. Therefore, $\dot{V}_t = dV_t/dh \cdot \dot{h}$ is always negative during descent because $\dot{h}$ is negative during descent. The second observation is that we can eliminate true airspeed dynamics, $\dot{V}_T$, in the equations of motion because V_T is a function of altitude and V_{CAS}. Therefore, the reduced state of the CV mode is $x_{CV} = [x_s \quad h]^T$.

3.6.1.2 constant descent rate mode : CD

In CD mode, $\dot{h}$ is constant and the mode parameter p_{CD} is the rate of descent. Hence, γ is obtained from the equations of motion for altitude. The constraint of the CD mode is

$$g_{CD}(V_T, \gamma, p_{CD}) = V_T \sin\gamma - p_{CD} = 0. \tag{58}$$

Since g_{CD} is an explicit function with respect to γ, it is calculated directly from (58) and γ_{CD} is:

$$\gamma_{CD} = sin^{-1}\left(\frac{\dot{h}_{target}}{V_T}\right). \tag{59}$$

In this mode, $\dot{V}_T$ can be both positive and negative. Therefore the CD mode can generate both an acceleration and deceleration segment in terms of true airspeed by setting different values of the parameter $\dot{h}_{target}$.

3.6.1.3 constant FPA mode : CP

The parameter p_{CP} is the control input γ itself. During the CP mode, γ is constant. The constraint of the CP mode is:

$$g_{CP}(\gamma, p_{CP}) = \gamma - p_{CP} = 0. \tag{60}$$

Similar to the CD mode, where the CP mode can generate true airspeed terms for both acceleration and deceleration segments.

3.6.1.4 constant Mach mode : CM

The CM mode is the descent mode with constant Mach number. The parameter p_{CM} of this mode is the target Mach number, and the relationship between V_T and M is:

$$M = f_M(V_T, h) = \frac{V_T}{\sqrt{1.4R\Theta(h)}}, \tag{61}$$

where R is the universal gas constant; Θ is atmospheric temperature that is a function of altitude. The mode constraint of the CM mode is:

$$g_{CM}(V_T, h, p_{CM}) = f_M(V_T, h) - p_{CM} = 0. \tag{62}$$

Since the constraint g_{CM} is not an explicit function of control γ, the control is determined by the time derivative of (62).

$$\dot{g}_{CM}(V_T, h, p_{CM}, \gamma) = 0 \tag{63}$$

The time derivative of Mach number can be calculated by the following equation:

$$\dot{M} = \left[\frac{V_T/dh}{\sqrt{1.4R\Theta}} - \frac{V_T \cdot d\Theta/dh}{2\Theta\sqrt{1.4R\Theta}} \right] \dot{h} \tag{64}$$

In order to descend with constant Mach number, $\dot{M}$ should be zero. From Eq. (64), we can get the target true airspeed gradient as follows:

$$\frac{dV_T}{dh} = \frac{V_T}{2\Theta}\frac{d\Theta}{dh}. \tag{65}$$

Since $d\Theta/dh < 0$ in ISA model and $V_T > 0$, dV_T/dh is negative always; hence, $\dot{V}_T$ is always positive during descent. Therefore, the CM mode is always accelerating in terms of true airspeed.

3.6.2 Mode Transition

Figure 24 represents the directed graph of hybrid automaton for the aircraft trajectory generation in the FMS. Each directed line denotes the direction of mode transition between two modes. In other words, this directed line represents the component of the edge E in the definition 3.1. As shown in Fig. 24, all four modes in FMS can be connected to each other. Any mode in the FMS can be transited to CV mode except the CV mode itself because the speed state is a continuous variable and cannot jump at the moment of mode transition. This transition is denoted by the red color line in Figure 24. As with the CV mode, any mode can be transited to the CM mode except the CM mode itself. Blue lines in Fig. 24 denotes this transition. On the other hand, in the CD and CP modes, the mode can be transited to itself if the following and preceding parameters are different.

The guard condition G in the definition 3.1 is as follows. The mode transition to the CV mode can occur when the calibrated airspeed in the previous mode meets the target calibrated airspeed in the CV mode. Therefore, $G(\cdot, CV) = \{V_{CAS}(V_T, h) = V_{target}\}$. Mode transition to the CM mode is very similar to the CV mode. This mode can occur when the airspeed in the previous mode meets the target Mach number in the CM mode; hence, $G(\cdot, CM) = \{M(V_T, h) = M_{target}\}$. On the other hand, a specific transition condition does not exist in either the CD or CP modes. Here altitude h or time t is selected as the mode transition condition. A summary of mode characteristics and respective transition condition is shown in Table 7.

Table 7: Mode characteristics and transition conditions

Mode	parameter	reduced state	transition cond.	accel.	decel.
CV	V_{CAS}	$[x_s \quad h]^T$	$V_T = f(V_{CAS}, h)$	X	O
CD	$\dot{h}$	$[V_T \quad x_s \quad h]^T$	h or t	O	O
CP	γ	$[V_T \quad x_s \quad h]^T$	h or t	O	O
CM	M	$[x_s \quad h]^T$	$V_T = f(M, h)$	O	X

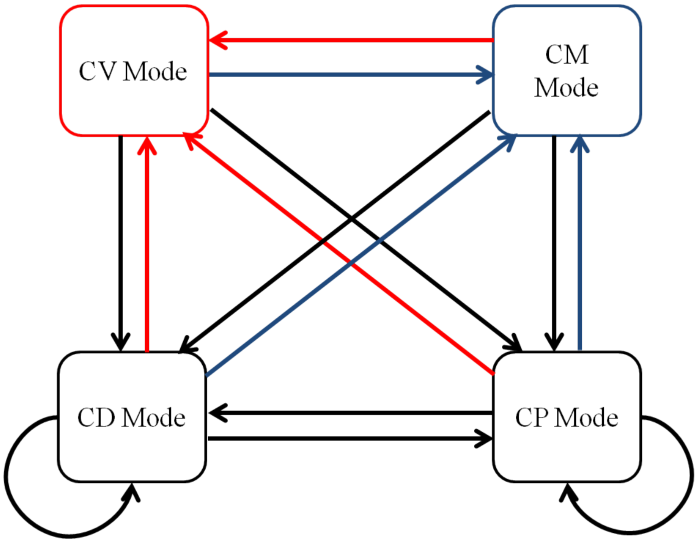

Figure 24: FMS modes for vertical trajectory generation.

3.7 Numerical Examples

To test the validity of the proposed trajectory generation method, a numerical simulation was performed. To evaluate the performance of trajectory generated by the proposed sequential method, aircraft specific relaxed optimal control problems were calculated with variations in RTA. These solutions have the lower bound performance of the original hybrid optimal control problems. The optimal solutions were calculated using the proposed method with the same conditions as the lower bound solutions, and the performances of the hybrid optimal solutions are evaluated by comparing the results to the lower bound performance.

3.7.1 Simulation condition

A simulation was performed for both B737-500 (B735) and B767-400 (B764) aircraft. BADA was used as the aircraft performance model. To simplify the problem, the lateral path was assumed to be a straight line. Since this chapter focuses on the systematic methodology to determine FMS input for a CDA profile generation, wind was simplified as a constant. The numerical values of the operational constraints using this numerical simulation are shown in Table 8. The boundary condition of the problem is the same as Park and Clarke used[48]. To solve the optimal control problem, a pseudospectral method was used along with many numerical optimal control schemes. There are several version of pseudospectral methods[61, 23]. In this numerical example, GPOPS[23] was used as a numerical solver for an optimal control problem with both a relaxed optimal control case and a fixed mode sequence hybrid optimal control case.

Table 8: Numerical values of constraints

	$\dot{h}[m/s]$	$V_{CAS}[kt]$ (B735/B764)	$\gamma[deg]$
min	-25.0	220/230	-6
max	-2.54	340/360	0

3.7.2 Results of Relaxed Optimal Control Problems

The optimal solutions of the relaxed optimal control problem were calculated for two performance indices: mintime and minfuel. These two results construct a feasible time range of a CDA flight with a given environmental condition[50]. The formulation of the ECP problem is applicable for general wind profiles, but since the feasible time range depends on the wind for setting a feasible RTA condition, the wind is assumed to be zero. In a zero wind condition, the feasible time range is 983.03 $\sim$ 1,130.06 sec for B735 and 972.39 $\sim$ 1,112.47 sec for B764, respectively. Considering the feasible flight time range of two aircraft, we pick three RTAs, which are 1,000 sec, 1,050 sec, and 1,100 sec, and calculate the fixed RTA minimum fuel trajectories. The trajectory performances of several cases for the B735 and B764 are shown in Table 9 and 10, respectively. These results give the lower bound of performance for the hybrid system approach.

Table 9: B735 optimal trajectory performances with various RTA conditions

Type	TOD (nm)	fuel (kg)	ETA (sec)
mintime	-103.32	416.24	983.03
RTA1000	-106.71	402.46	1000.00
RTA1050	-112.73	381.29	1050.00
RTA1100	-116.00	372.46	1100.00
minfuel	-117.06	371.16	1130.06

Table 10: B764 optimal trajectory performances with various RTA conditions

Type	TOD (nm)	fuel (kg)	ETA (sec)
mintime	-111.42	747.36	972.39
RTA1000	-116.83	702.70	1,000.00
RTA1050	-122.07	664.15	1,050.00
RTA1100	-124.54	650.78	1,100.00
minfuel	-124.85	650.27	1,112.47

3.7.3 Results of Hybrid Optimal Control Problems

The performance results from the proposed sequential method using the same performance indices and RTAs are shown in Table 11 and 12 for B735 and B764, respectively. The last two columns in the tables, segments and sequence, are the results of a trajectory partition and mode estimation of the sequential method. As shown in the tables, the estimated mode sequence is dependent on optimal type, RTA, and aircraft type. If the RTA is close to the lower limit, which is determined by the minimum time result, the CV mode with the maximum allowable CAS is inserted to increase the descent speed to meet the RTA condition. If the RTA is close to the upper bound, which is determined by the minimum fuel result, the mode sequence result is the same as that of the minimum fuel case. For the B735, the estimated mode sequence of the minimum fuel case is CD-CD-CD while for the B764 it has a CD-CV-CD sequence. The minimum time case of the B764 has an additional CM mode, when compared to the B735 case, to capture the constant Mach descent with the maximum allowable Mach number.

The performance gaps between the lower bound and the optimal solutions from the proposed method are very small for all simulation cases. The maximum performance gap is less than 0.5 kg in fuel burn, 0.02 NM in TOD, and 1 sec in the flight time for both the B735 and B764 simulations. In the minimum time case, two results; the relaxed optimal solution and the FMS applicable solution, are the same. As stated in chapter 2, the minimum time trajectory is determined at a maximum performance limit such as the maximum CAS/Mach and a maximum ROD/FPA. Therefore, it can be generated by a combination of FMS VNAV modes with maximum mode parameters.

Table 11: B735 optimal trajectory performances with various RTA conditions

Type	TOD (nm)	fuel (kg)	ETA (sec)	Segments	Sequence
mintime	-103.32	416.24	983.03	4	CP-CD-CV-CD
RTA1000	-106.71	402.46	1,000.00	5	CP-CD-CD-CV-CD
RTA1050	-112.74	381.33	1,050.00	3	CD-CD-CD
RTA1100	-116.00	372.46	1,100.00	3	CD-CD-CD
minfuel	-117.05	371.17	1,129.90	3	CD-CD-CD(CP)

Table 12: B764 optimal trajectory performances with various RTA conditions

Type	TOD (nm)	fuel (kg)	ETA (sec)	Segments	Sequence
mintime	-111.42	747.36	972.39	5	CP-CD-CM-CV-CD
RTA1000	-116.83	702.77	1,000.00	4	CP-CD-CD-CD
RTA1050	-122.07	664.16	1,050.00	3	CD-CD-CD
RTA1100	-124.56	650.95	1,100.00	3	CD-CV-CD
minfuel	-124.88	650.35	1,113.20	3	CD-CV-CD(CP)

The trajectory comparisons between the lower bound and the optimal solution from the sequential method for the B735 and B764 are shown in Figures 25 and 26, respectively. The left column represents the trajectories of the lower bound solutions, and the right column represents the optimal trajectories obtained by the sequential method. As shown in the Figures, the optimal speed and altitude profiles are quite similar to those of the lower bound solutions in all RTA cases. As mentioned above, the minimum time trajectories are identical in both cases. This result shows that the optimal solution from the sequential method have a very similar performance to the lower bound solution from the relaxed optimal control problems.

3.7.3.1 Results of Mode Estimation

In the sequential method, from STEP 1, the relaxed optimal control problem to STEP 3, the mode estimation is the procedure to find the optimal mode sequence to make a similar trajectory to the lower bound solution. Hence, if the mode sequence is fixed for all variations in wind, RTA, and aircraft type, the mode estimation procedure does not require an onboard calculation in the FMS. This procedure can be an offline mode sequence design procedure, and hence the computational load can be reduced significantly.

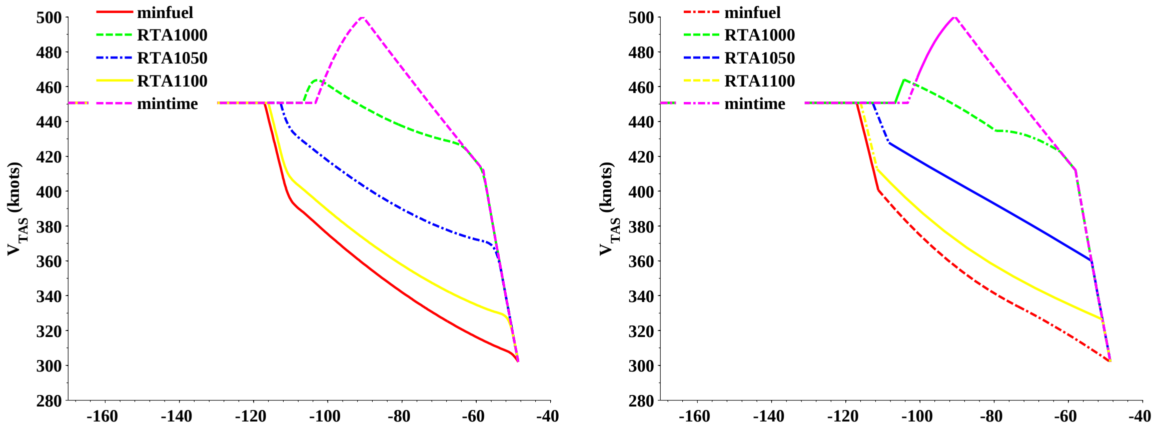

(a) Relaxed solution: TAS (b) Sequential Method: TAS

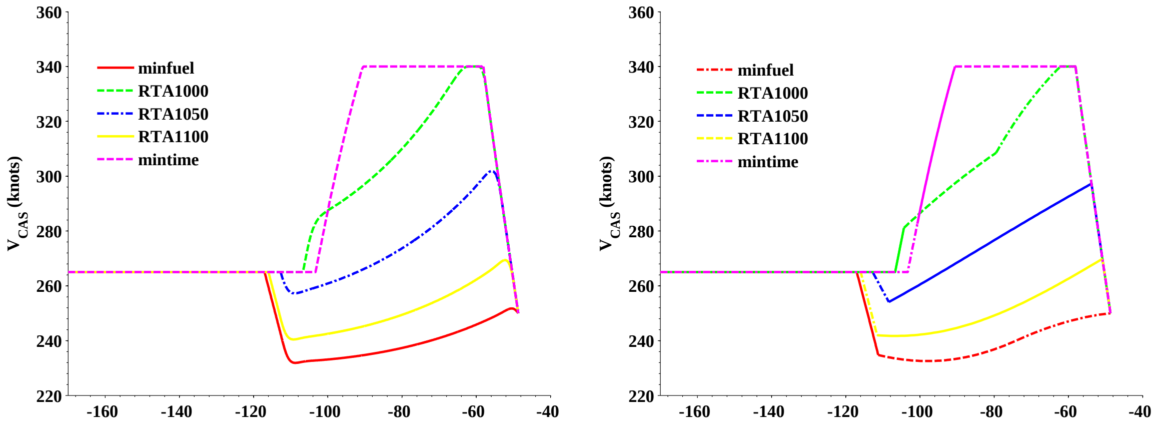

(c) Relaxed solution: CAS (d) Sequential Method: CAS

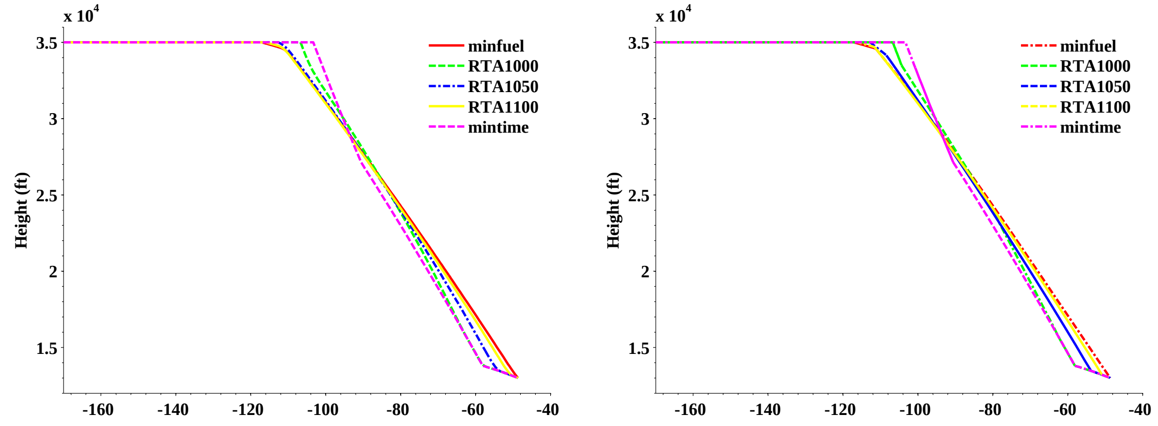

(e) Relaxed solution: Alt. (f) Sequential Method: Alt.

Figure 25: Comparison of the optimal solutions of B735

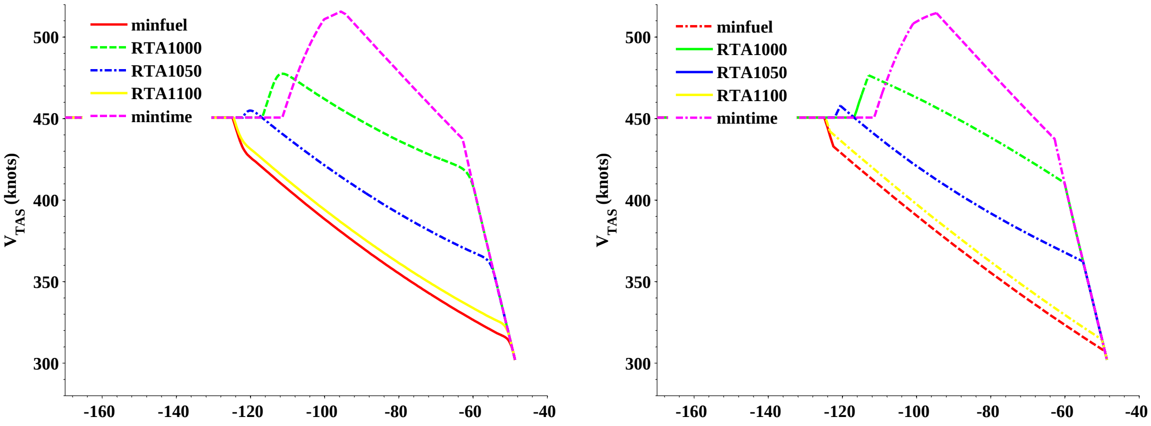

(a) Relaxed solution: TAS

(b) Sequential Method: TAS

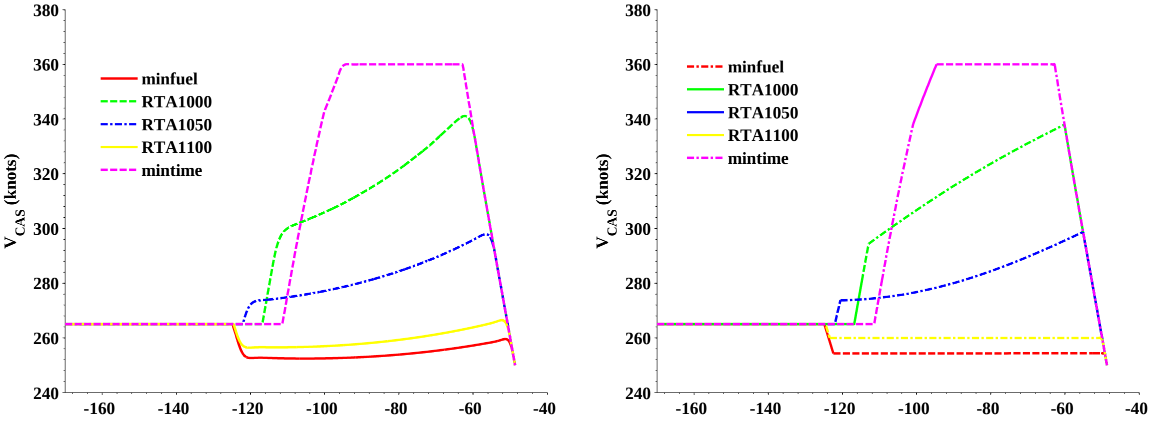

(c) Relaxed solution: CAS

(d) Sequential Method: CAS

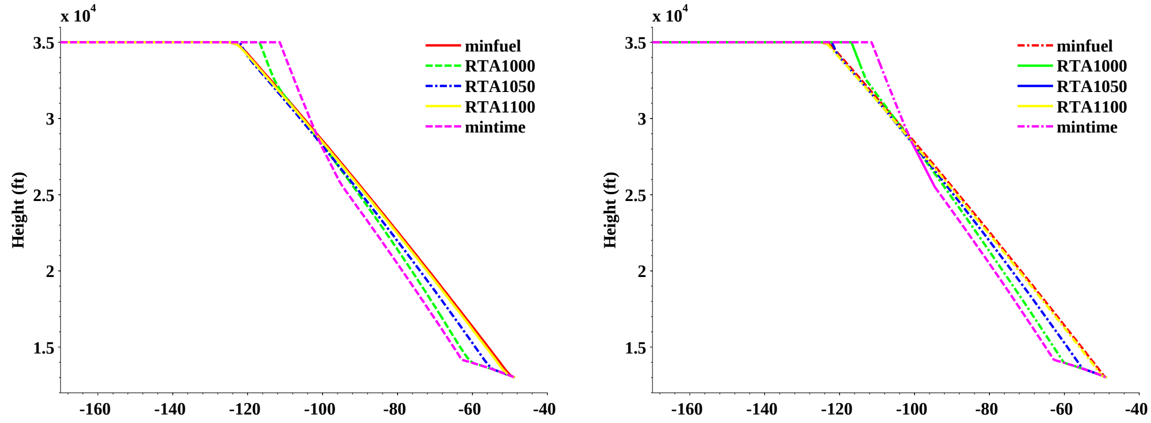

(e) Relaxed solution: Alt.

(f) Sequential Method: Alt.

Figure 26: Comparison of the optimal solutions of B764

In order to evaluate the possibility of this strategy and find a general optimal sequence of modes for a fixed RTA fuel optimal trajectory generation in the FMS if possible, we analyze the mode estimation procedure with various wind and RTA conditions. The mode estimation results with various RTA and wind conditions are shown in Table 13. Note that "tail" denotes a $20m/s$ tail wind, and a "head" denotes a -$20m/s$ head wind.

Using the proposed rule, there are a total of four partitioned segments for mintime trajectories applying three wind conditions; zero wind, a head wind, and a tail wind. The resulting estimated mode sequences were the same as $\{CP \quad CD \quad CV \quad CD\}$. This result is exactly the same as with previous research[49]. In this previous research, the minimum time CDA trajectory was generated with the existing VNAV function with the same VNAV mode sequence as in Table 13. In the mintime trajectories, the first two segments, the CP and the CD are for the maximum acceleration performance as shown in Fig.25 and 26. The first mode in the mintime cases is CP and its minimum cost is zero because the control input limit is active in this segment. However, the CD mode has very small cost values for all cases below 0.02. That means the CD mode can be an alternative mode for the first CP mode by accepting a small performance degradation.

The estimated mode sequence is $\{CP \quad CD \quad CD \quad CV \quad CD\}$ in and RTA of 1000 in a zero wind case. In this case, the first two CP-CD mode sequences are for the acceleration during descent, and the mode parameters were determined at the limit for maximum acceleration. The period of the CP mode is also very short and the cost value is very close to the CD mode. Therefore, similar to the minimum time case, the CP-CD mode can be approximated by only the CD mode. Another interesting observation is that all cases except the mintime case have three segments and same estimated mode sequence $\{CD \quad CD \quad CD\}$. Here, the parameters of each segment are different while the modes are the same, which means that the initial mode is a CD and all mode transitions are to the CD mode itself in Fig.24

By this analysis, we propose $\{CD \quad CD \quad CV \quad CD\}$ as a general optimal mode sequence for the fixed RTA minfuel trajectory. To cover the feasible time range determined by the minimum fuel and minimum time trajectories[48], a CV mode is added as the third

Table 13: B735 Mode sequencing algorithm results

Type	wind	segments	mode seq.
mintime	zero	4	$\{CP \quad CD \quad CV \quad CD\}$
RTA1000	zero	5	$\{CP \quad CD \quad CD \quad CV \quad CD\}$
RTA1050	zero	3	$\{CD \quad CD \quad CD\}$
RTA1100	zero	3	$\{CD \quad CD \quad CD\}$
minfuel	zero	3	$\{CD \quad CD \quad CD(CP)\}$
mintime	tail	4	$\{CP \quad CD \quad CV \quad CD\}$
RTA950	tail	3	$\{CD \quad CD \quad CD\}$
RTA1000	tail	3	$\{CD \quad CD \quad CD\}$
RTA1050	tail	3	$\{CD \quad CD \quad CD\}$
minfuel	tail	3	$\{CD \quad CD \quad CD(CP)\}$
mintime	head	4	$\{CP \quad CD \quad CV \quad CD\}$
RTA1100	head	4	$\{CP \quad CD \quad CD \quad CD\}$
RTA1150	head	3	$\{CD \quad CD \quad CD\}$
RTA1200	head	3	$\{CD \quad CD \quad CD\}$
minfuel	head	3	$\{CD \quad CD \quad CP(CD)\}$

segment. This is a means of covering all mode sequences in Table 13. If the time interval of the CV mode is small, we can make the trajectory similar to the trajectory generated by the three CD modes.

3.7.4 Results with Fixed Mode Sequence

The optimal trajectories with the proposed optimal sequence $\{CD \quad CD \quad CV \quad CD\}$ were calculated. The optimal profiles for the B735 with various RTA conditions are shown in Figure 27. These results show that the optimal profiles with a given structure are very similar to the lower bound solutions shown in Fig. 25. The numerical values of trajectories generated by the proposed method are shown in Table 14. The optimal parameters for modes of each case are shown in Table 15. These parameters are FMS inputs for generating minimum fuel trajectory with an RTA constraint.

The feasible time range of trajectories with the proposed structure is 983.08∼1,131.12 sec. This result shows that performance degradation by restricting the trajectory structure is negligible from the feasible time range point of view. In all cases, fuel burn differences from the lower bound are below 0.2 kg. From this result, it is concluded that optimal solutions with a fixed CD-CD-CV-CD mode have very similar performances when compared to those

Table 14: B735 minfuel FMS trajectory performances with various RTA condition

Type	TOD (nm)	fuel (kg)	ETA (sec)
mintime	-103.32	416.20	983.08
RTA1000	-106.64	402.60	1000.00
RTA1050	-112.74	381.33	1050.00
RTA1100	-116.00	372.46	1100.00
minfuel	-117.09	371.17	1131.12

Table 15: B735 optimal parameters of each mode with various RTA conditions

Type	CD($\dot{h}[m/s]$)	CD($\dot{h}[m/s]$)	CV($V_{CAS}[kt]$)	CD($\dot{h}[m/s]$)
mintime	-24.27	-25.00	340.00	-2.54
RTA1000	-16.05	-17.49	340.00	-2.54
RTA1050	-9.28	-12.62	296.87	-2.54
RTA1100	-2.54	-10.80	268.76	-2.54
minfuel	-2.54	-10.27	242.29	-9.59

of lower bound solutions in Table 9 or the optimal solutions from the sequential method in Table 11.

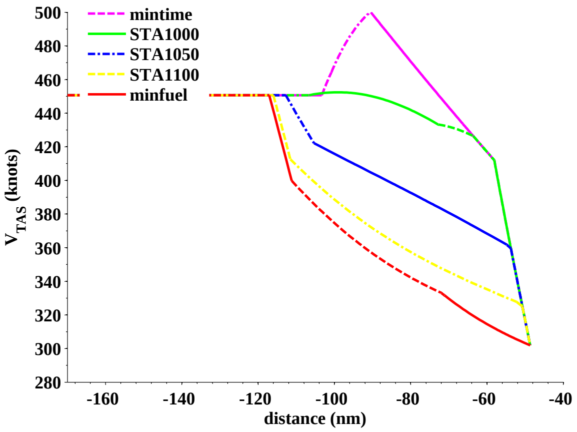

(a) TAS

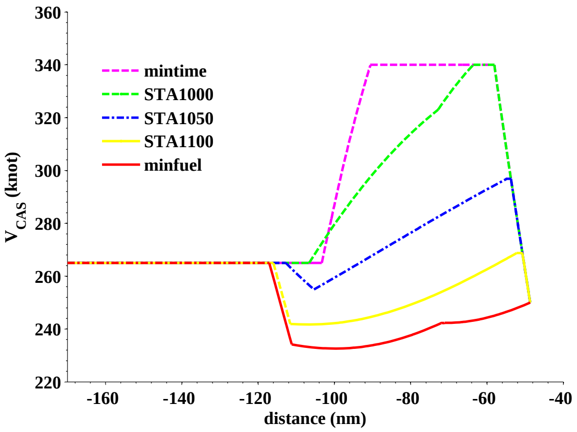

(b) CAS

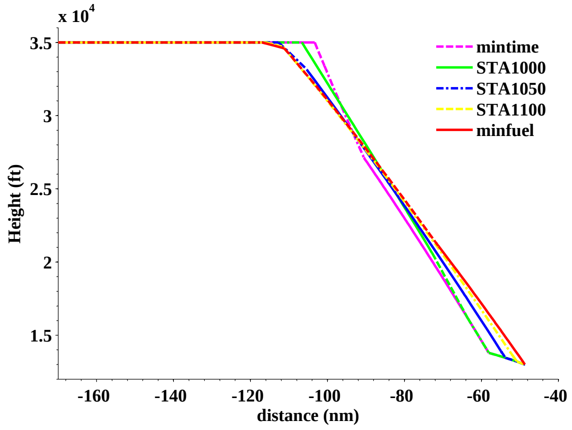

(c) Altitude

Figure 27: B735 Fixed Mode Sequence Solutions

3.8 Conclusion

The trajectory generation method in the FMS VNAV framework was addressed for the en-route descent portion of a CDA trajectory. For the successful CDA operation in the TRACON area, an RTA constraint is given at a meter fix. The FMS trajectory generation function was modeled as a hybrid system with four VNAV modes: CV, CD, CP, and CM. With a hybrid system model of the FMS VNAV function, the en-route trajectory generation problem was formulated as a hybrid optimal control problem. To design the trajectory structure, which is a mode sequence in a hybrid system, the sequential method, using the relaxed optimal solution was proposed. By analysis of the lower bound minimum fuel trajectories with variations in RTA and wind profiles, we designed a single sequence $\{CD \quad CD \quad CV \quad CD\}$. Since the mode sequence is fixed for a CDA en-route trajectory generation, the original hybrid optimal control problem was converted to a multi-phase optimal control problem which can be solved relatively easily. By solving this problem, optimal parameters of each mode are obtained, and these parameters are the FMS inputs of a designed VNAV mode sequence. The proposed trajectory structure was evaluated by numerical analysis, and the result showed that the performance of an optimal trajectory with a given structure are very similar to the lower bound performances in various conditions.

CHAPTER IV

ANALYSIS OF EN ROUTE DESCENT OPTIMAL TRAJECTORY

In this chapter, we analyze the relaxed optimal en-route trajectory formulated in chapter 3. To analyze the switching structure of the optimal solutions, we simplified the dynamics with small angle approximation. From the necessary conditions for optimality, we analyze the interior singular arc and boundary arc. Based on this analysis, the switching structure is analyzed, and it provides the mode sequence for the sequential method.

4.1 Introduction

In the previous chapter, the method to solve optimal control problems of switched systems was proposed and applied to the en-route descent trajectory generation problem using the FMS VNAV modes. The algorithm uses the optimal solution of the relaxed optimal control problem, and hence two optimal control problems have to be solved: the relaxed optimal control problem, and a fixed-mode optimal control problem of a switched system. The optimal mode sequence was analyzed for various wind and RTA conditions in the previous chapter, and the common optimal mode sequence solution covered almost all cases. By using this common mode sequence, the required computational load can be reduced.

An alternative method to reduce the computational time is to use analytic or semi-analytic solutions instead of directly solving the relaxed optimal control problem. In this chapter, we address the analysis of the en-route descent trajectory optimization problem by using simplified dynamics. The simplified dynamics have an affine formulation with respect to the control input, therefore, the optimal solution may have a singular arc as a part of the solution[44]. An analysis of this singular arc is necessary to acquire information regarding the structure of the optimal solution.

In the same framework as the previous chapter, the en-route trajectory optimization problem is formulated as a two-phase optimal control problem since the flight range covers the latter portion of the cruise segment. This original problem is converted to an equivalent single phase, free initial and final time optimal control problem with unknown cost index, which is similar to the approach in [9]. The optimal trajectory is analyzed based on the three possible subarcs; interior singular arc, nonsingular arc, and boundary arc. Based on the analysis of the switching structure of the optimal solution, an algorithm can be used to generate the optimal trajectory by forward and backward integration instead of solving an optimal control problem using a numerical optimization method. The solution from this proposed method can replace the solution of the relaxed optimal control problem. Furthermore, the optimal mode sequence can be directly estimated from this solution. In this manner, the computational time can be reduced significantly. The numerical examples are presented to demonstrate the validity of this proposed method.

4.1.1 Singular Optimal Control

The equation of motion of an aircraft can be formulated in a nonlinear affine form in control by using several assumptions such as a point mass and small angle approximation. Furthermore, in many applications, the cost functional depends only on the state variables; minimum time[46, 77], minimum fuel[7, 49, 48, 51], minimum DOC[8, 9, 21], minimum energy[76], and maximum distance[22]. For this reason, the singular arc can be a part of the optimal trajectory in those problems, and the singular optimal control have appeared in many works of literature about aircraft trajectory optimization problems[7, 8, 21, 22, 46, 76].

In this chapter, the aircraft equations of motion presented in Chapter 2 are simplified using a small angle approximation in the control input γ. As a result, the dynamics has a control affine form. In addition, the performance indices of interest; fuel cost and emissions cost are functions of vehicle state only (the detail formulation will be shown later). Therefore, the analysis of a singular arc is studied.

4.1.2 Necessary Conditions for State Inequality in Constrained Problems

Necessary conditions for the optimality of the optimal control problems with state inequality constraints have been studied in two ways: direct adjoining approach and indirect adjoining approach. In the direct adjoining approach, the necessary conditions are derived by directly adjoining the pure state inequality constraint to the cost functional with a Lagrange multiplier[35, 47]. On the other hand, in the indirect approach, the time derivative of the pure state inequality which contains control are adjoined to the cost functional with a Lagrange multiplier[6, 5]. The main difference of two approaches is the difference in the Euler-Lagrange equations. The relationship of the Lagrange multipliers of both approaches which are associated with state inequality or the time derivative of the state inequality are explained in section 5 of [35]. In this chapter, the direct adjoining approach is used to analyze the boundary arc conditions.

4.2 Mathematical Preliminaries

Presented in this section are a few theorems for analyzing the boundary arc on state inequality constrained optimal control problems. Jacobson and et al.[35] have studied the necessary conditions for the junction points between interior arc and boundary arc with the assumption that the Hamiltonian should be regular. The definition of regular Hamiltonian is as follows:

Definition 4.1. The Hamiltonian H is said to be *regular* if along a given $x(t)$, and $\lambda(t)$, $H(u, \bar{x}, \bar{\lambda})$ has a unique minimum u,$t \in [0, T]$.

Note that, if the cost functional is a function of the state variable only, and the dynamics has an affine form in control, Hamiltonian fails to be regular. Therefore, the junction theorems in [35] cannot be used in this case. Maurer[44] addressed this problem and derived the following two junction theorems to address this issue.

Theorem 4.1 (Theorem 5.1 in [44]). *Let t_1 be the time at which an interior nonsingular arc and a boundary arc of an optimal control u are joined. Let $u^{(r)}$, $r \geq 0$, be the lowest order derivative of u which is discontinuous at t_1 and let p be the order of state inequality and q be the order of a singular arc. Let $p \leq 2q + r$. If $\nu(t_1) > 0$, then $p + r$ is an even integer.*

Theorem 4.2 (Theorem 5.4 in [44]). *Let t_1 be a point where an interior singular arc and a boundary arc of an optimal control u are joined. Let q be the order of the singular arc* *and assume that the strengthened GLC-condition holds. Let* $u^{(r)}$, $r \geq 0$, *be the lowest order derivative of* u *which is discontinuous at* t_1 *and let* $p \leq 2q + r$. *Then* $\nu(t_1) = 0$, *and* $q + r$ *is an odd integer.*

Note that Theorem 4.1 is for the junction point between the interior nonsingular arc and boundary arc, and Theorem 4.2 is for the junction point between the interior singular arc and boundary arc.

4.3 Optimal Control Problem Formulation

In this section, we modify Problem 3.4 with simplified dynamics. First, we will introduce the new simplified dynamics and formulate the optimal control problem to be solved in this chapter.

4.3.1 Flight Dynamic Model

Since the lateral path of an arrival procedure is typically provided by the STAR, we consider only the vertical path or motion in this chapter. Furthermore, from the small angle approximation on γ , which results in $\sin\gamma \approx \gamma$ and $\cos\gamma \approx 1$, the aircraft equations of motion in Eq. (8) $\sim$ (13) in Chapter 2 can be simplified as follows:

$$\dot{V}_T = \frac{1}{m}(T - D) - g\gamma - V_T\gamma\left(c(V_T, h)\frac{dW_h}{dh} + s(V_T, h)\frac{dW_c}{dh}\right) \tag{66}$$

$$\dot{x}_s = c(V_T, h)V_T + W_h \tag{67}$$

$$\dot{h} = V_T\gamma \tag{68}$$

where, V_T is the true airspeed of aircraft, x_s is the along track distance from the runway threshold; h is the altitude; γ is the aerodynamic flight path angle; W_h and W_c are the altitude dependent horizontal wind speed and cross wind speed, respectively; dW_h/dh and dW_c/dh are the wind shear terms. $c(V_T, h) = \cos\psi_w$ and $s(V_T, h) = \sin\psi_w$. Here, the aircraft mass m is considered constant during the entire en-route descent phase similar to the assumption in Chapter 2. The lift force L and drag force D are given by

$$L = \frac{1}{2}\rho(h)V_T^2SC_L = mg \tag{69}$$

$$D(h, V_T) = \frac{1}{2}\rho(h)V_T^2SC_D(V_T, h, C_L) \tag{70}$$

where ρ is the air density which is a function of h, and C_L and C_D are the lift and the drag coefficients, respectively. The International Standard Atmosphere (ISA) model is used for $\rho(h)$. Assuming that the lift force is equal to gravity in Eq. (69), $C_L = C_L(V_T, h)$, the drag in Eq. (70) is a function of V_T and h also. During the descent segment, thrust T is set to flight idle thrust. Generally, as done in several airframe manufacturer's performance models and BADA, flight idle thrust is modeled as a function of V_T and h . Therefore, γ is the only control input during the flight idle descent segment.

4.3.2 Environmental Cost Indices

In this study, fuel burn and emission costs are used as environmental cost indices. Since the en-route descent trajectory consists of two phases; cruise and descent, the cost functional is defined as a summation of the cost of the cruise segment plus that of the flight idle descent segment. From the wind speed assumption, the ground speed is constant during the cruise flight. Therefore, the cost for the cruise phase can be expressed as the Mayer cost term. For this reason, the optimal control problem for the en route descent part of CDA is formulated as a single phase optimal control problem. The cost functional form is given by

$$J = K_{cr}(x_s(t_0) - d_{max}) + \int_{t_0}^{t_f} K_{des}(V_T, h)\ \mathrm{dt} \tag{71}$$

where K_{cr} is the cruise cost coefficient which is the cost per distance, and K_{des} is the flight idle descent cost coefficient which is the cost per time; d_{max} is the along track distance from the runway threshold to the initial waypoint of the CDA procedure; $x_s(t_0)$ is the Top of Descent (TOD) point. From Lemma 2.1, d_{max} does not affect the optimal solution if $d_{max} < x_s(t_0)$. Note that since the runway threshold is set as the origin, and d_{max} is set to a negative value, this inequality means d_{max} should be strictly farther than the TOD.

The fuel cost and emission cost can be expressed as follows:

- Fuel burn cost

$$\begin{aligned} K_{cr} &= \frac{\dot{f}_{cr}}{V_{cr}} \\ K_{des}(V_T, h) &= \dot{f}_{idle}(V_T, h) \end{aligned} \tag{72}$$

- Emission cost

$$\begin{aligned} K_{cr} &= \frac{EI_X \dot{f}_{cr}}{V_{cr}} \\ K_{des}(V_T, h) &= EI_X(V_T, h)\dot{f}_{idle}(V_T, h) \end{aligned} \tag{73}$$

where $\dot{f}_{cr}$ and $\dot{f}_{idle}$ denote fuel flow rate in the cruise segment and the flight idle descent segment, respectively; EI_X denotes the emission index, and subscript X denotes the emission gas types:CO, HC, and NO_x.

The emission index table can be obtained from the International Civil Aviation Organization (ICAO) engine exhaust emissions databank[1], and EI is interpolated by Boeing method2 (BM2) which is the EI correction method considering the airspeed and atmospheric conditions such as temperature, pressure, and humidity[16]. Since the flight idle fuel flow rate is a function of Mach number and h, EI obtained by BM2 is also a function of V_T and h. Therefore, K_{des} in Eq. (71) can be expressed as $K_{des}(V_T, h)$ in both the fuel and emission cost cases. Therefore, the combination of the two performance indices can be formulated as Eq. (71) also.

4.3.3 Constraints for CDA

The path constraints of Problem 3.4 are applied to the problem in this chapter. CAS bound, Mach number bound, Rate of Descent (ROD) bound, and flight path angle bound are accounted for in the flight envelope protection and passenger comfort consideration. Since CAS and Mach are functions of V_T and h, CAS/MACH bound constraints are the pure state inequality constraints. The detail formulations of these are in Eq. (51) and (61). Boundary conditions are given in Eq. (74) and (75). CAS speed and altitude constraints are usually given at a meter fix from the published STAR chart. The operational constraint in the terminal area is considered by adding the RTA constraint at the meter fix. The RTA is defined as a flight time from d_{max} to the meter fix. The initial descent time t_0 is the flight time associated with the cruise segment. The initial manifold in Eq. (76) is added for time continuity.

- Boundary conditions

$$V_T(t_0) = V_{T0}, \quad h(t_0) = h_0, \quad x_s(t_0) = \text{free}, \quad t_0 = \text{free} \tag{74}$$

$$V_T(t_f) = V_{Tf}, \quad h(t_f) = h_f, \quad x_s(t_f) = s_f, \quad t_f = \text{RTA} \tag{75}$$

$$x_s(t_0) \geq d_{max}, \quad \Phi(x_s(t_0), t_0) = (x_s(t_0) - d_{max})/V_{cr} - t_0 = 0 \tag{76}$$

4.3.4 Problem Formulation

By combining the flight dynamics, cost functionals, and constraints, the constrained optimal control problem for the en-route trajectory optimization is defined as follows:

Problem 4.1 (Original Problem)**.** Consider the following optimal control problem

$$\underset{\gamma}{\text{minimize}} \quad J \text{ in Eq. (71)}$$

s.t.

$$\begin{aligned}
&\dot{V}_T = \frac{1}{m}(T-D) - g\gamma - V_T\gamma\left(c(V_T,h)\frac{dW_h}{dh} + s(V_T,h)\frac{dW_c}{dh}\right)\\
&\dot{x}_s = c(V_T,h)V_T + W_h\\
&\dot{h} = V_T\gamma\\
&\dot{h}_{min} \leq \frac{dh}{dt} \leq \dot{h}_{max}\\
&\gamma_{min} \leq \gamma \leq \gamma_{max}\\
&V_{min,CAS} \leq V_{CAS}(t) \leq V_{max,CAS}\\
&M_{min} \leq M(t) \leq M_{max}\\
&\text{boundary conditions : Eq. (74)} \sim \text{(76)}
\end{aligned} \tag{77}$$

4.4 Analysis of the Optimal Trajectory

To analyze the optimal solution of the Problem 4.1, first we will find the equivalent free initial and final time optimal control problem. Then, we will analyze the necessary conditions using direct adjoining approaches in [28, 35] with the equivalent optimal control problem.

4.4.1 Equivalent Optimal Control Problem

Consider the following Problem 4.2 which is the mixed cost problem with free final time.

Problem 4.2 (Mixed Cost with free final time problem).

$$\begin{aligned} \min_{\gamma} \quad & J + c_t t_f \\ \text{s.t.} \quad & \\ & \text{dynamic constraints: Eq. (66)} \sim \text{(68)} \\ & \text{path constraints : Eq. (29)} \sim \text{(33)} \\ & \text{boundary conditions : Eq. (74)} \sim \text{(76) but } t_f \text{ is free} \end{aligned} \tag{78}$$

The following lemma shows that Problem 4.1 and 4.2 are equivalent if t_f of both problems are the same.

Lemma 4.1. *Assume that the optimal solution of Problem 4.1 is unique. The optimal solutions of the Problem 4.1 and the Problem 4.2 are identical if the optimal* t_f *of Problem 4.2 is the same as the RTA of Problem 4.1.*

Proof. Let $(\mathbf{x}_1, \gamma_1)$ and $(\mathbf{x}_2, \gamma_2)$ be the optimal solution pairs of Problem 4.1 and Problem 4.2, respectively. By this assumption, t_f are the same in both problems. Since the constraints of the two problems are the same, $(\mathbf{x}_1, \gamma_1)$ is a feasible solution of Problem 4.1 and vice versa. This implies the following two relationships:

$$J(u_2) + c_t t_f \leq J(u_1) + c_t t_f \tag{79}$$

$$J(u_1) \leq J(u_2) \tag{80}$$

From the above relations,

$$J(u_1) = J(u_2) \tag{81}$$

Therefore, $(\mathbf{x}_2, \gamma_2)$ is the optimal solution of Problem 4.1 and vice versa. From the assumption of the uniqueness, $(\mathbf{x}_1, \gamma_1) = (\mathbf{x}_2, \gamma_2)$. □

Consider the other optimal control problem:

Problem 4.3.

$$\min_{\gamma} \quad J = \int_{t_0}^{t_f} -\left(K_{cr} + \frac{c_t}{V_{cr}}\right)(cV_T + W_h) + K_{des}(V_T, h) + c_t \, \mathrm{dt}$$

s.t.

$$\begin{aligned} &\text{dynamic constraints: Eq. (66)} \sim \text{(68)} \\ &\text{path constraints : Eq. (29)} \sim \text{(33)} \\ &\text{boundary conditions : Eq. (74)} \sim \text{(76)} \end{aligned} \tag{82}$$

The following lemma shows that Problem 4.3 is equivalent to the Problem 4.2.

Lemma 4.2. *Let $x_s^*(t_0)$ be the optimal TOD of Problem 4.3. If $x_s^*(t_0) \geq d_{max}$, Problem 4.3 is equivalent to the Problem 4.2.*

Proof. Since $x_s^*(t_0) \geq d_{max}$, the optimal solution of Problem 4.3 is a feasible solution of Problem 4.2. Furthermore, adding constant term $\left(K_{cr} + \frac{c_t}{V_{cr}}\right)(x_s(t_f) - d_{max})$ to the cost functional of Problem 4.3 does not change the optimal solution. Hence, the optimal solution of Problem 4.3 is the optimal solution with the following cost functional:

$$J = \left(K_{cr} + \frac{c_t}{V_{cr}}\right)(x_s(t_f) - d_{max}) + \int_{t_0}^{t_f} -\left(K_{cr} + \frac{c_t}{V_{cr}}\right)(cV_T + W_h) + K_{des}(V_T, h) + c_t \, \mathrm{dt} \tag{83}$$

From Eq. (11)

$$x_s(t_f) - x_s(t_0) = \int_{t_0}^{t_f} cV_T + W_h \, \mathrm{dt}. \tag{84}$$

Substituting Eq. (84) into Eq. (83), we can get the equivalent cost functional

$$J = \left(K_{cr} + \frac{c_t}{V_{cr}}\right)(x_s(t_0) - d_{max}) + \int_{t_0}^{t_f} K_{des}(V_T, h) \, \mathrm{dt} + c_t(t_f - t_0) \tag{85}$$

Since $x_s(t_0) - d_{max} = t_0 V_{cr}$, by substituting this into Eq. (85), we can get the equivalent cost functional expressed as

$$J = K_{cr}(x_s(t_0) - d_{max}) + \int_{t_0}^{t_f} K_{des}(V_T, h) \, \mathrm{dt} + c_t t_f, \tag{86}$$

which is the same as the cost functional of Problem 4.2. Therefore, the optimal solution of Problem 4.3 is the optimal solution of Problem 4.2. □

From the Lemma 4.1 and 4.2, Problem 4.3 is equivalent to Problem 4.1 if t_f of both problems are the same. Hence, we use Problem 4.3 to derive the necessary conditions.

4.4.2 Necessary Conditions

The Hamiltonian for Problem 4.3 is defined as follows:

$$H = -K_{cr}^{t}(cV_T+W_h)+K_{des}(V_T,h)+c_t+\lambda_V(\frac{T-D}{m}-g\gamma-V_T\gamma\mathbf{W}_{h,\chi})+\lambda_x(cV_T+W_h)+\lambda_h V_T\gamma \tag{87}$$

where λ_V, λ_x, and λ_h are the costate variables corresponding to the state variables V_T, x_s and h, respectively. In Eq. (87), $K_{cr}^{t} = K_{cr} + \frac{c_t}{V_{cr}}$, and $\mathbf{W}_{h,\chi} = c\frac{dW_h}{dh} + s\frac{dW_c}{dh}$.

As stated previously, we follow a direct adjoining approach in [35] for the analysis of the necessary conditions. The Lagrangian L including path constraints is given by

$$L = H + \mu^T C(V_T,h,\gamma) + \eta^T S(V_T,h) \tag{88}$$

where inequality constraints $C(V_T,h,\gamma) : \mathbb{R}^3 \to \mathbb{R}^q$ and $S(V_T,h) : \mathbb{R}^2 \to \mathbb{R}^s$ represent mixed path constraints and pure state inequality in Problem 4.3, respectively; $\mu \in \mathbb{R}^q$ and $\eta \in \mathbb{R}^s$ are the Lagrange multipliers for mixed and pure state inequality constraints, respectively.

The following equations are the necessary conditions for the optimality of the Problem 4.3[28]. From the Euler-Lagrange equations,

$$\begin{aligned}
\dot{\lambda}_V &= -\frac{\partial L}{\partial V_T} \\
&= (K_{cr}^{t} - \lambda_x)\left(c + \frac{\partial c}{\partial V_T}V_T\right) - \frac{\partial K_{des}}{\partial V_T} \\
&\quad + \lambda_V(\frac{1}{m}\frac{\partial \tilde{D}}{\partial V_T} + \mathbf{W}_{h,\chi}\gamma + \frac{\partial \mathbf{W}_{h,\chi}}{\partial V_T}V_T\gamma) - \lambda_h\gamma - \mu^T\frac{\partial C}{\partial V_T} - \eta^T\frac{\partial S}{\partial V_T}
\end{aligned} \tag{89}$$

$$\dot{\lambda}_x = -\frac{\partial L}{\partial x_s} = 0 \tag{90}$$

$$\begin{aligned}
\dot{\lambda}_h &= -\frac{\partial L}{\partial h} \\
&= (K_{cr}^{t} - \lambda_x)\left(\frac{\partial c}{\partial h}V_T + \frac{dW_h}{dh}\right) - \frac{\partial K_{des}}{\partial h} \\
&\quad + \lambda_V(\frac{1}{m}\frac{\partial \tilde{D}}{\partial h} + V_T\gamma\frac{\partial \mathbf{W}_{h,\chi}}{\partial h}) - \mu^T\frac{\partial C}{\partial h} - \eta^T\frac{\partial S}{\partial h}
\end{aligned} \tag{91}$$

where $\tilde{D} = D - T$, which means the net drag force. From the Karush-Kuhn-Tucker

(KKT) conditions,

$$\begin{aligned} &\mu \geq 0, \quad \mu^T C(V_T, h, \gamma) = 0, \\ &\eta \geq 0, \qquad \eta^T S(V_T, h) = 0. \end{aligned} \tag{92}$$

The jump condition at a contact point or junction point t_i is as follows[35]:

$$\lambda_V(t_i^+) = \lambda_V(t_i^-) - \nu_i \frac{\partial S_a}{\partial V_T} \tag{93}$$

$$\lambda_x(t_i^+) = \lambda_x(t_i^-) - \nu_i \frac{\partial S_a}{\partial x} \tag{94}$$

$$\lambda_x(t_i^+) = \lambda_h(t_i^-) - \nu_i \frac{\partial S_a}{\partial h} \tag{95}$$

where S_a is an active state inequality. Since state inequalities are independent of time and x_s, for any time τ on the boundary arc where $S(V_T, h) = 0$, λ_x is continuous with respect to time at a junction or contact point.

$$\lambda_x(\tau^-) = \lambda_x(\tau^+) \tag{96}$$

The optimal control γ^o is determined by the following minimum principle[28]:

$$\gamma^o = \text{argmin}_{\gamma \in \Omega(V_T, h)} H \tag{97}$$

$$L_\gamma = H_\gamma + \mu^T C_\gamma = 0 \tag{98}$$

where $\Omega(V_T, h) = \{\, \gamma \mid C(V_T, h, \gamma) \leq 0 \,\}$ is the admissible control set, and is dependent on the state variable V_T and h.

From the initial manifold constraint in Eq. (76) and the initial and final time free conditions in Eq. (74) and (75), the following transversality conditions hold:

$$\lambda_x(t_0) = -\nu_0 \frac{\partial \Phi}{\partial x_s} = -\frac{\nu_0}{V_{cr}} \tag{99}$$

$$H(t_0) = \nu_0 \frac{\partial \Phi}{\partial t_0} = -\nu_0 \tag{100}$$

$$H(t_f) = 0 \tag{101}$$

where ν_0 is the Lagrange multiplier for the initial manifold.

The Hamiltonian is constant along the optimal trajectory since the Hamiltonian in Eq. (88) is not an explicit function of time. Hence, Eq. (100) and (101) imply

$$H(t) = -\nu_0 = 0 \quad \text{for} \quad t \in [t_0, t_f]\,. \tag{102}$$

Since λ_x is constant on the optimal trajectory from the Eq. (90) and (96). In addition, from (99) and (102),

$$\lambda_x(t) = -\frac{\nu_0}{V_{cr}} = 0 \quad \text{for} \quad t \in [t_0, t_f]\,. \tag{103}$$

The solution of the constrained optimal control problem can be grouped by two subarcs: the interior arc on which $S(V_T, h) < 0$ and the boundary arc on which at least one of the components of $S(V_T, h)$ is zero. Therefore, analyses of both subarcs are necessary to solve the constrained optimal control problem 4.3.

4.4.3 Interior Arc

First, assume that all the state constraints $S(V_T, h)$ are not active. Then η is set to zero. By the minimum principle in Eq. (97), the optimal control input γ is determined as

$$\gamma^o = \begin{cases} \gamma_{\max} & \text{if } H_\gamma < 0 \\ \tilde{\gamma} & \text{if } H_\gamma = 0 \\ \gamma_{\min} & \text{if } H_\gamma > 0 \end{cases} \tag{104}$$

where $\tilde{\gamma}$ is the singular control, and $\gamma_{\max}$ and $\gamma_{\min}$ are determined by $\Omega(V_T, h)$. The switching function H_γ in Eq. (104) is given by

$$H_\gamma = -\lambda_V(g + V_T\mathbf{W}_{h,\chi}) + \lambda_h V_T. \tag{105}$$

For the analysis of the singular arc, assume that H_γ is zero during a singular arc interval. Then, from the zero Hamiltonian in Eq. (102), the remaining term H_0 is

$$H_0 = -K_{cr}^t(cV_T + W_h) + K_{des} - \lambda_V\frac{\tilde{D}}{m} + c_t = 0. \tag{106}$$

The singular control and singular arc are obtained by the time derivatives of H_γ and Eq. (102) and (106). From $H_\gamma = 0$,

$$(g + V_T\mathbf{W}_{h,\chi}) = \frac{\lambda_h}{\lambda_V}V_T. \tag{107}$$

By differentiating Eq. (105) and inserting time derivatives of costate and state variables Eq. (107), $\dot{H}_\gamma$ is expressed as

$$\begin{aligned} \dot{H}_\gamma = K_{cr}^t &\left[-\left(c + \frac{\partial c}{\partial V_T}V_T\right)\frac{\lambda_h}{\lambda_V}V_T + \frac{\partial c}{\partial h}V_T^2 + V_T\mathbf{W}_{h,\chi}\right] + \frac{\partial K_{des}}{\partial V_T}\frac{\lambda_h}{\lambda_V}V_T - \frac{\partial K_{des}}{\partial h}V_T \\ &+ \frac{\lambda_V}{m}\left[\tilde{D}\left(\mathbf{W}_{h,\chi} + \frac{\partial \mathbf{W}_{h,\chi}}{\partial V_T}\right) + \frac{\partial \tilde{D}}{\partial h}V_T\right] - \frac{\lambda_h}{m}\left(\frac{\partial \tilde{D}}{\partial V_T}V_T + \tilde{D}\right) = 0. \end{aligned} \tag{108}$$

From $H_0 = H_\gamma = 0$, λ_V and λ_h can be expressed as

$$\begin{aligned} \frac{\lambda_V}{m} &= \frac{1}{\tilde{D}}(-K_{cr}^t(cV_T + W_h) + K_{des} + c_t) \\ \frac{\lambda_h}{m} &= \frac{\lambda_V}{m}\frac{1}{V_T}(g + V_T\mathbf{W}_{h,\chi}). \end{aligned} \tag{109}$$

By substituting Eq. (109) into Eq. (108), the final formulation of the singular arc $\Gamma_s(V_T, h)$ is obtained as

$$\begin{aligned} \Gamma_s(V_T, h) &= -\dot{H}_\gamma \tilde{D} \\ &= \left[-c_t + K_{cr}^t(cV_T + W_h) - K_{des}(V_T, h)\right]\left[V_T\frac{\partial \tilde{D}}{\partial h} - \frac{\partial \tilde{D}}{\partial V_T}(g + V_T\mathbf{W}_{h,\chi}) + \tilde{D}\frac{\partial \mathbf{W}_{h,\chi}}{\partial V_T}\right] \\ &\quad - \tilde{D}\left[K_{cr}^t\left(cg + \frac{W_h}{V_T}g - \left(c + \frac{\partial c}{\partial V_T}V_T\right)(g + V_T\mathbf{W}_{h,\chi}) + \frac{\partial c}{\partial h}V_T^2 + V_T\mathbf{W}_{h,\chi}\right)\right] \\ &\quad - \tilde{D}\left[-\frac{K_{des}}{V_T}g - \frac{c_t g}{V_T} + \frac{\partial K_{des}}{\partial V_T}(g + V_T\mathbf{W}_{h,\chi}) - \frac{\partial K_{des}}{\partial h}V_T\right] \\ &= 0 \end{aligned} \tag{110}$$

Since the singular arc $\Gamma_s(V_T, h)$ in Eq. (110) is not an explicit function of control γ, a second time derivative $\ddot{H}_\gamma$ is needed to obtain the analytic formulation of optimal singular control $\tilde{\gamma}$. From Eq. (66) and (68),

$$\begin{aligned} \ddot{H}_\gamma &= \frac{\partial \dot{H}_\gamma}{\partial V_T}\dot{V}_T + \frac{\partial \dot{H}_\gamma}{\partial h}\dot{h} \\ &= -\frac{\partial \dot{H}_\gamma}{\partial V_T}\frac{\tilde{D}}{m} + \left(-\frac{\partial \dot{H}_\gamma}{\partial V_T}(g + V_T\mathbf{W}_{h,\chi}) + \frac{\partial \dot{H}_\gamma}{\partial h}V_T\right)\gamma = 0 \end{aligned} \tag{111}$$

Hence,

$$\tilde{\gamma} = \frac{\partial \dot{H}_\gamma}{\partial V_T}\frac{\tilde{D}}{m}\left(-\frac{\partial \dot{H}_\gamma}{\partial V_T}(g + V_T\mathbf{W}_{h,\chi}) + \frac{\partial \dot{H}_\gamma}{\partial h}V_T\right)^{-1} \tag{112}$$

Furthermore, if the singular arc is a part of the optimal trajectory, the following Generalized Legendre-Clebsch (GLC) condition should be satisfied:

$$\frac{\partial}{\partial \gamma}\left[\frac{\mathrm{d}^2}{\mathrm{d}t^2}H_\gamma\right] \leq 0. \tag{113}$$

Proposition 4.1. *Assume that the solution of* $\Gamma_s(V_T, h) = 0$ *in Eq. (110) is unique for fixed* h *in every* $h \in \{h_f \leq h \leq h_0\}$. *Furthermore, suppose the following conditions are satisfied:*

1. $\frac{\partial \dot{H}_\gamma}{\partial V_T} > 0$ *on the singular arc in Eq. (110);*

2. $\frac{dV_T}{dh} \geq -(\frac{g}{V_T} + \mathbf{W}_{h,\chi})$ *holds;*

Then, the GLC condition in Eq. (113) holds on the singular arc in Eq. (110).

Proof. From Eq. (111) and (113),

$$\frac{\partial}{\partial \gamma}\left[\frac{\mathrm{d}^2}{\mathrm{d}t^2}H_\gamma\right] = -\frac{\partial \dot{H}_\gamma}{\partial V_T}(g + V_T\mathbf{W}_{h,\chi}) + \frac{\partial \dot{H}_\gamma}{\partial h}V_T. \tag{114}$$

From the Implicit Function Theorem, $\frac{dV_T}{dh} = -\frac{\partial \dot{H}_\gamma/\partial h}{\partial \dot{H}_\gamma/\partial V_T}$. Hence, the condition 2 implies that

$$-\frac{\partial \dot{H}_\gamma/\partial h}{\partial \dot{H}_\gamma/\partial V_T} \geq -(\frac{g}{V_T} + \mathbf{W}_{h,\chi}),$$

and hence GLC condition in Eq. (113) holds with the condition 1 and Eq. (114). □

Remark 3. The assumption of the uniqueness of the solution of $\Gamma_s(V_T, h) = 0$ implies that $\Gamma_s(V_T, h)$ value of the right side of the singular arc in the $V_T - h$ diagram is either positive or negative. Condition 1 in Proposition 4.1 implies that the right side of curve has a positive $\dot{H}_\gamma$, and hence $\Gamma_s < 0$ ($\Gamma_s = -\dot{H}_\gamma\tilde{D}$). In both minimum fuel and minimum NO_x cases, this condition is satisfied as shown in Fig. 28 and 29.

Remark 4. In nominal wind case $\mathbf{W}_{h,\chi} \geq 0$. Hence, the right side of the condition 2 in Proposition 4.1 is negative. Figures 28 and 29 show that the singular arcs with various c_t values satisfy the condition 2 in Proposition 4.1.

As shown in Figures 28 and 29, conditions 1 and 2 in Proposition 4.1 holds for various c_t values, and hence GLC condition holds.

4.4.4 Boundary Arc

In the analysis of boundary arc, it is assumed that the mixed state inequality $C(V_T, h, \gamma)$ is not active on the boundary arc. Therefore, $\mu(t) = 0, t \in [t_1, t_2]$. This assumption is reasonable because the flight path angle during the flight idle descent with maximum/minimum constant MACH/CAS is within the bound of the flight path angle limit. This assumption implies that the boundary arcs are singular arcs.

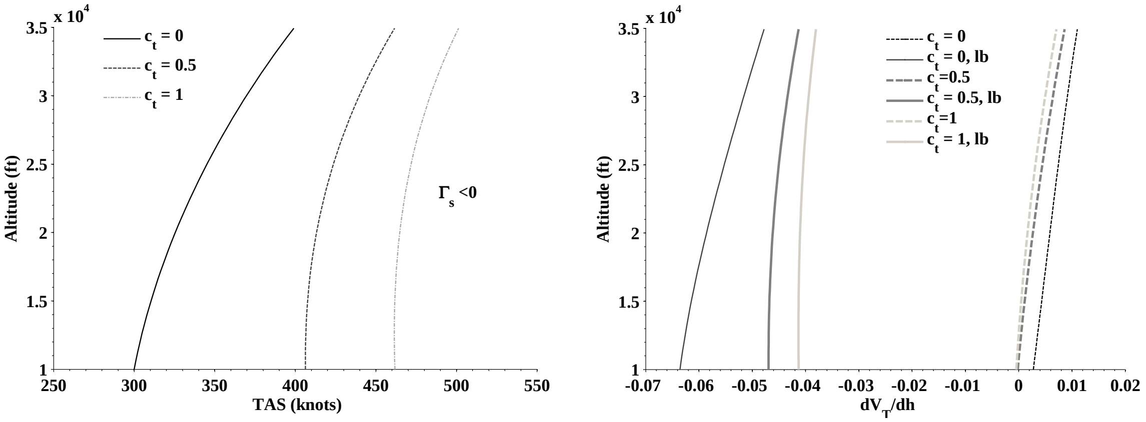

(a) Singular arc (b) Slope

Figure 28: B737-500 minimum fuel singular arc and slope in various c_t values

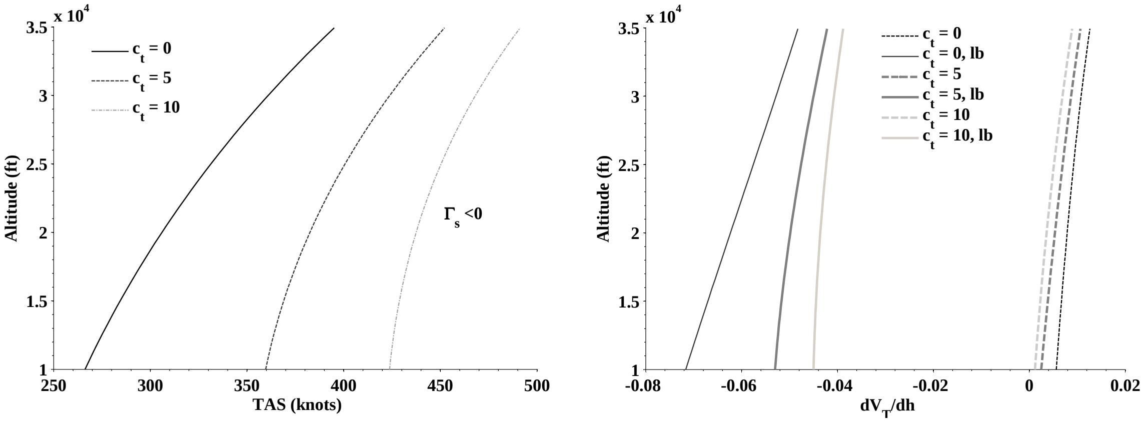

(a) Singular arc (b) Slope

Figure 29: B737-500 minimum NO_x singular arc and slope in various c_t values

The following conditions are the necessary conditions for the optimality when the optimal trajectory has boundary arc intervals:

$$\begin{aligned} L_\gamma(V_T, h, \gamma, \lambda_V, \lambda_h) = H_\gamma = 0 &\qquad \text{in Eq. } (105) \\ H_0(V_T, h, \lambda_V, \lambda_h) = 0 &\qquad \text{in Eq. } (106) \\ S_a(V_T, h) = 0 & \\ \dot{S}_a(V_T, t, \gamma) = 0 & \\ \dot{\lambda}_V = -\frac{\partial H}{\partial V_T} - \eta_a \frac{\partial S_a}{\partial V_T} & \\ \dot{\lambda}_h = -\frac{\partial H}{\partial h} - \eta_a \frac{\partial S_a}{\partial h} & \\ \eta_a(t) \geq 0, \quad t \in [t_1, t_2] & \end{aligned} \tag{115}$$

The active state inequality constraint $S_a = 0$ gives the relationship between V_T and h. Since $S_a(V_T, h)$ is the first order state inequality in this problem, which means that γ related terms revealed in the first time derivative $\dot{S}_a$, γ on the boundary arc can be obtained from the $\dot{S}_a = 0$, and it has an explicit formulation as

$$\gamma_{ba} = -\left[\frac{\partial S_a}{\partial V_T}(g + V_T \mathbf{W}_{h,\chi}) - \frac{\partial S_a}{\partial h} V_T\right]^{-1} \frac{\partial S_a}{\partial V_T} \frac{\tilde{D}}{m}. \tag{116}$$

Lemma 4.3. *If the boundary arc is a part of the optimal trajectory, the Lagrange multiplier of the active state inequality η_a is expressed as*

$$\eta_a = -\frac{m\gamma_{ba}}{\tilde{D}^2} \Gamma_s(V_T, h) \frac{\partial S_a}{\partial V_T}^{-1} \tag{117}$$

where, $\Gamma_s(V_T, h)$ is in Eq. (110).

Proof. Since boundary arc is a singular arc by the assumption, $H_\gamma = \dot{H}_\gamma = 0$. From the time derivative of Eq. (105),

$$\dot{H}_\gamma = \dot{H}_{\gamma s} + \eta_a \left[\frac{\partial S_a}{\partial V_T}(g + V_T \mathbf{W}_{h,\chi}) - \frac{\partial S_a}{\partial h} V_T\right] = 0, \tag{118}$$

where $\dot{H}_{\gamma s}$ is the same as Eq. (108), and hence $\dot{H}_{\gamma s} = \frac{-\Gamma_s}{\tilde{D}}$.

From Eq. (116),

$$\left[\frac{\partial S_a}{\partial V_T}(g + V_T \mathbf{W}_{h,\chi}) - \frac{\partial S_a}{\partial h} V_T\right] = -\frac{\tilde{D}}{m\gamma} \frac{\partial S_a}{\partial V_T}. \tag{119}$$

Eq. (117) is obtained by substituting Eq. (119) into Eq. (118). ☐

Note that $\Gamma_s(V_T, h)$ is not zero for $\forall \tau \in [t_1, t_2]$ on the boundary arc, where $[t_1, t_2]$ is the boundary arc interval.

Proposition 4.2. *If the boundary arc is a part of the optimal trajectory, $\Gamma_s(V_T, h) \frac{\partial S_a}{\partial V_T} \geq 0$ on the boundary arc.*

Proof. From the necessary condition in Eq. (115), $\eta_a \geq 0$. From Lemma 4.3, $-m\gamma/\tilde{D}^2$ is always positive during the descent. Therefore, if the boundary arc is a part of the optimal trajectory, $\Gamma_s(V_T, h) \frac{\partial S_a}{\partial V_T}$ should be nonnegative on the boundary arc. ☐

The possible boundary arc that satisfies the necessary condition is obtained by Proposition 4.2. The analysis of the possible boundary arcs of the CAS bound are shown in Fig. 30. The bold lines represent the possible boundary arcs that can be a part of optimal trajectory when a singular arc crosses the state inequality bound. Though the CAS bound case in Eq. (29) is considered only in Fig. 30, the MACH bound case can be analyzed in the same manner.

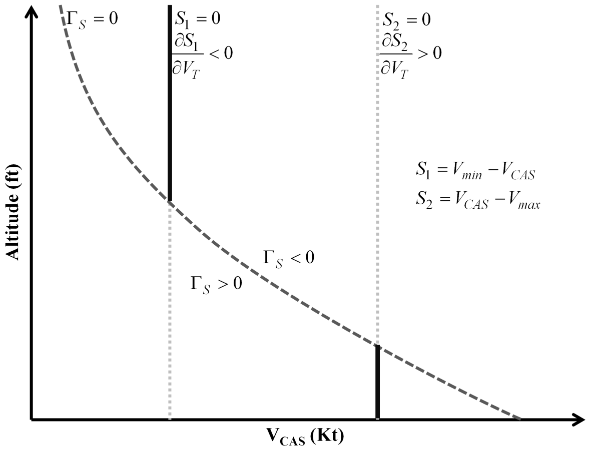

Figure 30: Boundary arcs satisfying necessary conditions

4.4.5 Continuity of Adjoint Variables

The adjoint variables λ_V and λ_h can be discontinuous at the junction point of the boundary arc from the jump condition in Eq. (93) $\sim$ (95). In addition, the adjoint variables can have discontinuities at any time for the boundary arc interval $[t_1, t_2]$[28]. Since the boundary arc is a singular arc from the assumption that $C(V_T, h, \gamma) < 0$, λ_V and λ_x have the same formulations with those in the interior singular arc in Eq. (109). This implies that λ_V and λ_h are continuous on the boundary arc. Therefore, the only possible discontinuous points are the junction points of the boundary arc. The following lemmas shows the continuity of the adjoint variables at the junction points of the boundary arc.

Lemma 4.4. *Both λ_V and λ_h are continuous at time t_1 at which an interior nonsingular arc and a boundary arc of an optimal control u are joined.*

Proof. Let $u^{(r)}$, $r \geq 0$, be the lowest order derivative of u which is discontinuous at t_1, and let p be the order of state inequality, and q be the order of singular arc. Here, $r = 0$, and $p = 1$ from the Eq. (110). Therefore, $p + r = 1$ which is an odd integer. From the junction point theorem 5.1 in [44], since $p + r$ is an odd integer, $\nu(t_1) = 0$. This implies that λ_V and λ_h are continuous at t_1 with the Eq. (93) and (95). □

Lemma 4.5. *Assume that the strengthened GLC-condition holds. Then, both* λ_V *and* λ_h *are continuous at time* t_1 *at which an interior singular arc and a boundary arc of an optimal control* u *are joined.*

Proof. Let $u^{(r)}$, $r \geq 0$, be the lowest order derivative of u which is discontinuous at t_1, and let p be the order of state inequality, and q be the order of singular arc. In this problem, $q = 1$ from the Eq. (110) and $p = 1$ from the CAS/MACH formulation. This implies $p \leq 2q + r$. Therefore, $\nu(t_1) = 0$ from the junction point theorem 5.4 in [44]. Hence, λ_V and λ_h are continuous at t_1 from the Eq. (93) and (95). □

The above two lemmas conclude the following proposition.

Proposition 4.3. *Both* λ_V *and* λ_h *are continuous on the entire optimal trajectory.*

Proof. From Lemma 4.4 and 4.5, both λ_V and λ_h are continuous at junction points where a boundary arc and an interior arc are joined. In addition, λ_V and λ_h are continuous on both interior arc and boundary arc from Eq. (89) and (91). Hence, λ_V and λ_h are continuous for the entire optimal trajectory. □

4.5 Optimal Trajectory Generation

In this section, we present the optimal trajectory generation algorithm based on the analysis results in the previous section. The algorithm consists of two parts: the optimal trajectory generation of Problem 4.3 with given c_t, and the finding of c_t to meet the RTA constraint. The overall procedure of the trajectory generation method is shown in Figure 31.

The algorithm A in Figure 31 generates the optimal trajectory by the combination of a nonsingular arc, an interior singular arc, and a boundary arc. The trajectory is calculated by forward and backward integrations without solving the optimal control problem directly.

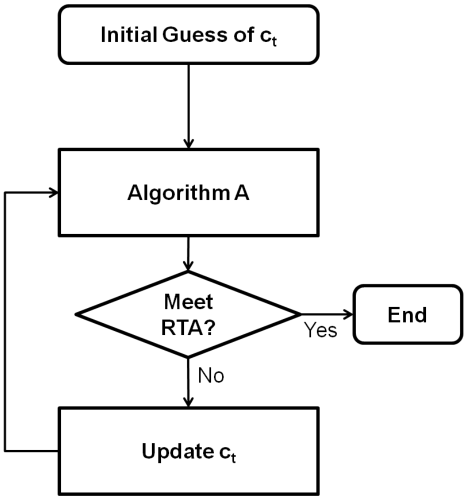

Figure 31: Algorithm

Therefore, it can be implemented in the FMS without additional computational capability. For the updating c_t to meet the RTA constraint, the gradient of RTA $\frac{dRTA}{dc_t}$ should be calculated. In this thesis, this gradient is calculated numerically.

4.5.1 Algorithm A

The proposed optimal trajectory generation algorithm is as follows:

STEP 1. Find the singular arc $\Gamma_s(V_T, h) = 0$ in Eq. (110) using a numerical method (In this thesis, Newton-Raphson method is used).

STEP 2. Find the initial segment of the optimal trajectory by forward integration of the equations of motion in Eq. (66) $\sim$ (68) from the initial point with either γ_{max} or γ_{min} in $\Omega(V_T, t)$. The control input is determined so that the trajectory moves toward the singular arc. The integration stops when the trajectory reaches either the possible boundary arc or the interior singular arc.

STEP 3. Find the last segment of the optimal trajectory by backward integration of the equations of motion from the terminating point with either γ_{max} or γ_{min} in $\Omega(V_T, t)$. The control input is determined so that the trajectory moves toward the singular arc. The backward integration stops when the trajectory reaches either the possible boundary arc or the interior singular arc.

STEP 4. Calculate the trajectory from the junction point of STEP 2 to the junction point of STEP 3 following either the boundary or interior singular arc.

In STEP 4, if the type of the junction points in STEP 2 and 3 are different, the trajectory generated in STEP 4 is switched from singular arc to the boundary arc or vice versa at least once.

The expected optimal trajectories with different c_t values are shown in Fig. 32. Since the singular arc $\Gamma_s(V_T, h) = 0$ changes according to c_t, the possible boundary arcs changes according to Proposition 4.2. The nonsingular controls in STEP 2 and 3 can be changed based on c_t value also. Therefore, c_t is one of the significant factors in determining the structure of the optimal trajectory as shown in Fig. 32. In case 1 of Fig. 32, junction points of STEP 2 and STEP 3 are on the boundary arc for the lower CAS bound, and interior singular arc, respectively. Therefore, the structure of the optimal trajectory is a nonsingular arc with γ_{max} - boundary arc for the lower CAS bound - interior singular arc - nonsingular arc with γ_{min}. On the other hand, the junction points of STEP 2 and STEP 3 in case 2 are the interior singular arc and boundary arc, respectively. Therefore, the structure of the optimal trajectory is a nonsingular arc with γ_{min} - interior singular arc - boundary arc for the upper CAS bound - nonsingular arc with γ_{max}.

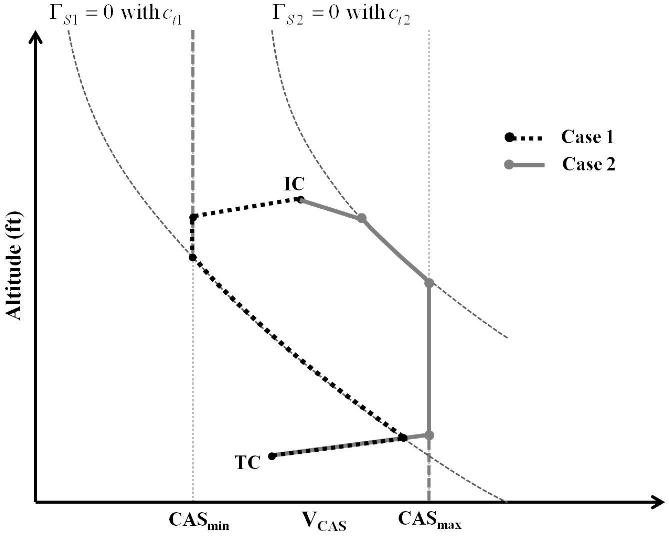

Figure 32: Structure of the optimal trajectory

4.5.2 Optimality Check

In this trajectory generation algorithm, we assume that the initial and the final parts of the trajectory, which move toward the singular arc in STEP 2 and 3, are parts of the optimal solution. To check if these parts are satisfied the necessary conditions, the sign of H_γ should be known. From the Proposition 4.3, the adjoint variables λ_V and λ_h are continuous at the junction points in STEP 2 and 3. Therefore, the values of λ_V and λ_h at junction point are known from Eq. (98) and (106). From Eq. (102), λ_V can be expressed as a function of V_T, h, and λ_h. Then Eq. (91) is expressed as follows:

$$\dot{\lambda}_h = K_{cr}^t \left(\frac{\partial c}{\partial h} V_T + \frac{dW_h}{dh}\right) - \frac{\partial K_{des}}{\partial h} + \frac{\lambda_h V_T \gamma + (K_{des} - K_{cr}^t(cV_T + W_h))}{\tilde{D} + m\left(g + V_T \mathbf{W}_{h,\chi}\right)\gamma} \left(\frac{\partial \tilde{D}}{\partial h} + m\gamma V_T \frac{\partial \mathbf{W}_{h,\chi}}{\partial h}\right). \tag{120}$$

From the continuity of λ_h, the values of λ_h at the junction points in STEP 2 and STEP 3 are known. The value at the junction point in STEP 2 is the final value of the initial segment, and the value of STEP 3 is the initial value of the final segment. By integrating Eq. (120) with the known values at the junction points in the backward direction along the initial segment or in the forward direction along the final segment, $\lambda_h(t)$ can be calculated. From $H = 0$ and known λ_h, λ_V also can be calculated. Therefore, the time history of H_γ is obtained from Eq. (105), and the optimality condition can be verified by Eq. (104). The trajectory generated by the proposed algorithm has satisfied this necessary condition, as will be shown by numerical examples.

4.6 Numerical Example

Both the minimum fuel and NO_x trajectories with various RTA and wind conditions are analyzed using two aircraft types: B737-500 (B735) and B767-400 (B764). Since K_{des} and $\tilde{D}$ are functions of V_T and h, which are quite general, various performance models can be adopted for the formulation derived in previous sections. BADA from EuroControl[2] is used as a performance data in this chapter. The boundary conditions are given in Table 16. The maximum range d_{max} is set to -150 NM, which is large enough to satisfy the assumption in Lemma 4.2. The numerical values of the path constraints in Eq. (29) $\sim$ (33) are given in Table 17.

Table 16: Boundary condition for numerical example

Initial Condition			Final Condition		
V_{CAS} (Kt)	h (ft)	x_s (NM)	V_{CAS} (Kt)	h (ft)	x_s (NM)
265	35,000	$> d_{max}$	250	13,000	-40

Table 17: Path constraints of B735 and B764

	B737-500		B767-400	
	min	max	min	max
MACH	0.45	0.82	0.45	0.86
CAS (Kt)	220	340	230	360
ROD (m/s)	-25.0	-2.54	-25.0	-2.54
γ (deg)	-6	0	-6	0

4.6.1 Fuel optimal trajectory

The structure of the optimal trajectory depends on the RTA constraint. The RTA effect on the fuel optimal trajectories are shown in Fig. 33 for B735 and Fig. 34 for B764. Here, RTA is given as the flight time from d_{max} to the meter fix, which is the terminal point in Table 16. As RTA increases, the types of the first and the last nonsingular arcs changes from the γ_{min}, which represents either the maximum ROD or the maximum descent angle, to the γ_{max}, which represents the minimum ROD.

The RTA curve as a function of c_t and the pareto curve between RTA and fuel performance are shown in Fig. 35. Since c_t represents the ratio between time and fuel costs, the RTA decreases as c_t value increases. At a certain point, the RTA does not decrease with c_t increases. The RTA converges to the minimum value, which is the minimum time case in Fig. 33. In the minimum time case, the singular arc with given c_t value is larger than the upper bound of MACH/CAS, and hence the structure of the trajectory is the nonsingular arc - boundary arc with the maximum MACH/CAS - nonsingular arc. On the other hand, if c_t is zero, the trajectory represents the minimum fuel case in Fig. 33.

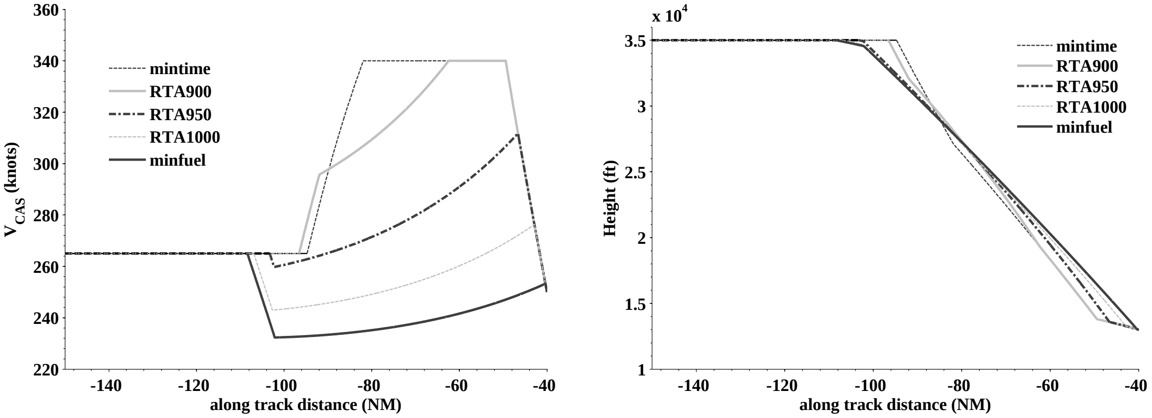

(a) Speed profiles (b) Altitude profiles

Figure 33: Fuel optimal trajectories of B735 with various RTA conditions. Wind is zero.

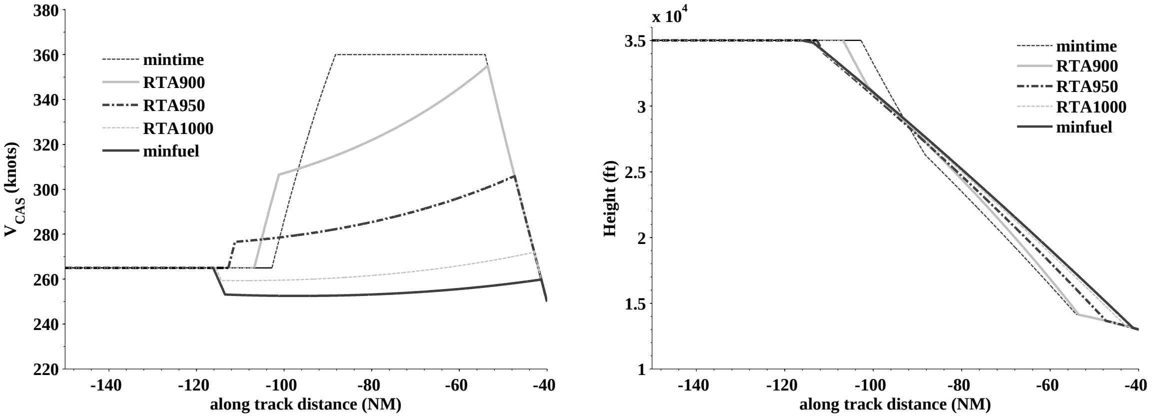

(a) Speed profiles (b) Altitude profiles

Figure 34: Fuel optimal trajectories of B764 with various RTA conditions. Wind is zero.

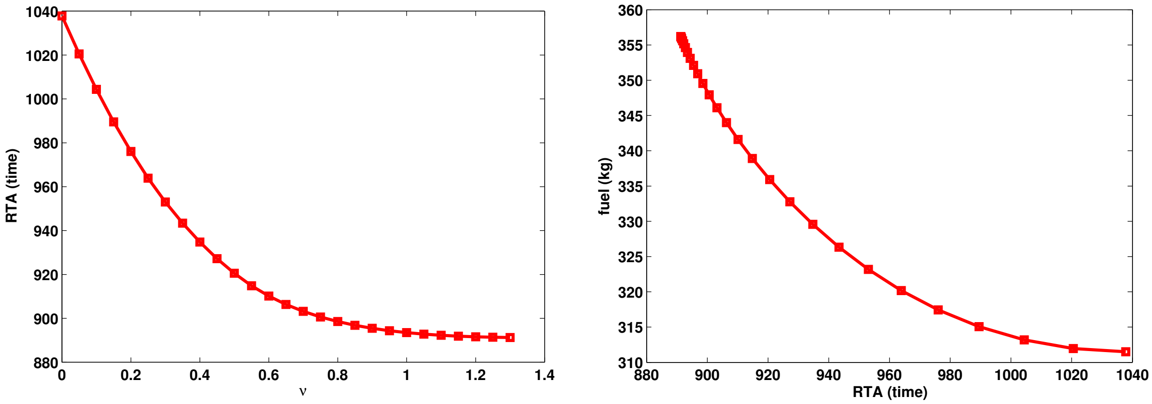

(a) Speed profiles (b) Pareto curves

Figure 35: Performance bound results of B735 with various c_t. Wind is zero.

4.6.1.1 Horizontal Wind Effect

The fuel optimal trajectories with various wind conditions with a given 950 sec RTA are shown in Fig. 36 and 37. The positive/negative wind represents the tail/head wind case. The wind affects the structure of the optimal trajectory. In the B735 case, the optimal trajectory includes the boundary arc on the upper bound of CAS when wind is -10 m/s. The wind also affects the TOD point. The TOD points moves farther from the runway as wind increases (tail wind increases). The type of nonsingular arc is changed according to wind. In a strong tail wind case, the initial bang is the γ_{max} to decelerate for both B735 and B764. However, in the tail wind case, the initial bang is the γ_{min} for the steepest descent.

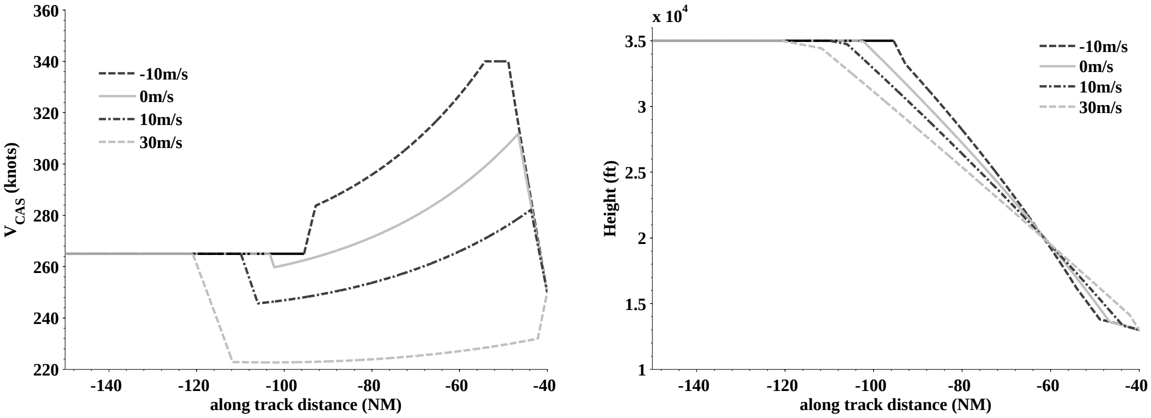

(a) Speed profiles (b) Altitude profiles

Figure 36: Fuel optimal trajectories of B735 with various wind conditions (RTA:950 sec).

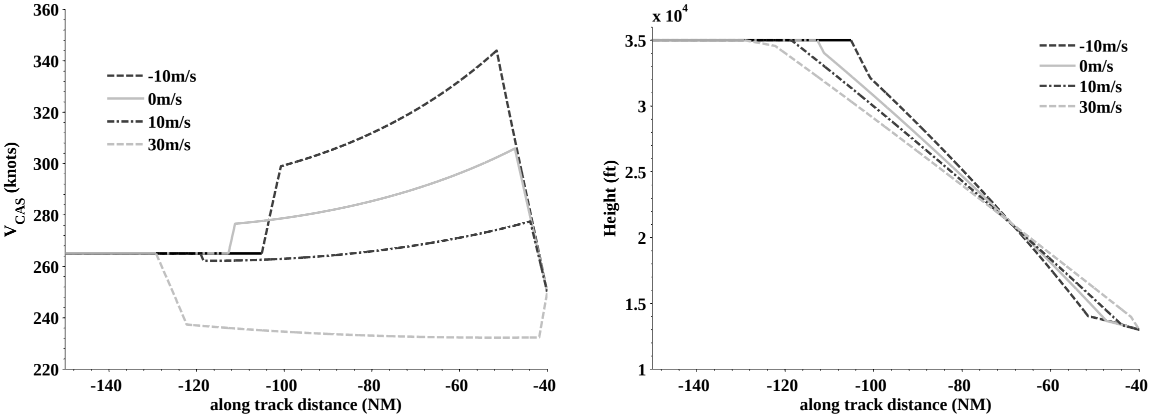

(a) Speed profiles (b) Altitude profiles

Figure 37: Fuel optimal trajectories of B764 with various wind conditions (RTA:950 sec).

4.6.1.2 Cross wind effect

To evaluate the cross wind effect, we compare two different cross wind cases, $W_c = 0m/s$ and $30m/s$, in which horizontal wind components are both zero (RTA is set to 800 sec). The optimal trajectories of both the B735 and B764 are shown in Fig. 38 and 39. The optimal structures for two different cross wind cases are the same; nonsingular - singular - boundary - nonsingular arc. The cross wind component affects the singular arc to meet the same RTA constraint at a meter fix. For a stronger cross wind, one has higher speed on the singular arc, and hence the TOD point moves toward runway threshold. Therefore, for the correct prediction of TOD, the cross wind should be considered in the formulation.

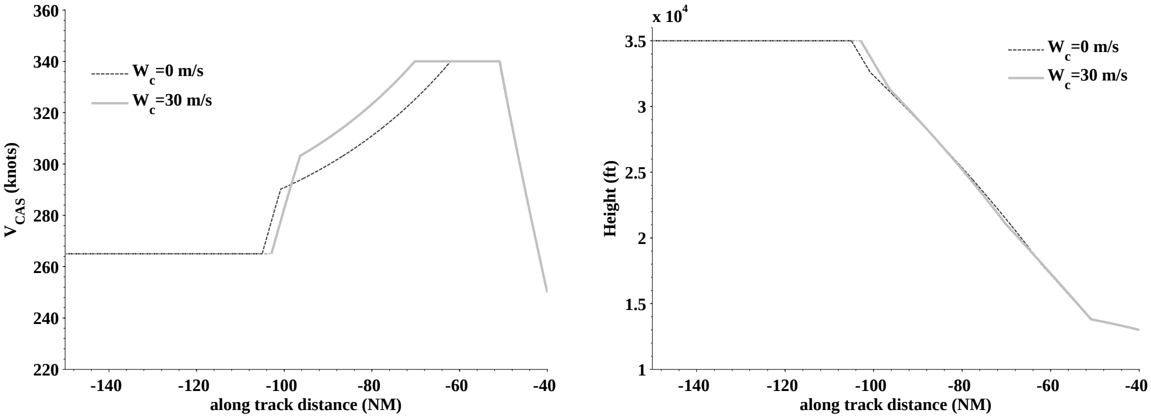

(a) Speed profiles (b) Altitude profiles

Figure 38: B735 fuel optimal trajectories with different cross winds, RTA : 800 sec

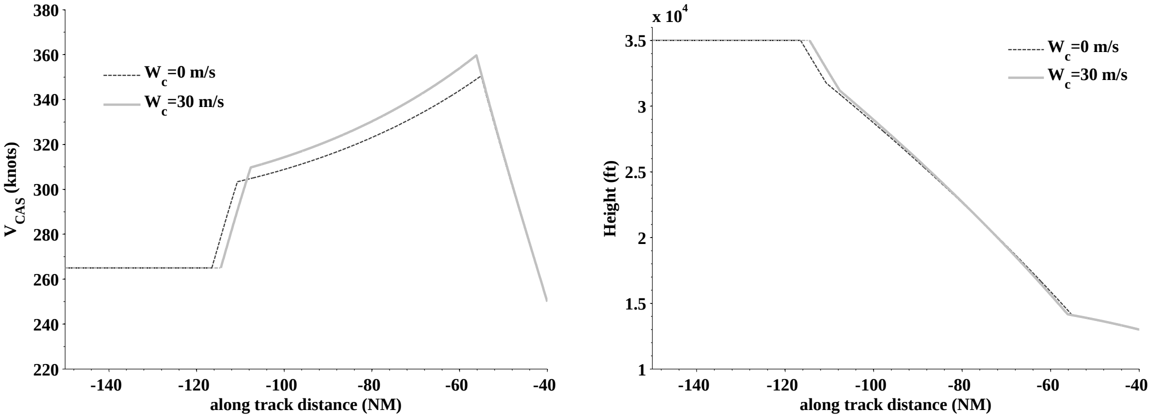

(a) Speed profiles (b) Altitude profiles

Figure 39: B764 fuel optimal trajectories with different cross winds, RTA : 800 sec

4.6.1.3 Wind Shear Effect

The effect of the wind shear term on the optimal trajectories is analyzed by a comparison of the performance bound with various wind profiles, which have the same cruise wind speed but different wind shear terms. The wind profiles for this analysis is shown in Fig. 40 (a) and the RTA curve as a function of c_t is shown in Fig. 40 (b). The influence of the wind shear term is relatively small compared to the horizontal and cross wind effect. For small c_t, the performances of the four wind profiles are almost the same. However, for large c_t, the RTA gap between the four cases becomes larger.

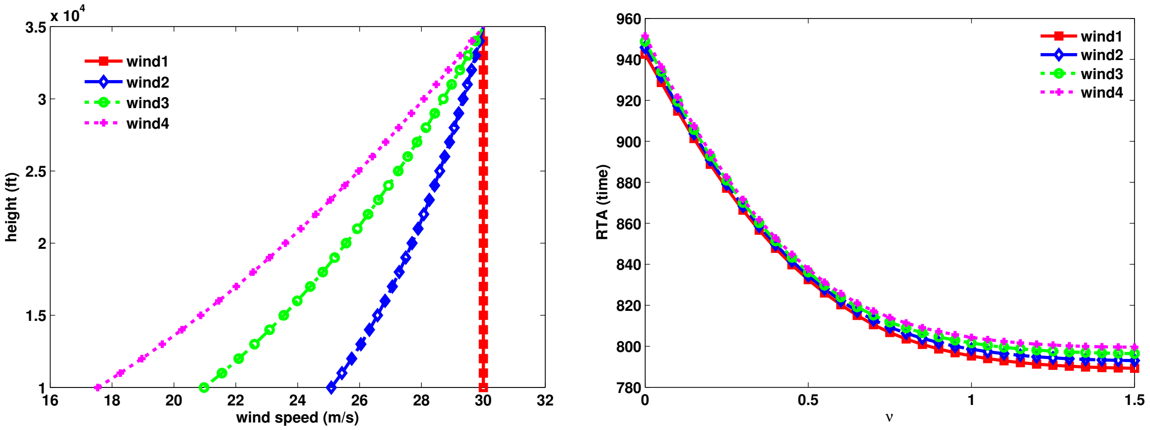

(a) Wind profiles

(b) Altitude profile

Figure 40: Performance bound results with various wind shear conditions

4.6.2 Emission optimal trajectory

In this section, minimum NO_x trajectories are analyzed with different RTAs and wind profiles. The RTA effect on the optimal trajectories for both the B735 and the B764 are shown in Fig. 41 and 42, respectively. Compared to the minimum fuel cases in Fig. 33 and 34, the optimal speed profiles for a large RTA case are quite different. However, as the RTA decreases, the minimum fuel and minimum NO_x trajectories become similar. At the end, the two different optimal trajectories converge to the minimum time trajectory as shown in Fig. 33, 34, 41, and 42.

The minimum NO_x CAS profiles for both the B735 and B764 for several constant horizontal wind components are shown in Fig. 43 and 44, respectively. In this numerical evaluation, the RTA for all cases is the same 950 sec. Similar to the minimum fuel case, the wind speed affects the structure of the optimal trajectory. The optimal structure of the B735 CAS profile in the head wind case is different from the others.

The comparison of the minimum NO_x trajectories with two different cross wind profiles are shown in Fig. 45. The cross wind components used in this analysis are the same as the wind for the minimum fuel case. The results are quite similar to the minimum fuel case. The cross wind term increases the speed on the singular arc and moves the TOD point toward the runway threshold.

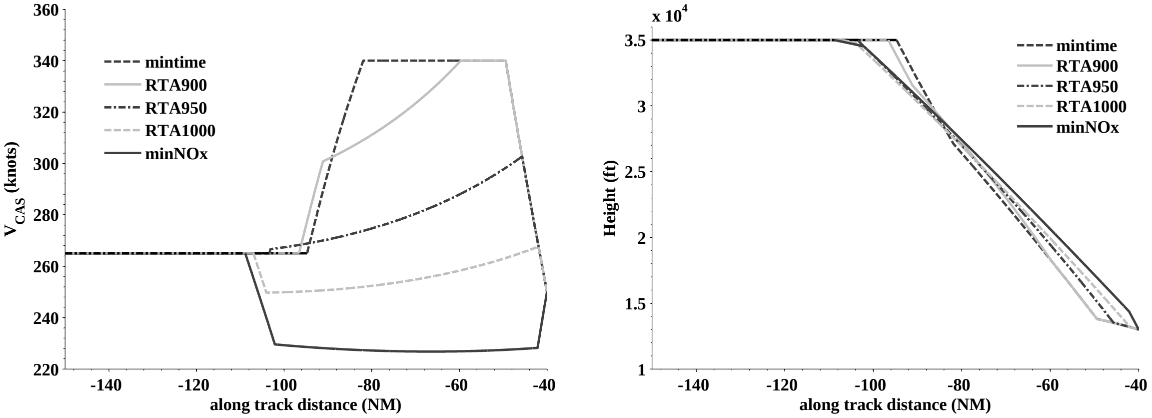

(a) Speed profiles

(b) Altitude profiles

Figure 41: B735 minimum NO_x trajectories with various RTA conditions. Wind is zero.

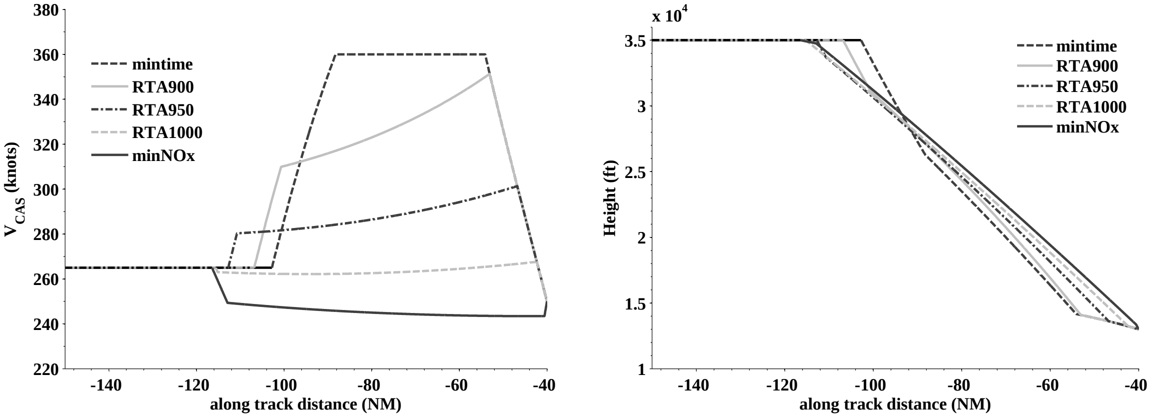

(a) Speed profiles

(b) Altitude profiles

Figure 42: B764 minimum NO_x trajectories with various RTA conditions. Wind is zero.

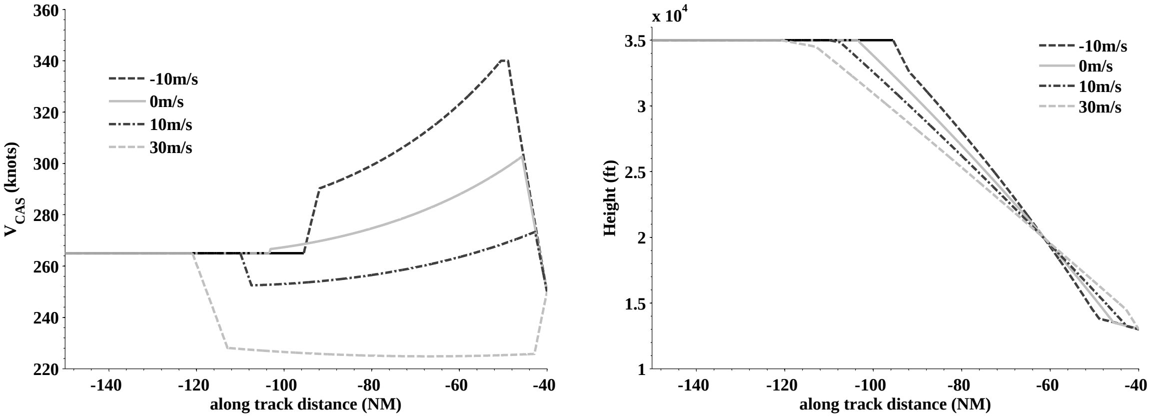

(a) Speed profiles (b) Altitude profiles

Figure 43: B735 minimum NO_x trajectories with various wind conditions. RTA is fixed as 950 sec.

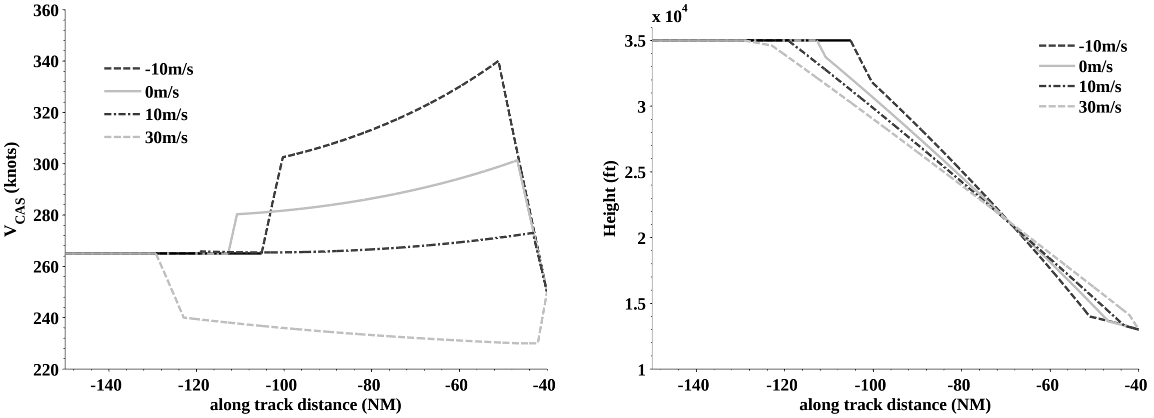

(a) Speed profiles (b) Altitude profiles

Figure 44: B764 minimum NO_x trajectories with various wind conditions. RTA is fixed as 950 sec.

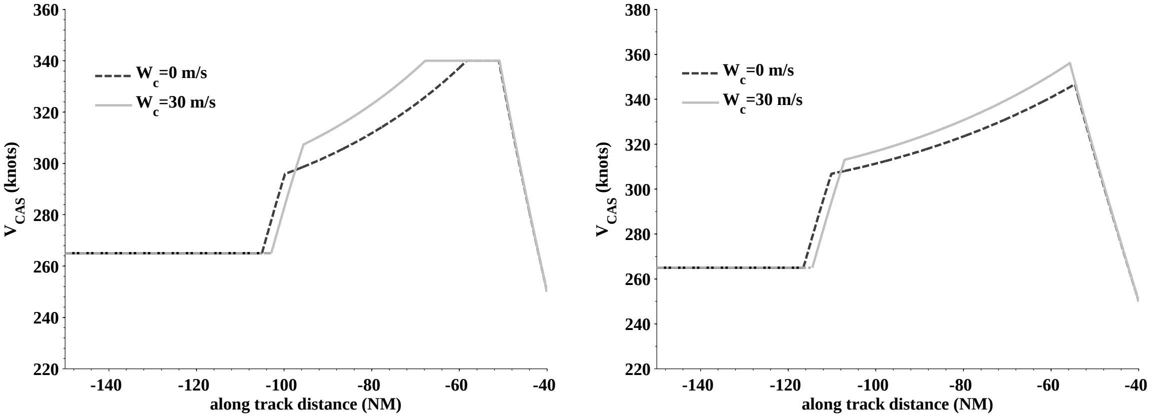

(a) B735 (b) B764

Figure 45: Minimum NO_x speed profiles with different cross winds, RTA : 800 sec

4.7 FMS Application

A sequential method to solve optimal control problems of hybrid systems was proposed to generate the optimal trajectory using the FMS VNAV modes. The proposed method uses the relaxed optimal solution, which is the lower bound of the original problem.

In this section, to reduce the computational time of the proposed method, we use the solution of Problem 4.1 instead of the relaxed optimal problem. To evaluate the computational time saving, we compare the computational time to solve to solve the relaxed optimal solutions of B735 in Fig. 25 in Chapter 3. For the numerical approach in Chapter 3, we used GPOPS ver.5 for optimal control problem solver. Since the minimum time trajectory can be generated by the combination of the current FMS VNAV modes, we used the minimum time trajectory as an initial trajectory in the numerical approach. In the semi-analytic approach proposed in this chapter, c_t was set to 0.5 as the initial value for the fixed RTA case. Since the switching structure of the minimum time trajectory is known, it can be obtained by one time calculation. In the minimum fuel case, c_t is zero, and hence it can be calculated immediately without any iteration.

The comparison result is shown in Table 18. The computational time was measured on an AMD Athlon II dual core M320, 2.1 GHz, 3.0 GB RAM HP laptop with MATLAB R2010b implementation. The computational times with the semi-analytic approach are less than 3.5 sec for all cases. In the minimum time and minimum fuel cases when the solutions are converged by one time calculation, the computational times are less than 1 sec. However, we need over 100 sec to solve the minimum fuel problems since the minimum fuel solutions contains singular sub arc which is difficult to solve numerically[4]. Therefore, if we replace the original relaxed solution with the semi-analytic solution, we can reduce the computational time significantly.

Table 18: Computational time comparison

Method	mintime	RTA1000	RTA1050	RTA1100	minfuel
numerical(GPOPS) [sec]	14.52	79.95	158.29	191.93	141.42
semi-analytic (sec 4.5)[sec]	0.90	2.18	3.09	3.13	0.55

The simplified algorithm is shown in Fig. 46. STEP 1 and STEP 2, which are the steps to solve the relaxed optimal control problem and to partition the trajectory using the relaxed optimal solution, can be replaced to the step to calculate the trajectory using the algorithm in section 4.5. Since all junction points are obtained, the trajectory partitioning is automatically performed through the algorithm A in section 4.5. Furthermore, by the analysis of the switching structure, the nonsingular arc is either min/max ROD or min/max FPA, the estimated mode for the nonsingular arc is determined during the trajectory calculation. The boundary arc is either min/max CAS/MACH also. Hence, the remaining partitioned trajectories belong to the interior singular arcs. Therefore, we reduce the iterations in mode estimation by doing this step for only singular arc.

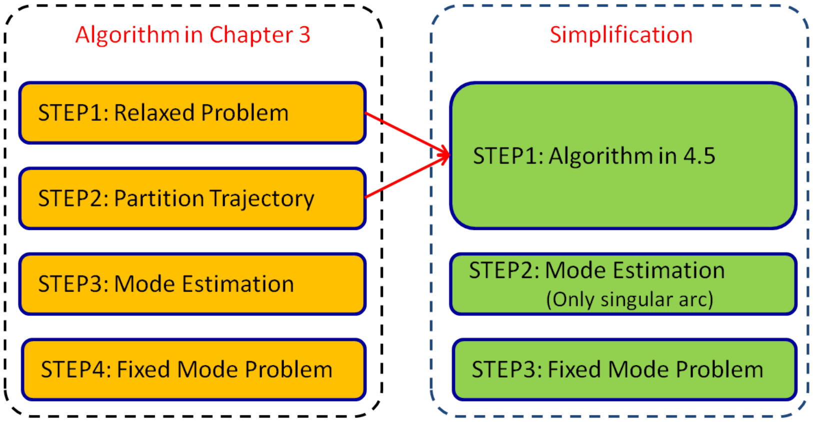

Figure 46: Simplified Algorithm

4.7.1 Comparison of Mode Estimation

With the same initial and final conditions in chapter 3, we investigated the optimal switching structure using the proposed algorithm in section 4.5. Table 19 compares the mode estimation results in chapter 3 and the results from the algorithm in section 4.5 with various wind and RTA conditions. As the same in chapter 3, the tail/head wind denotes the constant 20/-20 m/s horizontal wind profile. As shown the results, for all computed cases, the mode segments and the corresponding mode sequence from the different approaches are identical.

This result supports the simplified sequential method depicted in Fig. 46. The simplification in dynamics does not affect the optimal switching structure compared to the relaxed optimal control problem in chapter 3. Therefore, by generating the approximated solution using the method in this chapter, we can reduce the computational load and time significantly. Furthermore, this approximated solution provides the initial guess on the mode parameter with high quality.

Table 19: Comparison of mode estimation result

		Sequential method		algorithm in sec 4.5	
Type	wind	seg.	mode seq.	seg.	mode seq.
RTA1000	zero	5	$\{CP \quad CD \quad CD \quad CV \quad CD\}$	5	$\{CP \quad CD \quad CD \quad CV \quad CD\}$
RTA1050	zero	3	$\{CD \quad CD \quad CD\}$	3	$\{CD \quad CD \quad CD\}$
RTA1100	zero	3	$\{CD \quad CD \quad CD\}$	3	$\{CD \quad CD \quad CD\}$
RTA950	tail	3	$\{CD \quad CD \quad CD\}$	3	$\{CD \quad CD \quad CD\}$
RTA1000	tail	3	$\{CD \quad CD \quad CD\}$	3	$\{CD \quad CD \quad CD\}$
RTA1050	tail	3	$\{CD \quad CD \quad CD\}$	3	$\{CD \quad CD \quad CD\}$
RTA1100	head	4	$\{CP \quad CD \quad CV \quad CD\}$	4	$\{CP \quad CD \quad CV \quad CD\}$
RTA1150	head	3	$\{CD \quad CD \quad CD\}$	3	$\{CD \quad CD \quad CD\}$
RTA1200	head	3	$\{CD \quad CD \quad CD\}$	3	$\{CD \quad CD \quad CD\}$

4.8 Conclusion

We have presented a method to generate the optimal descent trajectory to minimize the environmental impact with a fixed-range and fixed Required Time of Arrival (RTA) in the presence of both horizontal and cross wind components. The fuel cost and NO_x cost has been used as environmental costs. Both the cross wind and the horizontal wind were assumed to be a function of altitude. Flight idle thrust was assumed during the entire descent phase. The flight range was specified from the point at the latter stages of the cruise segment to the meter fix. MACH and calibrated airspeed (CAS) bounds, rate of descent limit, and flight path angle limit have been taken into account for both flight envelope protection and passenger comfort.

The two-phase optimal control problem has been converted to an equivalent free initial and final time single phase optimal control problem with unknown cost index. The analytic formulation of the singular arc and the possible boundary arc condition have been analyzed using the necessary conditions of optimality. Based on this analysis, the structure of the optimal trajectory has been derived. The switching structure is affected by a specific aircraft type, an RTA, and wind condition.

In the proposed method, the optimal solution is computed by iterating to find the cost index c_t for satisfying an RTA condition. Since the optimal trajectory is generated by forward and backward integration, the proposed algorithm does not require the additional computational power compared to the current FMS vertical trajectory generation method using VNAV functions. Hence, this algorithm can be implemented in a current FMS system and can be applied to time based operations for the arrival phase.

CHAPTER V

PERFORMANCE BOUND ANALYSIS OF CDA TRAJECTORY

The methodology for the performance bound analysis for a time based CDA operation is described in this chapter. We propose an optimal control based methodology using the trajectory optimization method described in the previous chapters. We perform the trajectory performance bound analysis for an arrival to Hartsfield Jackson International airport (ATL) from the Northwest with ATL in an East flow operation (i.e. aircraft landing towards the East). Based on results of the analysis, we propose a single flight time strategy for conflict resolution during the entire CDA flight.

5.1 Introduction

5.1.1 Time Based CDA Operation

Trajectory Based Operation (TBO) is a key component of the Next Generation Air Transportation System (NextGen). One objective with TBO is to reduce the environmental impact while maximizing the capacity and enhancing the safety of the airspace. As mentioned in Chapter 1, a CDA procedure is a proven procedure for reducing the environmental impact. Therefore, the time based CDA operation concept, which is the operational concept which combines a CDA with TBO in the arrival phase, supports the stated objectives of NextGen.

The key concept of the time based CDA operation, from the ATC standpoint, is the Controlled/Scheduled Time of Arrival (CTA/STA). ATC assigns the STA to individual aircraft for the sequencing and scheduling at the meter fix to ensure separation management inside the TRACON airspace, thereby increasing the success rate of CDA procedures. A regulatory minimum separation is required at the runway threshold and managing the separation at or near this minimum is necessary to maximize the runway throughput. When ATC or the Traffic Management Advisor (TMA) assigns an RTA to the aircraft, the minimum required separation time should be one of the constraints.

For an individual aircraft, the assigned STA is interpreted as the Required Time of Arrival (RTA). To meet the RTA condition at the meter fix, four dimensional (4D) trajectory generation and 4D guidance functions should be implemented in the FMS.

5.1.2 Related Works and Motivation

Several researchers have studied the strategy of a time based CDA operation concept and proven the potential benefits through simulations and/or flight trials [15, 14, 24, 26, 34, 40, 42, 41]. However, far fewer researchers have focused on an RTA assignment while considering conflict resolution during the entire CDA flight has been accomplished.

In order to make appropriate sequencing and scheduling, which results in an RTA assignment for the aircraft at a meter fix, ATC needs the following information: 1) a minimum required time separation at meter fix between leading and trailing aircraft, and 2) a feasible RTA range of each aircraft. This is explained in Fig. 47 where a) is for information in 1), and b) is for information in 2).

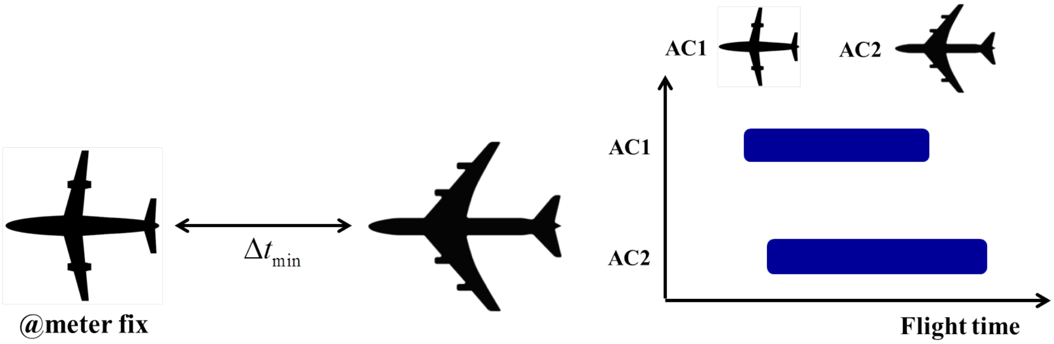

(a) minimum separation (b) feasible range

Figure 47: Information for RTA Assignment

Ren and Clarke [55] developed TASAT which was described earlier in this thesis. This tool provides a separation analysis result to determine the required separation in terms of distance or time between any aircraft pair at a selected meter fix/waypoint along the lateral path. Therefore, by using TASAT, we can obtain Δt_{min} information in Fig. 47 a). However, since TASAT assumes the user defined descent speed, e.g. (Mach/CAS) = (0.8/300), it cannot provides the feasible RTA range information in Fig. 47 b).

As stated, the issue in time based CDA operation is the conflict resolution during the descent with a given RTA. One of the tools to address this issue is the Efficient Descent Advisor (EDA)[15] from NASA. EDA is a ground automation tool for the speed and the path stretch advisory in order to meet an RTA at a meter fix without conflict. In a field test of the Oceanic Tailored Arrival (OTA) the performance of EDA was proven successfully[14]. However, EDA calculates the trajectory of a single aircraft without knowing the exact aircraft weight. If variance in the weight is larger than expected, a descent using the EDA advisory speed cannot meet a RTA constraint within an acceptable error range. In addition, the conflict can occur even though EDA only checks the conflict possibility for all aircraft approaching the same meter fix. Therefore, airborne RTA capability is necessary to reduce the RTA accuracy. This topic has been addressed in Chapter 3 and 4 of this thesis.

Because of the difference in speed and vertical profile, a loss of minimum spacing between in-trail aircraft can be possible, and simulation in [72] has shown the case. Therefore, conflict resolution during the descent still remains a problem though aircraft have the capability to generate a trajectory to meet a fixed RTA.

5.1.3 Goal

In this chapter, we address the issues of scheduling and spacing at the meter fix, and he goal is to answer the following questions:

1. What is the feasible schedule/RTAs of the arrival aircraft for the successful CDA procedure?
2. What is required to guarantee a conflict free CDA operation?
3. Does the feasible schedule guarantee a conflict free CDA procedure?

To address these questions, we describe in this chapter an optimal control based methodology to analyze the feasible time range of a CDA procedure. Based on the result of the feasible time range analysis, a single transit time flight strategy is proposed in order to apply CDA procedures in dense or heavy traffic conditions. A numerical simulation with a proposed operating strategy at ATL is conducted to evaluate the performance of the proposed concept in terms of the conflict resolution during the entire CDA.

The remainder of this chapter is organized as follows; In section 5.2, we introduce the TPA concept. In section 5.3, we show the analysis results for various aircraft types operating into ATL. In section 5.4, we propose a single transit time strategy and shows the numerical evaluation of this strategy. Our conclusions are presented in section 5.5.

5.2 Methodology for Analysis of Trajectory Performance

5.2.1 CDA Trajectory Performance

We define the term 'trajectory performance' for the en-route CDA trajectory under a time based CDA operation. Since the key component, in this thesis, is an RTA for the time based CDA operation, the trajectory performance is defined as the flight time from a fixed RTA waypoint to a meter fix. This definition will be applied in the remainder of this chapter.

The concept of a Trajectory Performance Analyzer (TPA) is used in this section to analyze the performance bound of the CDA trajectory for a selected aircraft type. The CDA trajectory performance varies depending on the performance index and a RTA condition as shown in Chapter 2 $\sim$ 4. Therefore, the trajectory performance is not determined as a single value, but a set $\mathcal{P}$. Any feasible flight time at a given condition belongs to this set (The condition will be explained in the next subsection).

Since the performance is the flight time from the RTA frozen waypoint to a meter fix, the smallest value point t_{min} in $\mathcal{P}$ is determined by the minimum time solution of the Problem 3.4. In the same way, the largest value point t_{max} in $\mathcal{P}$ is determined by the solution of the Problem 3.4 with $-J_t$, which is the maximum time case. Therefore, the set $\mathcal{P}$ is expressed as:

$$\mathcal{P} = \{t \in \mathbb{R} | t_{min} \leq t \leq t_{max}\}. \tag{121}$$

From the the airline's perspective, a flight that consumes more fuel with a longer arrival time does not have any benefit. Based on this fact, the trajectory performance should be modified by using the end points of the pareto frontier curve of the two performance indices: minimum time and minimum fuel. Figure 48 shows the time of arrival and fuel consumption curve. In the Figure, the curve between the minimum time point and the minimum fuel point is the pareto frontier from Lemma 4.1. Therefore, we modified the set $\mathcal{P}$ using the t_{fuel}, which is the time of the minimum fuel solution of Problem 3.4. The resulting modified performance set $\tilde{\mathbf{P}}$ is:

$$\tilde{\mathcal{P}} = \{t \in \mathbb{R} | t_{min} \leq t \leq t_{fuel}\}. \tag{122}$$

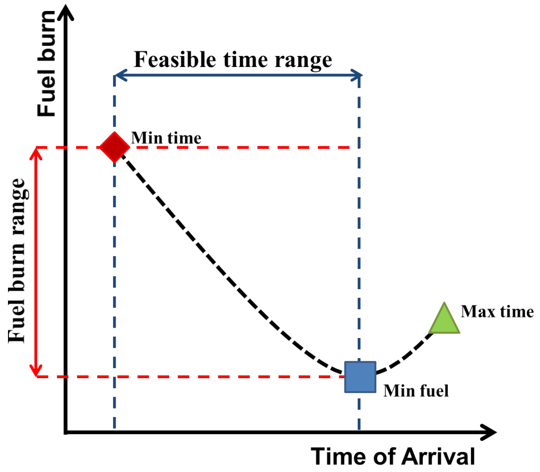

Figure 48: Trajectory Performance Limit

5.2.2 Trajectory Performance Analyzer

The optimal control based methodology used to analyze the CDA trajectory performance is detailed below. As stated in Eq. (122), the CDA trajectory performance bound is determined by different types of optimal solutions to Problem 3.4. Hence, calculation of the performance bound of a CDA trajectory requires solving the optimal control problems with different performance indices.

As shown in Chapters 3 and 4, the optimal solution varies according to the variations in wind, aircraft weight, and the initial condition of cruise speed and altitude. Information regarding cruise flight conditions can be transmitted to ATC via aircraft-ground communication links, while ATC does not know the aircraft weight. For this reason, a sensitivity analysis of the optimal solution is necessary. For the robust performance bound that covers all possible variations, the following intersection of all sets of particular conditions must be computed:

$$\tilde{\mathcal{P}}_f = \bigcap_{i=1}^{N} \tilde{\mathcal{P}}_i \tag{123}$$

where N is the number of the scenario for the sensitivity analysis.

The TPA is used to perform an analysis of the CDA trajectory performance. The overall concept of the TPA is shown in Figure 49. As shown in the Figure, the TPA consists of three parts; input generator, trajectory optimizer, and performance analyzer. Each column in Figure 49 represents a component of the TPA. The next subsection describes the detailed functions and input/output of each component.

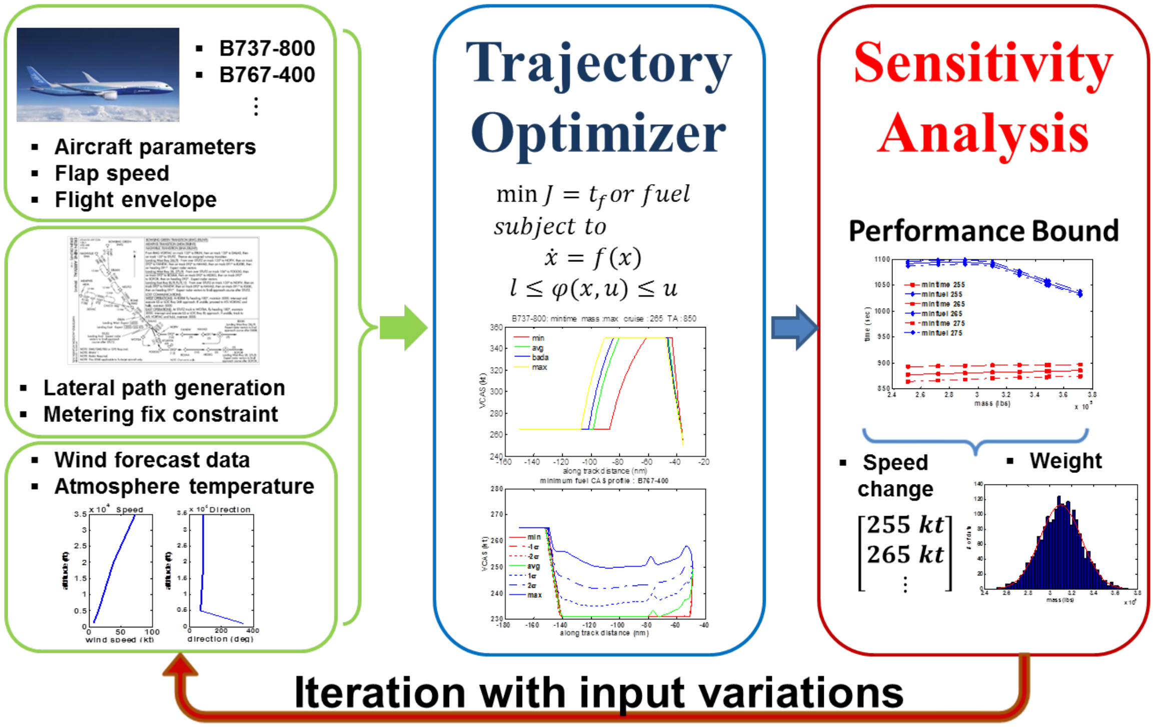

Figure 49: The Concept of TPA

5.2.2.1 *Input generator*

As stated above, the CDA trajectory varies with variations in aircraft weight, wind, and cruise conditions. In the TPA input generator, one scenario is for the CDA trajectory optimization. This scenario is categorized by three terms as shown in Figure 49. The first category generates aircraft performance data, and the second category generates geometrical related inputs. The third category generates the environmental input and constraints. The inputs and constraints can be changed by setting a different aircraft type, STAR charting, and current wind conditions.

- Aircraft performance data and constraints

  Any aircraft performance data can be used for the TPA. In this thesis, Base of Aircraft Data (BADA)[2] is used for the aircraft performance data. Aerodynamic parameters, thrust and fuel flow data are loaded depending on the aircraft type. The flap extension speed range is calculated relative to the aircraft type and weight. The maximum Mach/CAS is set for generating path constraints to protect the flight envelope.

- Geometric constraints

  In this category, guidance for the lateral path is generated using the FMS function according to the published STAR chart that is cleared for the arrival. The boundary condition at the meter fix is also generated. Typically, the STAR specifies the altitude at this point and in some cases both the altitude and speed. In the case that only altitude is given, 250 KCAS is used as the speed constraint at the meter fix.

- Environmental input and constraints

  In this category, forecasted wind data is generated. Wind is assumed to be a function of altitude. Atmospheric properties such as temperature, pressure, and air density are also generated according to the ISA model.

5.2.2.2 Trajectory Optimizer

A Trajectory Optimizer (TO) initializes multi-phase optimal control problems using the numerical data from the input generator. If the altitude constraint at a meter fix is higher than 10,000 ft, the optimal control problem can be formulated as explained in Chapter 3. Since the performance bound is determined by two optimal solutions, which are the minimum time and the minimum fuel solutions, the optimal control problem in Problem 3.4 with two performance indices are solved in the TO. In the TO, a pseudospectral method is chosen because it guarantees fast convergence and robustness to an initial guess[23], and it has been used in CDA trajectory optimization problems[49, 51] . GPOPS[53] and

SNOPT[25] are used as the pseudospectral method code and an NLP solver, respectively.

As shown in Chapter 2∼4, the minimum time trajectory is determined at the boundary at the path constraints, and it can be generated by the combination of the current FMS VNAV. Hence, using this fact, the minimum time trajectory can be solved with a given mode sequence and the limit of the parameter in each mode.

For the minimum fuel solution, the flight time of the relaxed minimum fuel solution is very close to that of the FMS optimal solution from the sequential method, therefore, we can use the relaxed optimal solution instead of the FMS optimal solution for a fast calculation.

5.2.2.3 Sensitivity Analysis

The CDA trajectory can have very large variations as the aircraft performance parameters change. Among the many parameters, weight variation can have a substantial influence and significantly affects the trajectory performance. While known and available, the airlines do not want to share their aircraft weights (competitive issue) to ATC or other advisory tools such as the EDA. Hence, the weight is a very critical uncertainty to be accounted for when considering the performance bound analysis of each aircraft.

It should be noted here that TASAT has historical aircraft weights for arrivals into ATL for a number of aircraft types, and it can be modeled as a Gaussian distribution as shown in Fig. 50 (due to the nondisclosure agreement, the label of x axis is omitted).

TASAT only has weight data for a limited number of aircraft. To handle this issue, the TPA generates weight distributions for the selected aircraft by using the Operating Empty Weight (OEW), the Maximum Take Off Weight (MTOW), and the maximum payload M_p which are more easily obtained.

The aircraft weight is expressed as

$$W_{des} = OEW + c_p M_p + c_f M_f, \tag{124}$$

where c_p is the payload ratio between actual payload and M_p, and M_f is the maximum fuel when M_p is assumed. $M_f = MTOW - (EOM + M_p)$. c_f is the fuel weight ratio between actual fuel weight and M_f.

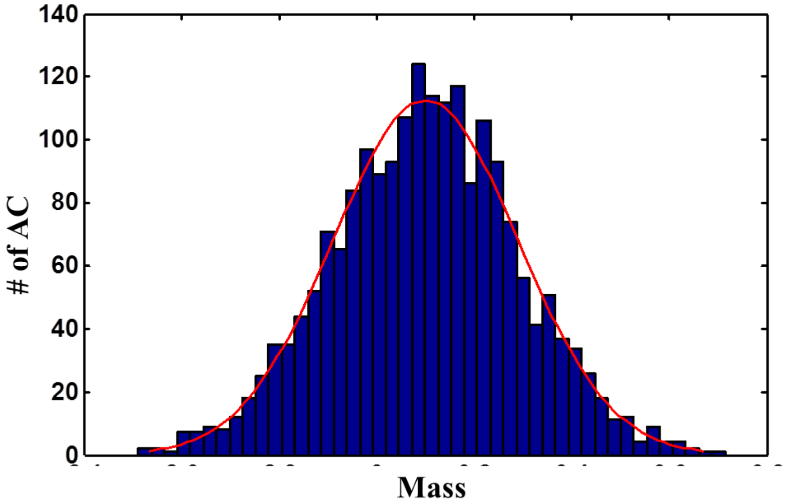

Figure 50: Descent Weight Distribution for B767-400

From the mass distribution for the available aircraft in TASAT, min/max c_p and c_f values can be obtained by matching the weight range. The estimated (c_p, c_f) for the maximum/minimum descent weight is $(1, 0.4)/(0.1/0.2)$. From these parameter sets, the maximum and minimum weight can be calculated. In addition, from the mass distribution in TASAT, the min/max value among the historical weight data is outside of $\pm 2\sigma$ boundary. From this fact, we assume that min/max value is $\pm 3\sigma$ value, and hence we can calculate mean and standard deviation of the weight for the selected aircraft.

From the generated weight distribution, the weight samples are chosen (the methodology to choose a sample set will be explained in the next subsection). By using the sampled weight set, several scenarios are generated and the sensitivity analysis is performed.

5.2.3 Scenario Generation

Obviously, limit points t_{fuel} and t_{min} of the performance set $\tilde{\mathcal{P}}$ are a function of the weight from the results in Chapter 2. Since weight is a random variable, the limit performance t_{fuel} and t_{min} are also random variables. However, the relationship between the weight and performance is not a linear function, so the distributions of t_{fuel} and t_{min} may not be Gaussian although the weight has a Gaussian distribution.

The most frequently used method to calculate a distribution for a nonlinear mapping in the presence of uncertainty is the Monte-Carlo simulation. Figures 51 and 52 show the simulation results and the histograms of t_{fuel} for the for B735 and B764, respectively. These results are obtained by a Monte-Carlo simulation with 200 samples from the weight distribution. As expected, the distributions of t_{fuel} and t_{min} are not Gaussian. Furthermore, the shape of the histogram in two cases are quite different. This difference is due to the lower bound of CAS. In B735, the speed profile is limited by the CAS lower bound. On the other hand, for the B764, very few cases are limited by the CAS lower bound.

There are several important observations from this Monte-Carlo simulation. the first is that the curve t_{fuel} versus weight is smooth. As shown in Figures 51 and 52, even though the shape of the curve is different, the performance curves in both aircraft are smooth.

The second observation is that 95 % of the results are within a 2σ range. The statistical data for both aircraft are shown in Table 20. Since t_{fuel} is the upper limit point, the only concern is the lower range of t_{fuel}, and hence $\underline{t}_{fuel}$, which has a $\bar{t}_{fuel} - 2\sigma_t$ value is considered. In both cases, shown in Fig. 51 and 52, t_{fuel} covers 95 % of the 200 simulation results. Based on this observation, we will use $\underline{t}_{fuel}$ as the lower bound of the t_{fuel}. Hence, the mean and variance information is needed to calculate $\underline{t}_{fuel}$.

Table 20: Statistics of Monte-Carlo simulation results

	minfuel		mintime	
ACtype	mean (sec)	σ	mean (sec)	σ
B735	1,065.3	7.4413	873.1	1.018
B764	1,044.3	14.435	868.63	0.583

5.2.3.1 Unscented Transformation

Several sampling based mean and variance estimation methods for reducing the iteration number have been developed. Unscented Transformation (UT) is one of the method for calculating the statistics of a random variable which is transformed by the nonlinear mapping[37]. In UT, sample points, which is called sigma points, are chosen deterministically to catch the statistical properties of the transformed random variable by Taylor series expansion of the nonlinear mapping[37].

The most popular application of UT is the state estimation of a dynamical system. It

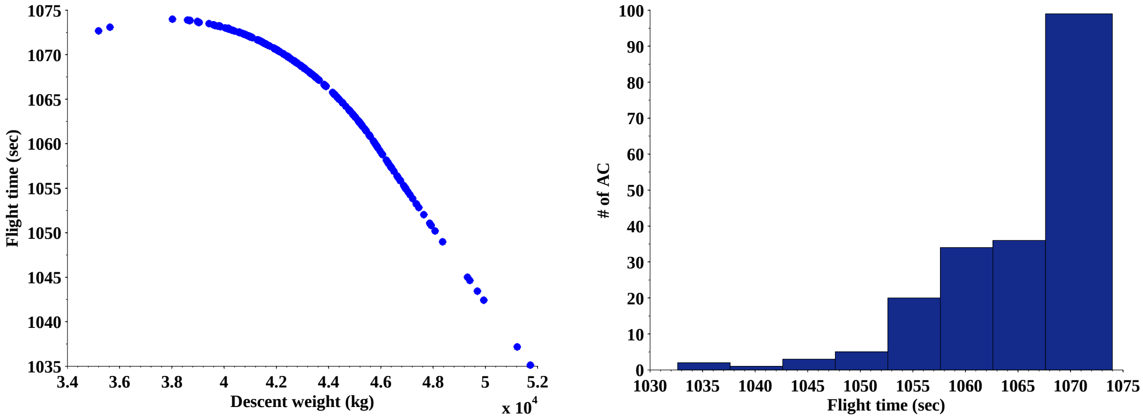

(a) Monte-Caro simulation (b) Histogram

Figure 51: Monte-Carlo simulation of the B735: minimum fuel case

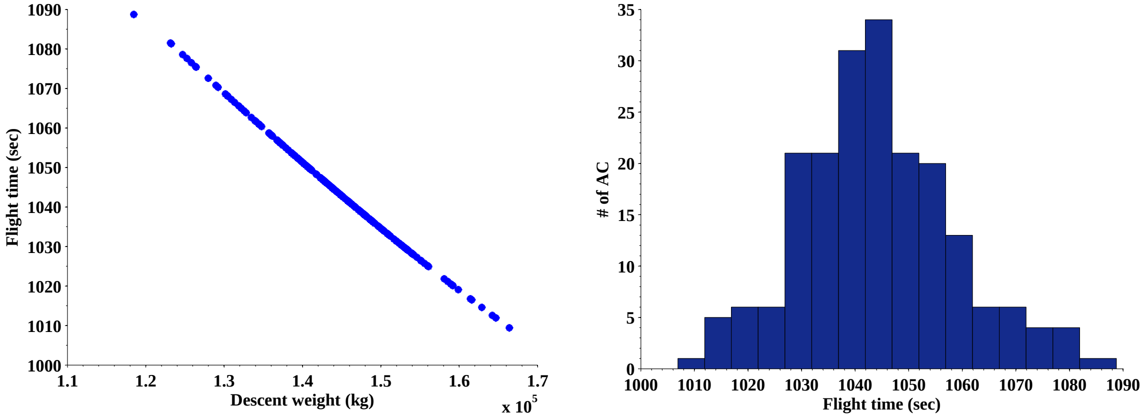

(a) Monte-Caro simulation (b) Histogram

Figure 52: Monte-Carlo simulation of the B764: minimum fuel case

has been adopted to the Kalman filter, which is called Unscented Kalman Filter (UKF), for the propagation of the mean and covariance along the nonlinear dynamics[36], and its performance has been proved in many nonlinear system applications including state estimation for six degrees of freedom aircraft dynamics[39].

Let $\bar{\mathbf{x}}$ and $\mathbf{P}_{xx}$ be a mean and covariance of a n-dimensional random variable. According to [37], the sigma points and associated weighting factors are selected as follows:

$$\begin{aligned}
\chi_0 &= \bar{\mathbf{x}} && , \mathbf{W}_0 = \kappa/(n+\kappa) \\
\chi_i &= \bar{\mathbf{x}} + \left(\sqrt{(n+\kappa)\mathbf{P}_{xx}}\right)_i && , \mathbf{W}_i = 1/2(n+\kappa) \\
\chi_{i+n} &= \bar{\mathbf{x}} - \left(\sqrt{(n+\kappa)\mathbf{P}_{xx}}\right)_i && , \mathbf{W}_{i+n} = 1/2(n+\kappa)
\end{aligned} \tag{125}$$

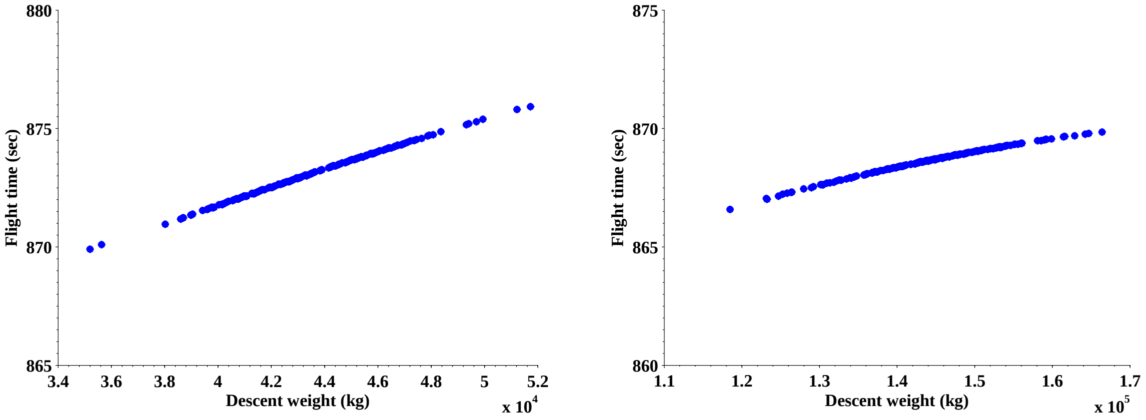

(a) B735 (b) B764

Figure 53: Monte-Carlo simulations of the minimum time cases for the B735 and B764

where $\kappa \in \mathbb{R}$, $\left(\sqrt{(n+\kappa)\mathbf{P}_{xx}}\right)_i$ is the i^{th} column of the matrix square root of $(n+\kappa)\mathbf{P}_{xx}$. $\mathbf{W}_i$ is the weight of the i^{th} sigma point. As shown in Eq. (125), $2n+1$ sigma points are needed for the statistical estimation of transformed n-dimensional random variable.

The following are the statistical estimation results of t_{fuel} by UT. This result shows that the error in the mean is less than 0.02 sec and the error in σ is less than 0.2. Based on this result, we will use UT for a sensitivity analysis and 2σ value for t_{fuel} and t_{min}.

Table 21: Statistics estimation from Unscented Transform)

	B737-500		B767-400	
	value	error($v_{MC} - v_{UT}$)	value	error($v_{MC} - v_{UT}$)
mean	1,065.4	-0.0637	1044.3	-0.0153
σ	7.5867	-0.1453	14.385	-0.0503

5.3 Case Study : Atlanta International Airport (ATL)

ATL is one of 22 airports in the US for which CDA procedures have been developed and operated. The CDA trajectory performance bound in ATL is analyzed using TPA. For a realistic result, the nominal wind profile in TASAT, which is obtained from historical wind data, is used for the analysis. The fleet used in the analysis is determined from ATL data for a 24 hour period. In the TPA, two performance indices, fuel cost and time cost are used for the trajectory optimization in the TO. Furthermore, an additional analysis is performed using the maximum time cost to evaluate the time range extension.

5.3.1 Test Environment

5.3.1.1 Path

All arrival traffic to ATL pass over one of four arrival/meter fixes; DIRTY, CANUK, HONIE, and ERLIN, and each is located at points on the boundary of the TRACON airspace which is a radius of approximately 40 NM from the airport. For ATL, there are four charted STARs, one each using these meter fixes. For this analysis, the ERLIN NINE RNAV STAR was selected. ERLIN NINE is used by inbound traffic from the Northwest quadrant.

The published chart for the ERLIN9 STAR is shown in Figure 54. In this analysis, the lateral path from the Memphis (MEM) transition is used. Since the CDA procedure starts at the initial waypoint which is in the cruise phase, it should be distant enough from the meter fix to track along the optimal trajectory obtained in the previous chapter, as described in Lemma 2.1 in Chapter 2, which provides one of the conditions for choosing the initial waypoint.

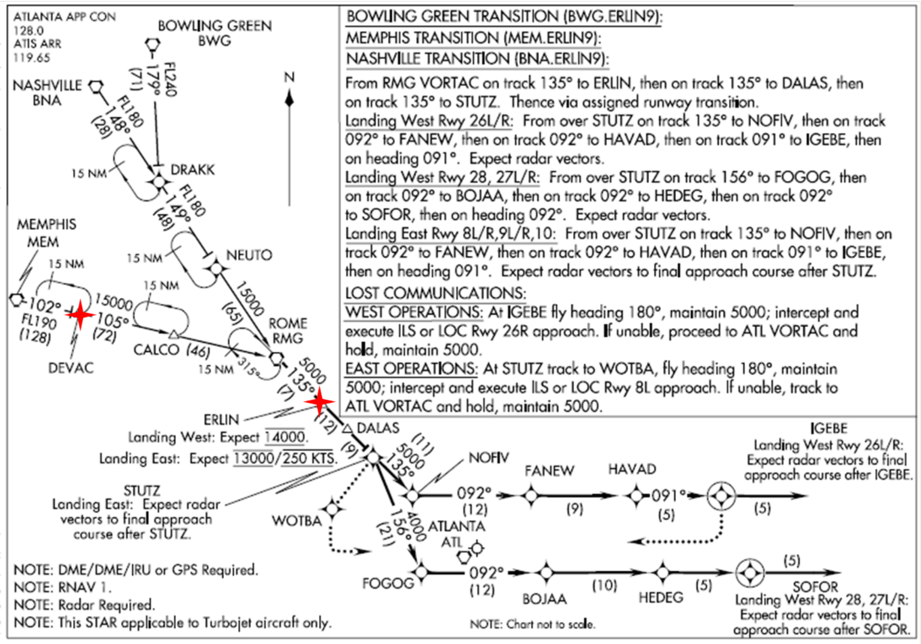

BOWLING GREEN TRANSITION (BWG.ERLIN9):
MEMPHIS TRANSITION (MEM.ERLIN9):
NASHVILLE TRANSITION (BNA.ERLIN9):
From RMG VORTAC on track 135° to ERLIN, then on track 135° to DALAS, then on track 135° to STUTZ. Thence via assigned runway transition.
Landing West Rwy 26L/R: From over STUTZ on track 135° to NOFIV, then on track 092° to FANEW, then on track 092° to HAVAD, then on track 091° to IGEBE, then on heading 091°. Expect radar vectors.
Landing West Rwy 28, 27L/R: From over STUTZ on track 156° to FOGOG, then on track 092° to BOJAA, then on track 092° to HEDEG, then on track 092° to SOFOR, then on heading 092°. Expect radar vectors.
Landing East Rwy 8L/R,9L/R,10: From over STUTZ on track 135° to NOFIV, then on track 092° to FANEW, then on track 092° to HAVAD, then on track 091° to IGEBE, then on heading 091°. Expect radar vectors to final approach course after STUTZ.
LOST COMMUNICATIONS:
WEST OPERATIONS: At IGEBE fly heading 180°, maintain 5000; intercept and execute ILS or LOC Rwy 26R approach. If unable, proceed to ATL VORTAC and hold, maintain 5000.
EAST OPERATIONS: At STUTZ track to WOTBA, fly heading 180°, maintain 5000; intercept and execute ILS or LOC Rwy 8L approach. If unable, track to ATL VORTAC and hold, maintain 5000.

NOTE: DME/DME/IRU or GPS Required.
NOTE: RNAV 1.
NOTE: Radar Required.
NOTE: This STAR applicable to Turbojet aircraft only.

Figure 54: KATL STAR chart of ERLIN9

ATC assigns an RTA at a meter fix, and once assigned it cannot be changed after aircraft pass the initial waypoint. Hence, the initial waypoint becomes the RTA freeze point, and the RTA at this fix is associated with the flight time to the meter fix.

The charted waypoint DEVAC in Fig. 54 was chosen as the initial waypoint or RTA freeze point since it is located on the boundary of ATL airspace and is the first encountered when transiting from MEM airspace.

The sequence of waypoints used for this analysis is DEVAC - CALCO - ROME(RMG) - ERLIN. with ROME coded navigationally as a fly-by waypoint. This coding is interpreted by the FMS LNAV as no requirement to pass directly over the RMG waypoint and allowing the FMS to anticipate a turn to intercept the required path from RMG to the next waypoint. For this arrival a landing on ATL runway 9R is planned. The lateral path and the along track distance is generated by the FMS logic contained in TASAT and the resulting distance from DEVAC to the runway threshold is approximately 170 NM. Since a landing on ATL 9R is planned, both charted speed and altitude constraints at ERLIN are given as shown in Fig. 54. The constraints at ERLIN are 250 kt CAS and an altitude of 13,000 ft.

5.3.1.2 Fleet

The target aircraft types were determined from historical flight data extracted from Enhanced Traffic Management System (ETMS) data (09. 30. 2005), the aircraft types arriving at ATL were chosen as a target fleet set. On this date, a total of 1,510 aircraft arrived in ATL.

BADA was used for the aircraft performance data to calculate the CDA trajectory performance in the TPA. Since not all of the aircraft types operating into ATL identified by the ETMS data are contained in BADA, the analysis was limited to only the aircraft types with available performance data.

As shown in Table 22, a total of 43 aircraft types were used with 23 classified as middle weight class and 20 as heavy weight class. It should be noted that BADA categorizes the aircraft weight into two classes, Middle and Heavy and differs from the FAA classification which is heavy, large, and small.

Table 22: Arrival Fleet in KATL

Weight	Aircraft type								
Middle	A319	A320	A321	B712	B722	B732	B733	B734	B735
	B736	B737	B738	B752	B753	CRJ1	CRJ2	CRJ9	E170
	E190	LJ35	LJ45	MD82	MD83				
Heavy	A306	A30B	A310	A332	A333	A343	A346	A388	B742
	B743	B744	B762	B763	B764	B772	B773	DC10	DC87
	L101	MD11							

5.3.1.3 Environmental Condition and Initial Condition

In this test, the atmosphere was assumed to be the ISA Standard. Historical wind data for ATL in TASAT was used for the test. The wind vector is assumed to be a function of altitude, and wind data is given as a lookup table. The speed and direction of the wind at a specific altitude is calculated by the interpolation of the lookup table. The wind direction and speed used in this test are shown in Figure 55. Note that the wind direction denotes the heading angle of the wind vector from the North. Therefore, the wind in Fig. 55 is a westerly wind.

Since the initial cruise condition affects flight time, from the observed historical data, the initial cruise speed was set at MACH 0.782 and the flight level in cruise is set to 35,000 ft.

5.3.2 Test Result

5.3.2.1 Feasible Time Range

The feasible time range analyzed by the TPA are shown in Figures 56 and 57, where the results are grouped according to the weight classification in BADA. The feasible time range can be calculated by two ways. The first way is by determining the feasible time range between minimum time and minimum fuel flight time, as depicted by the green bars in Fig 56 and 57. This set is the performance set $\tilde{\mathcal{P}}$. The second way is by calculating the feasible time range using the minimum time and the maximum time range, which is the set $\mathcal{P}$. The summation of two color bars in Figures denotes this set.

The extended time ranges for aircraft in the middle weight classification for the fleet mix used are shown in Figure 56 and are very small. This means that the 2σ range of the

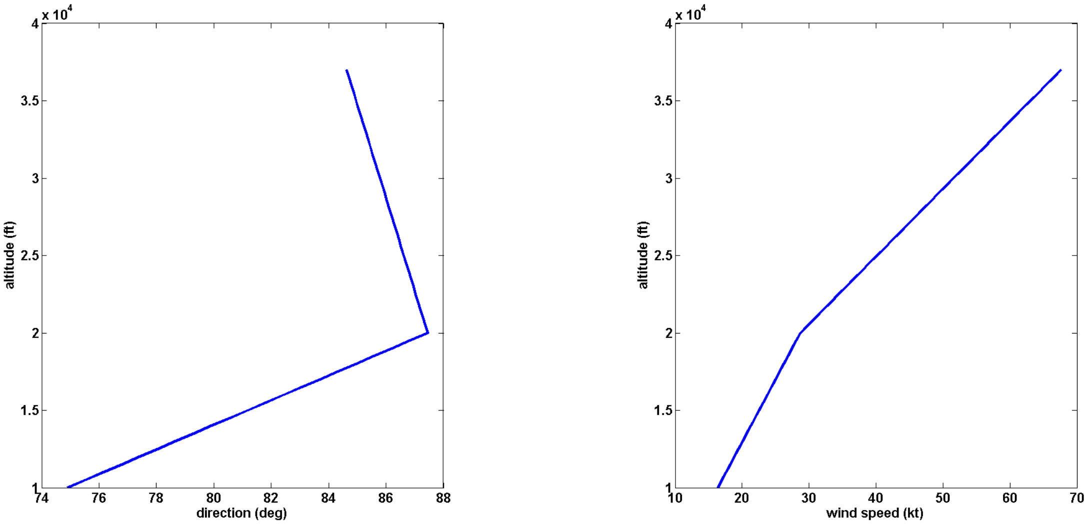

(a) wind direction (b) wind speed

Figure 55: Historical wind data used in ATL test

t_{fuel} is very close since the minimum fuel trajectory is determined at the lower bound of CAS. The LJ45 has the shortest time range and for the $\tilde{\mathcal{P}}$, the MD83 has the smallest t_{fuel} while the LJ45 has the smallest t_{max}.

The interesting observation is that there exists a common feasible time range for all aircraft in the middle weight classification. The common set $\tilde{\mathcal{P}}_c$ is determined by:

$$\tilde{\mathcal{P}}_c = \bigcap_{i \in Middle} \tilde{\mathcal{P}}_i.$$

The maximum time of all aircraft in the middle weight classification is limited by the LJ45. Since the minimum fuel and the maximum time trajectories are identical for the LJ45, and the t_{fuel} of the LJ45 is very close to the lowest value of t_{fuel}; using the maximum time performance there is no benefit in expanding the common feasible time set based on the LJ45 aircraft. However, the number of LJ45 landing operations is less than 10 flights for the 1,510 aircraft in Table 22. Therefore, the feasible time range of all middle class aircraft can be extended if we remove consideration of both the LJ35 and LJ45 aircraft. The variation in t_{min} according to the aircraft type is much smaller than the variation in t_{fuel}. With this action, the lower bound of $\tilde{\mathcal{P}}_c$ is determined by the E190 aircraft.

Table 23 shows the numerical values of the minimum time, the minimum fuel, and the maximum time limits of each aircraft. The limit is determined by 2σ values. The feasible time range of the middle weight classification is from 883.14 $\sim$ to 1,005.00 sec for $\tilde{\mathcal{P}}_c$. This result can be extended from 883.14 $\sim$ to 1,009.48 sec if we use the maximum time results as a performance bound. In the middle class case, the range extension is very small due to the LJ45. However, the feasible time range is extended to 1,026.10 sec if we remove LJ series aircraft due to it's very low percentage of landing traffic.

In the heavy weight classification, with the exception of the A333, the flight time range for each aircraft can be extended, and the level of extension is much larger than the aircraft in the middle weight classification. This is due to the fact that the minimum fuel trajectories are not restricted by the CAS lower bound as shown in the TASAT simulation results for the B764. For the A346, B764, B773, DC10, DC87, L101, and MD11, the feasible time range is extended by over 60 sec. Therefore, there exists a common feasible time range for all heavy weight classified aircraft also. The feasible time range of the heavy weight class is limited by the B743 for both $\mathcal{P}_c$ and $\tilde{\mathcal{P}}_c$.

Table 24 shows the performance limits of the heavy weight classification aircraft. In this class, the feasible time range is from 891.36 $\sim$ to 986.14 sec if the minimum fuel case is used as an upper bound. It can be extended to 1,009.08 sec by using the maximum time range. The common feasible time range for all aircraft in the heavy weight classification is from 891.36 $\sim$ to 986.14 sec, and this range can be extended from 891.36 $\sim$ to 1,009.08 sec if the maximum time case is used.

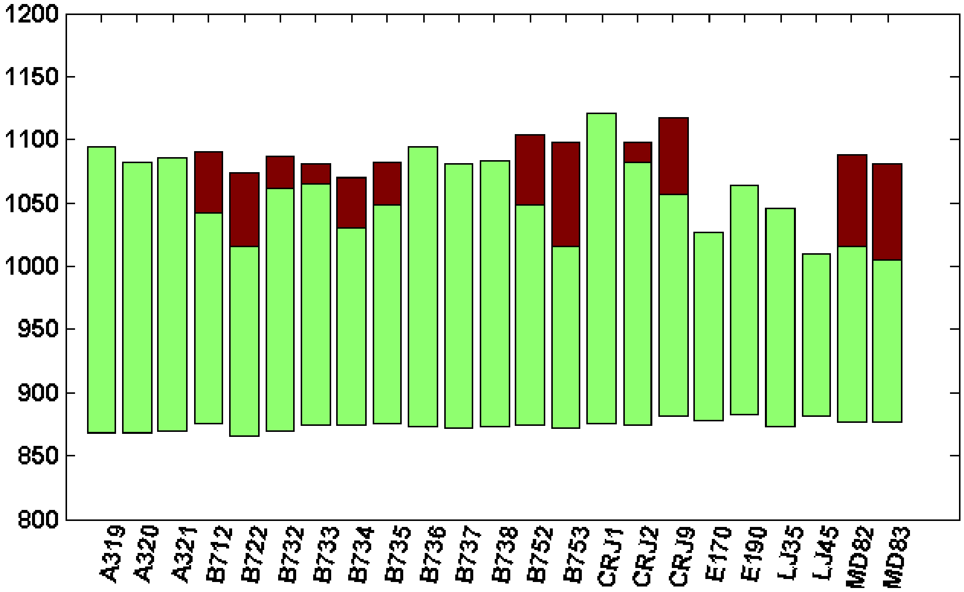

Figure 56: Feasible time range of middle class fleet

Table 23: Performance limit values: Middle class

ACtype	mintime	minfuel	maxtime
A319	867.81	1094.76	1094.76
A320	868.40	1081.62	1081.62
A321	868.99	1085.63	1085.50
B712	875.73	1041.88	1090.95
B722	865.28	1016.20	1073.60
B732	869.59	1062.04	1087.31
B733	874.45	1064.97	1081.18
B734	874.34	1030.63	1069.73
B735	875.30	1047.89	1082.52
B736	873.63	1094.51	1094.41
B737	872.46	1081.57	1081.57
B738	873.08	1083.33	1082.50
B752	873.75	1048.69	1103.98
B753	871.99	1015.62	1098.11
CRJ1	875.79	1121.19	1121.19
CRJ2	874.52	1081.80	1097.43
CRJ9	881.98	1056.60	1117.72
E170	877.63	1026.10	1026.10
E190	883.14	1064.62	1063.96
LJ35	873.20	1045.55	1044.72
LJ45	881.36	1009.48	1009.48
MD82	876.19	1015.47	1088.05
MD83	877.31	1005.00	1080.69
Time Range	883.14	1,005.00	1,009.48

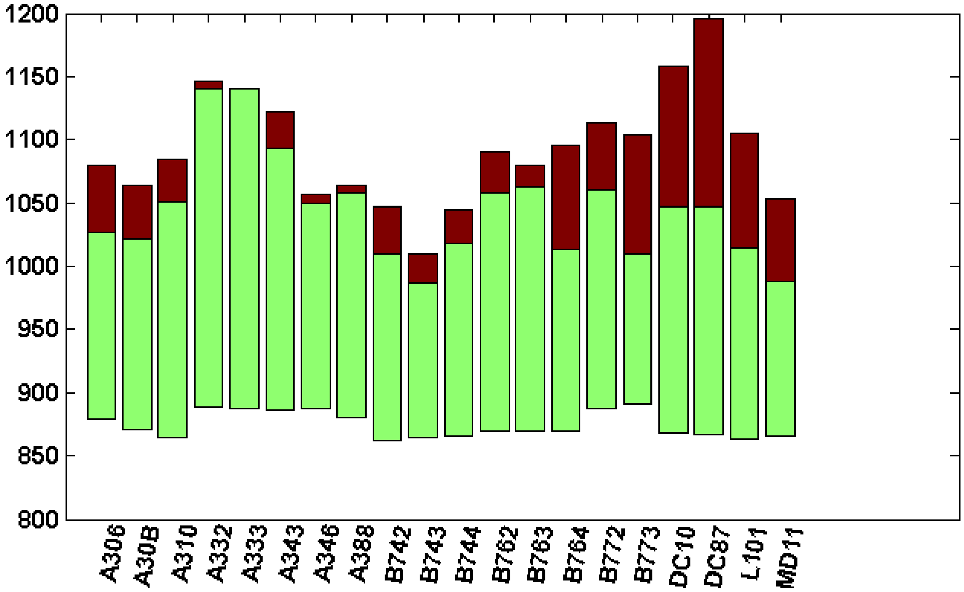

Figure 57: Feasible time range of heavy class fleet

Table 24: Performance limit values: Heavy class

ACtype	mintime	minfuel	maxtime
A306	879.39	1026.61	1079.45
A30B	871.07	1021.61	1063.63
A310	865.25	1050.20	1084.87
A332	889.15	1140.65	1145.76
A333	887.12	1140.54	1140.04
A343	886.47	1093.39	1121.82
A346	887.70	1049.66	1056.95
A388	880.76	1058.50	1064.26
B742	861.82	1009.60	1047.54
B743	864.63	986.14	1009.08
B744	865.28	1017.87	1044.27
B762	869.85	1058.31	1090.45
B763	870.01	1062.48	1079.39
B764	869.84	1013.77	1095.33
B772	887.52	1060.13	1114.18
B773	891.36	1009.30	1104.30
L101	862.96	1014.88	1104.94
DC10	867.94	1047.00	1158.22
DC87	867.37	1046.90	1195.70
MD11	866.33	987.73	1052.99
Time Range	891.36	986.14	1,009.08

5.3.2.2 TOD range

The TOD ranges of the aircraft listed in Table 22 are shown in Figures 58 and 59. The lower limit of the bar in the figures denotes the 2σ value of the TOD distribution for the minimum fuel solutions, and the upper limit of the bar is the 2σ value of TOD distribution for the minimum time solutions.

The TOD range analysis provides information for the marginal point to freeze the RTA at the meter fix. There is a possibility that an RTA will be infeasible after passing the lower bound of the TOD range. This occurs when the distance flown to meet the RTA is greater than the distance to the minfuel trajectory TOD for the aircraft.As an example, consider the B735 that has minfuel trajectories whose lower bound is -131.83 NM from the runway threshold and an RTA of 1047.89 sec. If the RTA changes after passing through a point -131.83 NM from the runway and the changed RTA is longer than the time to go when B735 flies along the minimum fuel trajectory, given RTA is infeasible because it passes minimum fuel TOD point already. On the other hand, before passing the lower bound of TOD point, all variations of CDA trajectory do not start descending, and hence aircraft can track all variations of CDA trajectory from the minimum time case to the minimum fuel case. Therefore, the RTA can be changed within feasible range at any time before passing the lower bound of TOD.

The lower bounds of TODs for all fleet listed in Table 22 except for DC87 are larger (closer) than -170 NM which is the along track distance of DEVAC. Therefore, DEVAC is the reasonable RTA freeze point in the sense of TOD analysis.

5.4 Time based CDA operation

Separation management between the leading and trailing pairs of aircraft is the one of the most significant issues when implementing CDAs, particularly in heavy traffic conditions. In this section, we discuss the time based CDA and its separation management strategy using the trajectory performance analysis from the TPA. First, we describe the necessary technologies to realize the time based CDA operation. Second, we explain the operational concept and discuss the conflict free condition during the CDA.

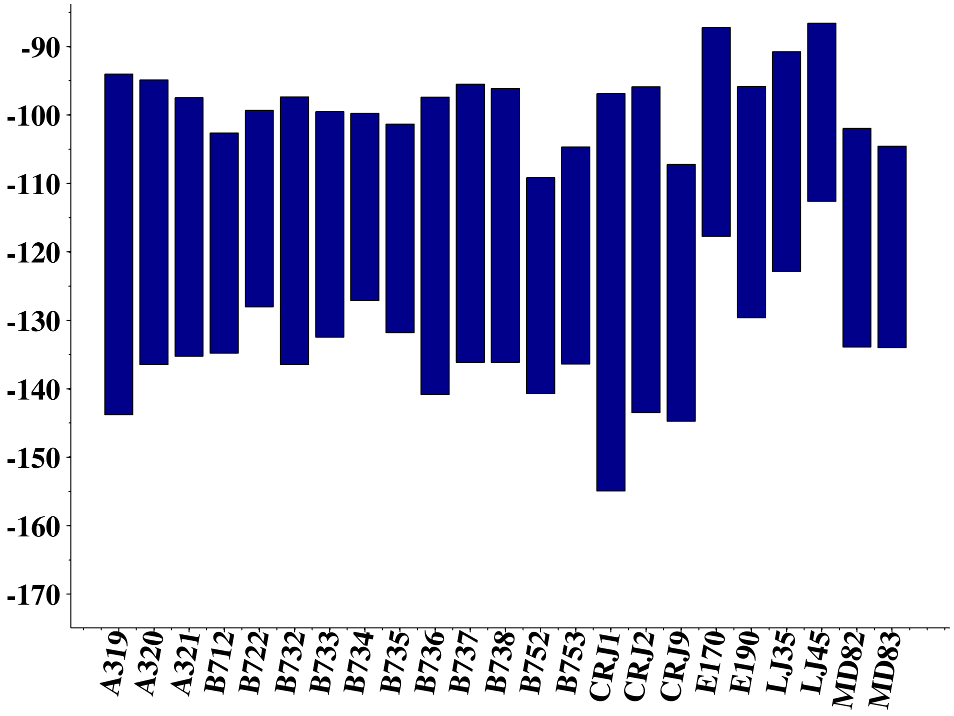

Figure 58: TOD range of middle class fleet

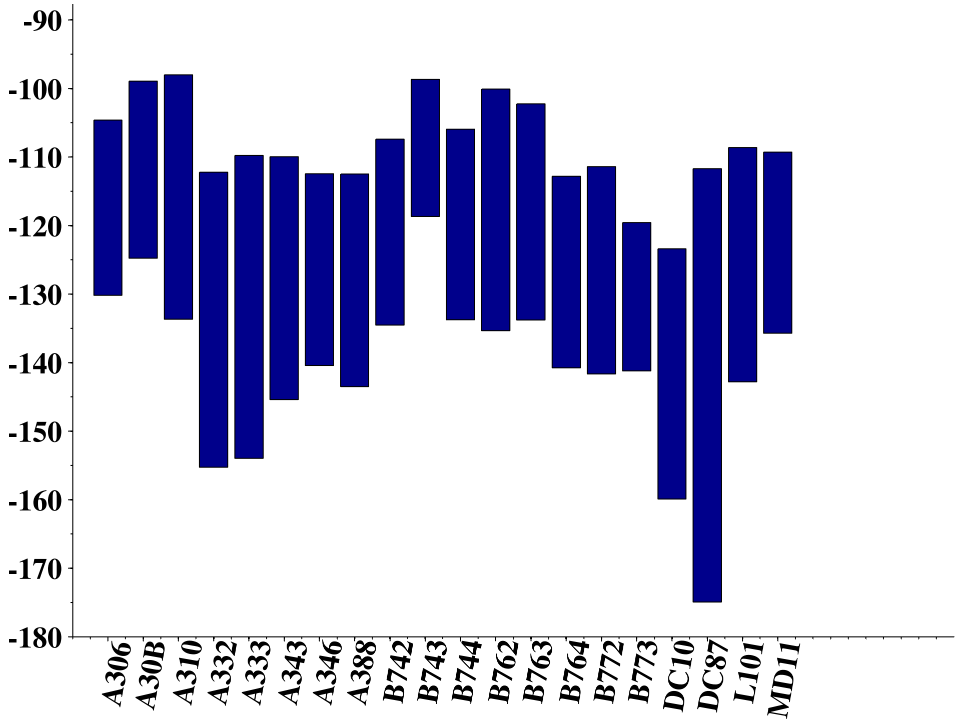

Figure 59: TOD range of heavy class fleet

5.4.1 Necessary Technologies

Before describing the time based CDA operation and the separation management strategy, we assume that the following three technologies are implemented in the FMS or in a ground automation tool for ATC:

1. 4D CDA trajectory generation

   The aircraft participating in CDA operation has a capability to generate a fixed RTA optimal CDA trajectory in the FMS, or the ground station has the same capability and can transmit 4D trajectory parameters to the aircraft via datalink. In the case that the ground station calculates the trajectory, the aircraft should provide their descent weight information.

2. Separation analysis at a meter fix

   The ground station has the capability to analyze the required minimum separation with selected leading and trailing aircraft pairs. TASAT[55] provides this information. Hence, it is assumed that TASAT is implemented in the ground automation tool, and ATC uses this information for the RTA assignment.

3. Feasible time range analysis

   The ground station uses the TPA for the feasible time range analysis. The fleet mix information in a specific time window is provided based on the prediction of the ETA at the RTA freeze waypoint, and the TPA uses this information to calculate the feasible time range of each aircraft. As shown in the ATL example in the previous section, it is assumed that there exists a common feasible time range for all aircraft types.

5.4.2 Concept of Operation

The concept of the time based CDA operation is depicted in Fig. 60 where WP1 is the RTA freeze waypoint. After this point, an RTA change is not allowed. The proposed operational concept consists of two parts; the CDA part and the cruise flight operation part.

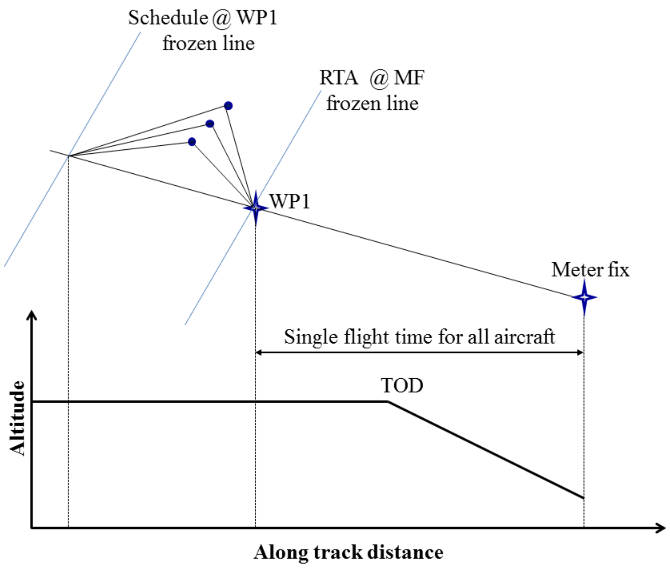

Figure 60: Single transit time CDA operation concept

The key strategy for the operation of a time based CDA part is the single flight requirement for all aircraft. As stated in the previous section, an RTA at the meter fix can be interpreted as the flight time from WP1 to the meter fix and vice versa. For a feasible operation, a single flight time should be determined within the common feasible time range obtained by the TPA. If all aircraft fly at the same flight time from WP1 to the meter fix, the separation time between a leading and trailing aircraft pair at WP1 will be maintained at the meter fix as shown in Fig. 61.

In the Figure, Δt denotes the separation time at WP1, and therefore the separation at the meter fix. Δ_{min} denotes the required minimum separation time at the meter fix for the successful CDA within the TRACON. As assumed in the previous section, the RTA is assigned considering Δt_{min}, and hence Δt should be greater than Δt_{min}. Since the separation time at the meter fix is the same as the separation time at WP1 by the single flight time strategy, Δ_{min} is a constraint to determine the scheduled time at WP1. If this condition holds, and the conflict does not occur during the descent, the CDA procedure from WP1 to the runway threshold guarantees a conflict free flight. In this manner, the target point to control the arrival time can be moved from the meter fix, which is a point along the the descent path, to WP1, which is a point along the cruise segment as shown in

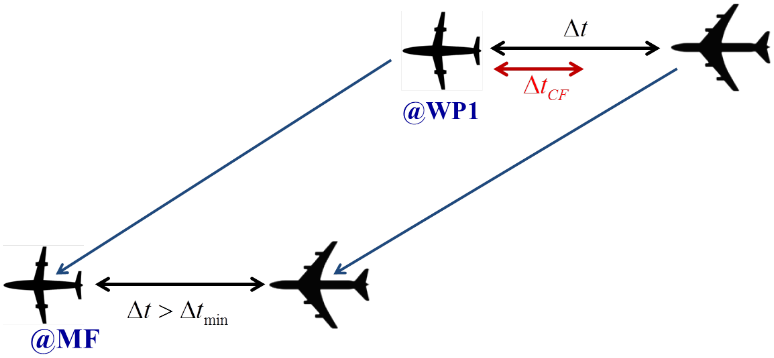

Figure 61: Separation analysis

Figure 60. Then, the traffic management problem becomes a 2D problem, which is much easier to manage and control than the original 3D problem.

In cruise, the scheduling at WP1 is necessary to manage the separation during the descent from WP1 to the meter fix. Scheduling at WP1 can be performed by modifying the existing scheduling algorithms at the meter fix [19, 45]. In the meter fix scheduling algorithm[45], a 5 NM minimum separation distance during the descent and the minimum runway threshold separation matrix are the constraints. In the modified scheduling algorithm for the proposed operation, the required minimum separation at the meter fix for a successful CDA is used instead of the runway separation matrix. This required minimum separation is analyzed by TASAT. To absorb the required delay from the scheduling algorithm, a cruise speed adjustment or path stretching similar to Three-Dimensional Path Arrival Management (3DPAM) concept[68] can be applied. The difference relative to the original 3DPAM is that the path stretch required for delay absorption occurs only in the cruise phase prior to WP1 as shown in Fig. 60.

For the successful time based CDA operation with a single flight time strategy, Δt_{min} at the meter fix, and an analysis of conflict from WP1 to the meter fix are needed. The following subsections describes these two issues.

5.4.3 Analysis of Required Minimum Separation

In order to determine Δt_{min}, TASAT[55] is used. Within TASAT, the CDA descent trajectory for simulation is generated by the embedded FMS VNAV function considering all waypoint constraints, if any. Multiple simulations of the CDA trajectory are produced by the Monte Carlo simulation to calculate the aircraft trajectory variations due to weight, wind and pilot response uncertainty. With the trajectory variations defined, a separation analysis is performed to determine the required minimum separation time at a meter fix for a leading and trailing aircraft pair. The trajectory variation set and the sequence of the aircraft at the meter fix become inputs to the separation analysis and the output is the required minimum separation distance or time at the meter fix.

5.4.4 Analysis of Conflict Free Condition

The condition $\Delta t > \Delta t_{min}$ implies a conflict free flight from the meter fix to the runway threshold. Therefore, the only remaining portion of the flight that can result in a loss of minimum separation is the flight segment from the WP1 to the meter fix. To analyze the conditions required for a conflict free operation we calculate the minimum separation time to guarantee no loss of separation from WP1 to the meter fix.

Similar to the sensitivity analysis in the TPA, the UT is used to calculate the Δt_{CF} in Fig. 61. Since Δt_{CF} is related to both leading and trailing aircraft, the dimension of the random vector is two, which is the weight of both leading and trailing aircraft. Hence, five sigma points are used to calculate $\Delta t_{CF}(i, j)$ where i is the leading aircraft type, and j is the trailing aircraft type.

Since Δt_{CF} is the required minimum separation time during the flight from WP1 to the meter fix, $\Delta t > \Delta t_{CF}$ implies the conflict free flight during the en-route CDA flight. Hence, the condition for a conflict free flight of the entire CDA flight from cruise to the runway threshold is as follows:

$$\Delta t_{CF} \leq \Delta t_{min} \leq \Delta t. \qquad (126)$$

5.4.5 Numerical evaluation

Since the required minimum separation at WP1 and the meter fix are same, the trajectories with a single flight time from WP1 to meter fix are conflict free if Eq. (126) holds. To evaluate the proposed single flight time strategy for the time based CDA operation, we calculated Δt_{CF} with a given traffic sequence. For a realistic result, ETMS data for one day was used to determine the sequence of aircraft and the aircraft type mix for arrivals into ATL.

According to the ETMS data, a total of 358 flights crossed the ERLIN waypoint, and the peak traffic period was $18 : 00 \sim 20 : 00$ hr when 47 flights crossed ERLIN. The 47 flights were used for the test traffic condition, and the sequence of the 47 flights was used to calculate Δt_{min} and Δt_{CF}. If an aircraft crossing ERLIN was not in the aircraft fleet type in Table 22, it was replaced by one in the table found to be the best match to the manufacturer and weight class. To compute Δt_{min} at ERLIN, TASAT was used. Since TASAT has only Boeing aircraft performance data, non-Boeing aircraft were replaced by Boeing aircraft matching the weight class.

The required minimum separation time matrix calculated by TASAT is shown in Table 25. The results are grouped by four different weight class of aircraft: Heavy, B757, Large, and Small. The longest required minimum separation time is 150.107 sec, and the shortest is 58.286 sec.

Table 25: Required minimum separation time matrix from TASAT

	Leading aircraft			
	Heavy	B757	Large	Small
Heavy	104.642	116.306	69.442	69.442
B757	123.268	106.981	58.286	58.286
Large	127.162	115.343	68.968	68.968
Small	150.107	138.480	103.489	68.968

Since the common feasible time range of the fleet in Table 22 is from $891.36 \sim$ to 986.14 sec, three flight time cases, 900 sec, 950 sec, and 980 sec, were simulated to check the condition in Eq. (126) during the flight from WP1 to the meter fix. The trajectories with a given RTA were generated by the sequential method in Chapter 3, and the minimum required separations were calculated using the tested sequence.

The results are shown in Fig. 62. The red bar denotes the required minimum separation time provided by TASAT, and the blue bars denoteΔt_{CF} for the given RTAs of 900, 950, and 990 sec, respectively. Since all three blue bars are below the TASAT result, the conflict free condition in Eq. (126) holds for all three RTAs if the schedule at WP1 does not violate

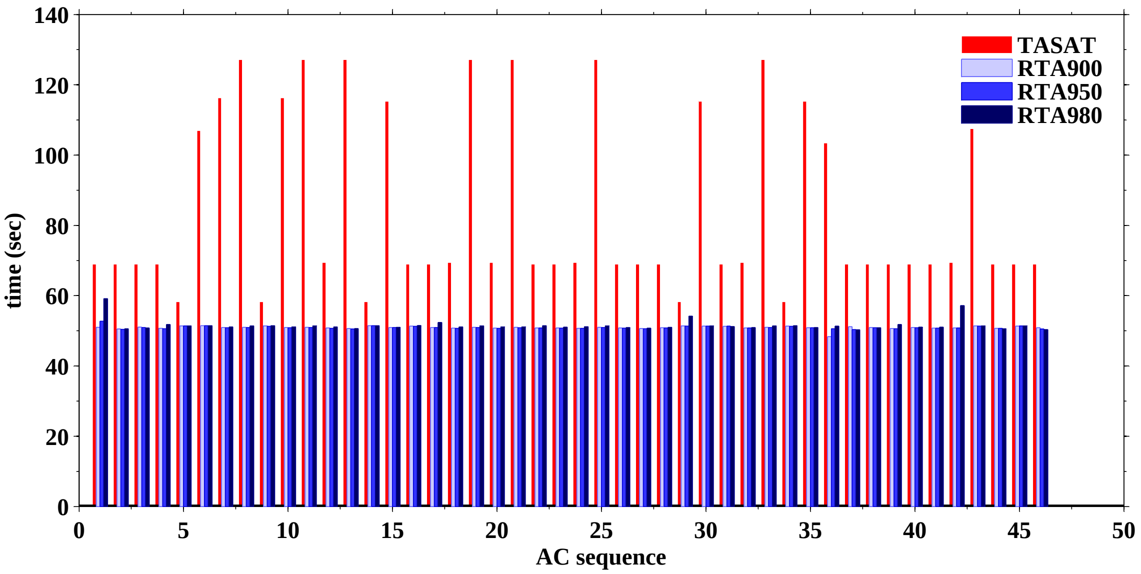

Figure 62: Required minimum separation with various RTAs

the separation matrix in Table 25.

The sequence of aircraft and their Δt_{min} and Δt_{CF} with three different RTA conditions are shown in Table 26. The interesting observation is that the required separation time for conflict resolution Δt_{CF} has approximately 50 to $\sim$ 51 sec for almost all simulated leading and trailing aircraft pairs for all three RTAs. The worst case occurs when a leading and trailing aircraft pair is (B737,MD82) with a 980 RTA. The required Δt_{CF} in this case is 59.175 sec. In both RTA 900 and 950 cases, all Δt_{CF} are less than 55 sec, the only two exceptions occurs in the RTA 900 case. The fuel optimal trajectories of five different aircraft are shown in Figure 63 for the same three RTA conditions. The TOD of each aircraft is quite different even though the RTA of each aircraft is the same. For any combination of these five aircraft, Δt_{CF} is 48 $\sim$ to 52 sec except the (CRJ1,B763) case, in which the Δt_{CF} is 55.69 sec. From these results, we can conclude that the required minimum separation time under a single flight time strategy is not sensitive to aircraft type.

Table 26: Required minimum separation time matrix from TASAT

ACtype	Class	Δt_{min}	Δt_{CF}:900	Δt_{CF}:950	Δt_{CF}:980
B737	L	N/A	N/A	N/A	N/A
MD82	L	68.968	51.010	52.714	59.175
B737	L	68.968	50.515	50.406	50.579
CRJ1	L	68.968	51.034	50.911	50.802
B738	L	68.968	50.708	50.573	51.831
B752	757	58.286	51.421	51.392	51.386
B752	757	106.981	51.457	51.431	51.471
B763	H	116.306	50.919	50.887	51.110
MD82	L	127.162	51.016	50.936	51.427
B752	757	58.286	51.390	51.284	51.455
B763	H	116.306	50.919	50.887	51.110
MD82	L	127.162	51.016	50.936	51.427
B763	H	69.442	50.837	50.721	51.083
CRJ2	L	127.162	50.645	50.557	50.621
B752	757	58.286	51.461	51.472	51.468
CRJ1	L	115.343	50.911	50.938	50.973
CRJ9	L	68.968	51.315	51.293	51.535
MD82	L	68.968	50.946	50.942	52.409
B763	H	69.442	50.782	50.721	51.083
MD82	L	127.162	51.022	50.936	51.427
B763	H	69.442	50.782	50.721	51.083
B712	L	127.162	50.988	50.901	51.085
MD82	L	68.968	50.835	50.821	51.470
B712	L	68.968	50.841	50.784	51.060
B763	H	69.442	50.729	50.724	51.154
MD82	L	127.162	51.022	50.936	51.427
CRJ1	L	68.968	50.799	50.759	50.945
A319	L	68.968	50.632	50.588	50.773
CRJ1	L	68.968	50.875	50.828	50.970
B752	757	58.286	51.384	51.366	54.195
CRJ9	L	115.343	51.354	51.371	51.419
CRJ9	L	68.968	51.309	51.331	51.226
B763	H	69.442	50.839	50.846	50.943
MD82	L	127.162	51.022	50.936	51.427
B752	757	58.286	51.333	51.284	51.455
B732	L	115.343	50.883	50.906	50.944
LJ45	S	103.489	48.341	50.586	51.350
B738	L	68.968	51.157	50.371	50.322
CRJ1	L	68.968	50.912	50.860	50.860
B738	L	68.968	50.623	50.573	51.831
B712	L	68.968	50.947	50.902	51.079
CRJ1	L	68.968	50.759	50.762	51.034
B763	H	69.442	50.835	50.816	57.203
CRJ9	L	127.162	51.391	51.322	51.414
B733	L	68.968	50.709	50.730	50.596
CRJ9	L	68.968	51.358	51.381	51.418
B737	L	68.968	50.881	50.537	50.362

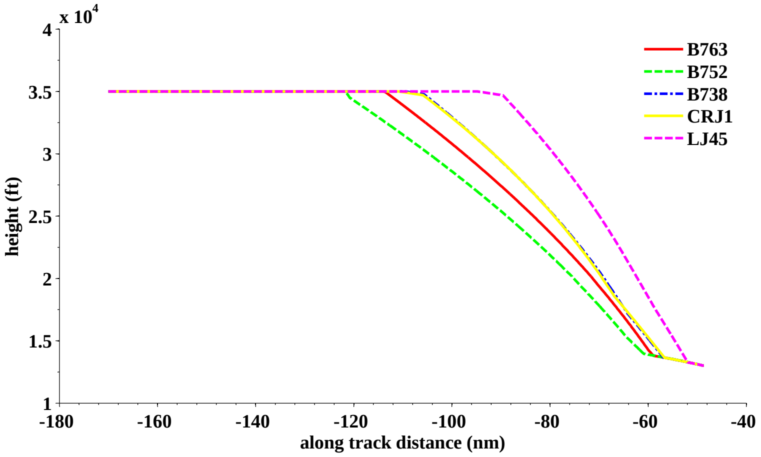

(a) RTA900

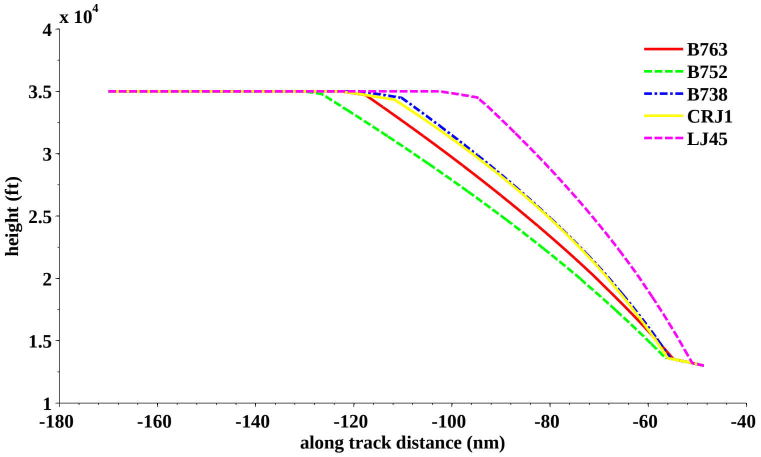

(b) RTA950

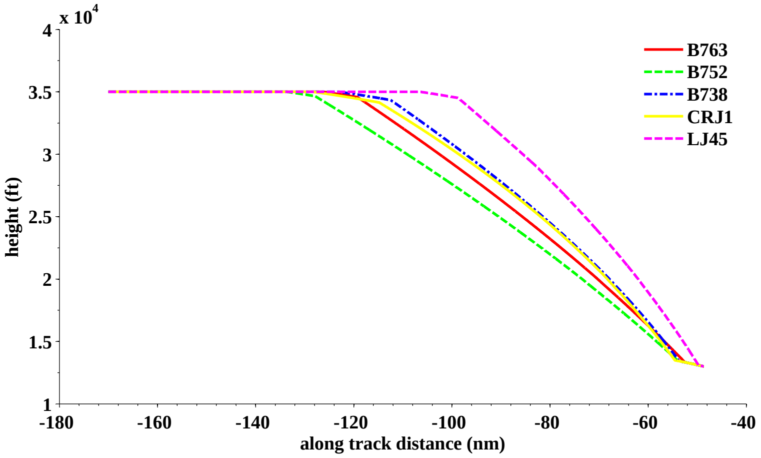

(c) RTA980

Figure 63: Trajectories with different RTAs

5.5 Conclusion

The performance bound of a CDA trajectory was analyzed for ATL arrivals using the ERLIN9 STAR. The target fleet was determined for one day of ETMS data, and the historical wind data in TASAT was used for the analysis. BADA data was used for aircraft performance data. With the given test condition, all middle weight class aircraft can fly from DEVAC to ERLIN with a time range of 883.14 $\sim$ 1,005.00 sec, and the common feasible time range of the heavy weight class aircraft is 891.36 $\sim$ to 986.14 sec if the minimum fuel case was used as the performance bound trajectory.

The time based CDA operational concept using the TPA analysis results appears to be a feasible way of increasing the CDA success rate in the heavy traffic conditions. The proposed concept uses a single flight time strategy from the RTA freeze waypoint to the meter fix for all aircraft. The single flight time was determined to be within the common feasible time range obtained from the TPA. The conflict resolution condition is analyzed under the assumption that the required minimum separation obtained from TASAT maintains at the RTA freeze waypoint. The numerical evaluation with ATL operating in a East traffic flow stream showed that the single flight time strategy provided the conflict free flights if the separation constraints at the RTA freeze waypoint are not violated.

CHAPTER VI

CONCLUSIONS

An optimal control based trajectory generation method and analysis methodology to support the trajectory based or time based Continuous Descent Arrival (CDA) procedures have been presented in this thesis. The contributions of this thesis are summarized in section 6.1, and directions of the future research are discussed in section 6.2.

6.1 Contributions

The major issue preventing the implementation of CDA procedures in high traffic conditions is separation management during the idle thrust/power descent. To increase the runway throughput without violating separation during CDA procedure, 1) aircraft should generate 4D trajectory, and 2) air traffic controller should know the performance bound of CDA trajectory and manage the separation of in-trail aircraft efficiently. This thesis has addressed these two problems. The specific contributions of this thesis are as follows:

- **Optimal control problem formulation for CDA trajectory generation**

  To maximize the benefits of CDA procedure such as flight time and fuel savings, the CDA trajectory optimization problem has been formulated as a multi-phase optimal control problem considering the flight envelope bound, passenger comfort, regulations from the FAA, and the flap and gear extensions. From the proposed optimal control problem formulation, the practical optimal solutions along with several performance indices have been obtained.

- **Hybrid system approach for the onboard CDA trajectory generation**

  Trajectory prediction performance on the ground station is one of the key component to manage the separation between aircraft. The trajectory prediction algorithms assume that the trajectory is generated as a combination of several Vertical Navigation

(VNAV) modes in the Flight Management System (FMS). By synchronizing the trajectory structure with ground, thereby reducing the trajectory prediction error, the vertical trajectory generation problem has been formulated as a hybrid/switched dynamical system. Four VNAV modes which are constant Calibrated airspeed (CAS), constant rate of descent (ROD), constant flight path angle (FPA), and constant Mach has been used for the problem formulation. Such a hybrid system has a different formulation from other hybrid systems since it has a mode parameter. The hybrid system with mode parameters has been formulated as a combination of the common dynamics for all modes and mode specific constraint.

- **Sequential algorithm to solve optimal control problem of hybrid systems**

  Based on the proposed formulation of the hybrid systems with mode parameter, sequential method to solve the optimal control problem of such a system has been developed. By relaxing mode specific constraint, the lower bound solution of the original problem has been solved. From the analysis of the switching structure and the curvature analysis, the number of mode transition has been estimated. By using the mode estimation technique for hybrid systems, mode sequence has been estimated. Finally, the fixed mode sequence problem has been solved. This algorithm has been applied to the trajectory generation problem within FMS framework, and its performance has been proved by numerical examples.

- **Fast calculation algorithm for en route CDA trajectory optimization**

  Using simplified dynamics, the relaxed optimal solution for the en route CDA trajectory optimization problem has been solved. The singular arc has been derived analytically, and the algorithm to find the optimal switching structure including boundary arc has been developed. By using the result from the analysis, the mode sequence can be estimated very fast.

- **Optimal control based methodology for analysis of CDA performance**

  An optimal control based methodology for analyzing the performance bound of the en route CDA trajectory has been developed. This methodology provides the feasible time range of each aircraft. The numerical case study for Atlanta International Airport (KATL) has showed that the common feasible time range that all aircraft can attend CDA procedure exists in ATL.

- **Conflict free CDA operation using single flight time strategy**
  Based on the performance bound analysis, time based CDA operation with single flight time strategy has been proposed. The conflict free flight condition has been analyzed, and numerical evaluation showed that the entire CDA operation from the RTA frozen waypoint to the runway can be achieved by appropriately chosen single flight time, which is the selected time in the common feasible time range. Hence, the arrival traffic management problem can be two-dimensional traffic management problem instead of three-dimensional problem by moving an metering point at which arrival time should be scheduled far away at the point in the cruise segment from the runway threshold.

6.2 Future Research

To achieve the time based CDA operation, the possible extensions of the research presented in this thesis are as follows:

4D Trajectory Guidance Law. In this thesis, we focused on the trajectory generation problem with fixed RTA condition. This is the flight planning component. To realize the time based CDA operation, a feedback guidance law to achieve the RTA is needed. In chapter 4, we analyzed the optimal switching structure and derived the analytic formulation of the optimal singular arc. Since the singular arc is the function of aircraft state, the natural property of the singular control is a feedback control. The optimal trajectory with singular arc presented in chapter 4 provides switching control between the open loop bang control and the singular arc feedback control. Hence, by applying this research, the 4D trajectory guidance law can be derived.

Trajectory Replanning Strategy. In some cases, for example when wind information is not accurate, replanning the descent trajectory may be more beneficial in terms of fuel and operating cost than trying to track the preplanned trajectory. Since CDA trajectory is generated assuming idle thrust, if severe uncertain disturbances exists, aircraft must use either addition thrust or speedbrakes to track the preplanned trajectory and meet the RTA constraint. Therefore, it is useful to employ a trajectory replanning strategy to determine whether the new trajectory is more beneficial or not. The possible variations of the optimal trajectory described in chapter 4 may provide the starting point of this research, as the algorithm in chapter 4 can generate the new trajectory very quickly.

Scheduling Algorithm. The one issue that must be addressed by scheduling algorithms for arrival management is the conflict resolution during the descent. The time based CDA operation concept with single flight time strategy has showed the benefit on the conflict resolution during the entire CDA flight from the cruise to the runway. For the efficient and safe traffic management, the scheduling algorithm with guaranteeing the conflict free flight during the descent is necessary. This would be achieved by adding the proposed single flight time strategy in the scheduling algorithm. To maximize the performance, the single flight time should be also included as a parameter to optimized.

REFERENCES

[1] "Icao engine exhaust emissions databank." `http://easa.europa.eu/environment/edb/aircraft-engine-emissions.php`.

[2] *User manual for the base of aircraft data (BADA). Revision 3.6.* EUROCONTROL Experimental Centre, 2004.

[3] Bengea, S. C. and DeCarlo, R. A., "Optimal control of switching systems," *Automatica*, vol. 41, no. 1, 2005.

[4] Betts, J. T., "Survey of numerical methods for trajectory optimization," *Journal of Guidance, Control, and Dynamics*, vol. 21, no. 2, pp. 193–207, 1998.

[5] Bryson, A. E., Denham, W. F., and Dreyfus, S. E., "Optimal programming problems with inequality constraints," *AIAA journal*, vol. 1, no. 11, pp. 2544–2550, 1963.

[6] Bryson, A. E. and Ho, Y.-C., *Applied optimal control: optimization, estimation, and control.* Taylor & Francis Group, 1975.

[7] Burrows, J. W., "Fuel optimal trajectory computation," *Journal of Aircraft*, vol. 19, no. 4, pp. 324–329, 1982.

[8] Burrows, J. W., "Fuel-optimal aircraft trajectories with fixed arrival times," *Journal of Guidance, Control, and Dynamics*, vol. 6, no. 1, 1983.

[9] Chakravarty, A., "Four-dimensional fuel-optimal guidance in the presence of winds," *Journal of Guidance, Control, and Dynamics*, vol. 8, no. 1, pp. 16–22, 1985.

[10] Clarke, J-P., B. J. R. L.-N. G. M. E. B. G. A. J. C. T. and Zondervan, D., "Flight trials of cda with time-based metering at atlanta international airport," in *AGIFORS Airline Operations*, 2007.

[11] Clarke, J.-P., "Systems analysis of noise abatement procedures enabled by advanced flight guidance technology," *Journal of aircraft*, vol. 37, no. 2, pp. 266–273, 2000.

[12] Clarke, J.-P., Brooks, J., Nagle, G., Scacchioli, A., White, W., and Liu, S. R., "Optimized profile descent arrivals at los angeles international airport," *Journal of Aircraft*, pp. 1–10, 2013.

[13] Clarke, J.-P., Ho, N. T., Ren, L., Brown, J. A., Elmer, K. R., Zou, K., Hunting, C., McGregor, D. L., Shivashankara, B. N., Tong, K.-O., Warren, A. W., and Wat, J. K., "Continuous descent approach: Design and flight test for louisville international airport," *Journal of Aircraft*, vol. 41, no. 5, pp. 1054–1066, 2004.

[14] Coppenbarger, R. A., Mead, R. W., and Sweet, D. N., "Field evaluation of the tailored arrivals concept for datalink-enabled continuous descent approach," *Journal of Aircraft*, vol. 46, no. 4, pp. 1200–1209, 2009.

[15] Coppenbarger, R., Lanier, R., Sweet, D., and Dorsky, S., "Design and development of the en route descent advisor (eda) for conflict-free arrival metering," in *Proceedings of the AIAA Guidance, Navigation, and Control Conference*, pp. 16–19, 2004.

[16] DuBois, D. and Paynter, G. C., ""fuel flow method2" for estimating aircraft emissions," *SAE Techinncal Paper 2006-01-1987*, 2006.

[17] Egerstedt, M., W. Y. and Axelsson, H., "Transition-time optimization for switched-mode dynamical systems," *IEEE Transactions on Automatic Control*, vol. 51, no. 1, 2006.

[18] Erzberger, H. and Lee, H., "Constrained optimum trajectories with specified range," *Journal of Guidance, Control, and Dynamics*, vol. 3, no. 1, pp. 78–85, 1980.

[19] Eun, Y., Hwang, I., and Bang, H., "Optimal arrival flight sequencing and scheduling using discrete airborne delays," *Intelligent Transportation Systems, IEEE Transactions on*, vol. 11, no. 2, pp. 359–373, 2010.

[20] Fahroo, F. and Ross, I. M., "Direct trajectory optimization by a chebyshev pseudospectral method," *Journal of Guidance, Control, and Dynamics*, vol. 25, no. 1, pp. 160–166, 2002.

[21] Franco, A., Rivas, D., and Valenzuela, A., "Minimum-fuel cruise at constant altitude with fixed arrival time," *Journal of Guidance, Control, and Dynamics*, vol. 33, no. 1, pp. 280–285, 2010.

[22] Franco, A., R. D. and Valenzuela, A., "Optimization of unpowered descents of commercial aircraft in altitude-dependent winds," *Journal of Aircraft*, vol. 49, no. 5, 2012.

[23] Garg, D., Patterson, M., Hager, W. W., Rao, A. V., Benson, D. A., and Huntington, G. T., "A unified framework for the numerical solution of optimal control problems using pseudospectral methods," *Automatica*, vol. 46, no. 11, 2010.

[24] Garrido-López, D., D'Alto, L., and Ledesma, R. G., "A novel four-dimensional guidance for continuous descent approaches," in *Digital Avionics Systems Conference, 2009. DASC'09. IEEE/AIAA 28th*, IEEE, 2009.

[25] Gill, P. E., Murray, W., and Saunders, M. A., "Snopt: An sqp algorithm for large-scale constrained optimization," *SIAM journal on optimization*, vol. 12, no. 4, pp. 979–1006, 2002.

[26] Gomez, R., M. M. and Prins, J. D., "Towards time-based continuous descent operations with mixed 4d fms equipage," in *AIAA Aviation Technology, Integration, and Operations Conference*, 2011.

[27] Gonzalez, H., V. R. K. M. S.-S. S. B. R. and Tomlin, C., "A numerical method for the optimal control of switched systems," in *49th IEEE Conference on Decision and Control (CDC)*, 2010.

[28] Hartl, R. F., S. S. P. and Vickson, R. G., "A survey of the maximum principles for optimal control problems with state constraints," *SIAM review*, vol. 37, no. 2, 1995.

[29] Hedlund, S. and Rantzer, A., "Optimal control of hybrid systems," in *38th IEEE Conference on Decision and Control*, pp. 3972–3977, 1999.

[30] Hedlund, S. and Rantzer, A., "Convex dynamic programming for hybrid systems," *IEEE Transactions on Automatic Control*, vol. 47, no. 9, 2002.

[31] Ho, N. T. and Clarke, J.-P., "Methodology for optimizing parameters of noise-abatement approach procedures," *Journal of Aircraft*, vol. 44, no. 4, pp. 1168–1176, 2007.

[32] Huntington, G. T., *Advancement and Analysis of Gauss Pseudospectral Transcription for Optimal Control Problems.* Sc.D. Dissertation, Massachusetts Institute of Technology, Department of Aeronautics and Astronautics, 2007.

[33] Hwang, I., Balakrishnan, H., and Tomlin, C., "State estimation for hybrid systems: applications to aircraft tracking," *IEE Proceedings Control Theory and Applications*, vol. 153, no. 5, 2006.

[34] Jackson, M., "CDA with RTA in a mixed environment," in *Digital Avionics Systems Conference, 2009. DASC'09. IEEE/AIAA 28th*, IEEE, 2009.

[35] Jacobson, D. H., Lele, M., and Speyer, J. L., "New necessary conditions of optimality for control problems with state-variable inequality constraints," *Journal of mathematical analysis and applications*, vol. 35, no. 2, pp. 255–284, 1971.

[36] Julier, S. J., "The scaled unscented transformation," in *American Control Conference, 2002. Proceedings of the 2002*, vol. 6, pp. 4555–4559, IEEE, 2002.

[37] Julier, S. J. and Uhlmann, J. K., "Reduced sigma point filters for the propagation of means and covariances through nonlinear transformations," in *American Control Conference, 2002. Proceedings of the 2002*, vol. 2, pp. 887–892, IEEE, 2002.

[38] Kamgarpour, M. and Tomlin, C., "On optimal control of non-autonomous switched systems with a fixed mode sequence," *Automatica*, vol. 48, no. 6, pp. 1177–1181, 2012.

[39] Kim, H. S., Park, S. K., Kim, Y., and Park, C. G., "Hybrid fault detection and isolation method for uav inertial sensor redundancy management system," in *Proceedings of the 16th IFAC World Congress, Prague, Czech Republic*, pp. 3–8, 2005.

[40] Klooster, J., Wichman, K., and Bleeker, O., "4d trajectory and time-of-arrival control to enable continuous descent arrivals," in *AIAA Guidance, Navigation and Control Conference and Exhibit*, 2008.

[41] Klooster, J. K. and de Smedt, D., "Controlled time of arrival spacing analysis," in *Proceedings of the Ninth USA/Europe Air Traffic Management Research and Development Seminar (ATM2011), Berlin, Germany*, 2011.

[42] Klooster, J. K., Del Amo, A., and Manzi, P., "Controlled time-of-arrival flight trials," in *8th USA/Europe Air Traffic Management R&D Seminar, Napa, CA*, 2009.

[43] Margellos, K. and Lygeros, J., "Toward 4-d trajectory management in air traffic control: A study based on monte carlo simulation and reachability analysis," *Control Systems Technology, IEEE Transactions on*, vol. 21, no. 5, pp. 1820–1833, 2013.

[44] Maurer, H., "On optimal control problems with bounded state variables and control appearing linearly," *SIAM journal on control and optimization*, vol. 15, no. 3, pp. 345–362, 1977.

[45] McClain, E., *Metroplex Identification, Evaluation, and Optimization.* Ph.D. Dissertation, Georgia Institute of Technology, School of Aerospace engineering, 2013.

[46] Nguyen, N., "Singular arc time-optimal climb trajectory of aircraft in a two-dimensional wind field," in *AIAA Guidance, Navigation, and Control Conference*, 2006.

[47] Norris, D., "Nonlinear programming applied to state-constrained optimization problems," *Journal of mathematical analysis and applications*, vol. 43, no. 1, pp. 261–272, 1973.

[48] Park, S. G. and Clarke, J.-P., "Fixed RTA fuel optimal profile descent based on analysis of trajectory performance bound," in *31st Digital Avionics Systems Conference (DASC),*, 2012.

[49] Park, S. G. and Clarke, J.-P., "Vertical trajectory optimization for continuous descent arrival procedure," in *AIAA Guidance, Navigation, and Control Conference*, 2012.

[50] Park, S. G. and Clarke, J.-P. B., "Feasible time analysis of wide fleet for continuous descent arrival," in *AIAA Aviation Technology, Integration, and Operations (ATIO) Conference*, 2013. AIAA 2013-4229.

[51] Park, S. G. and Clarke, J.-P. B., "Trajectory generation for optimized profile descent using hybrid optimal control," in *AIAA Guidance, Navigation, and Control Conference*, 2013.

[52] Pellegrini, E., S. S. D. K. J.-D. R. and Lohmann, B., "Nonlinear control of a semi-active suspension system considering actuator and state constraints using methods of optimal control," in *American Control Conference (ACC)*, 2013.

[53] Rao, A. V., Benson, D. A., Darby, C., Patterson, M. A., Francolin, C., Sanders, I., and Huntington, G. T., "Algorithm 902: Gpops, a matlab software for solving multiple-phase optimal control problems using the gauss pseudospectral method," *ACM Transactions on Mathematical Software*, vol. 37, no. 2, p. 22, 2010.

[54] Ren, L., *Modeling and Managing Separation for Noise Abatement Arrival Procedures.* Sc.D. Dissertation, Massachusetts Institute of Technology, Department of Aeronautics and Astronautics, 2007.

[55] Ren, L. and Clarke, J.-P., "Separation analysis methodology for designing area navigation arrival procedures," *Journal of Guidance, Control, and Dynamics*, vol. 30, no. 5, pp. 1319–1330, 2007.

[56] Ren, L. and Clarke, J.-P., "Flight-test evaluation of the tool for analysis of separation and throughput," *Journal of Aircraft*, vol. 45, no. 1, pp. 323–332, 2008.

[57] Ren, L. and Clarke, J.-P., "Modeling and simulating wind variation between flights for continuous descent arrival implementation," in *AIAA Modeling and Simulation Technologies Conference and Exhibit*, 2008.

[58] Ren, L., Ho, N. T., and Clarke, J.-P., "Workstation based fast-time aircraft simulator for noise abatement approach procedure study," in *AIAA Aviation Technology, Integration and Operations Conference*, 2004.

[59] Reynolds, T. G., R. L. C. J.-P. B. B. A. S. and Green, M., "History, development and analysis of noise abatement arrival procedures for uk airports," in *AIAA Aviation, Technology, Integration and Operations Conferences*, 2005.

[60] Reynolds, T. G., Ren, L., and Clarke, J.-P., "Advanced noise abatement approach activities at nottingham east midlands airport, uk," in *7th USA-Europe Air Traffic Management R&D Seminar*, 2007.

[61] Ross, I. M. and Fahroo, F., "Pseudospectral methods for optimal motion planning of differentially flat systems," *IEEE Transactions on Automatic Control*, vol. 49, no. 8, 2004.

[62] Schultz, R. L., "Three-dimensional trajectory optimization for aircraft," *Journal of Guidance, Control, and Dynamics*, vol. 13, no. 6, 1990.

[63] Slattery, R. and Zhao, Y., "Trajectory synthesis for air traffic automation," *Journal of Guidance, Control, and Dynamics*, vol. 20, no. 2, 1997.

[64] Sorensen, J. A. and Waters, M. H., "Airborne method to minimize fuel with fixed time-of-arrival constraints," *Journal of Guidance, Control, and Dynamics*, vol. 4, no. 3, 1981.

[65] Sprong, K., Klein, K., Shiotsuki, C., Arrighi, J., and Liu, S., "Analysis of aire continuous descent arrival operations at atlanta and miami," in *IEEE/AIAA 27th Digital Avionics Systems Conference*, 2008.

[66] Swenson, H. N., Hoang, T., Engelland, S., Vincent, D., Sanders, T., Sanford, B., and Heere, K., "Design and operational evaluation of the traffic management advisor at the fort worth air route traffic control center," in *1st USA/Europe Air Traffic Management R & D Seminar*, 1997.

[67] Tomlin, C., Pappas, G., and Sastry, S., "Conflict resolution for air traffic management: A study in multiagent hybrid systems," *IEEE Transactions on Automatic Control*, vol. 43, no. 4, pp. 509–521, 1998.

[68] Tong, K.-O., S. E. G. B.-D. A. S. J. and Haraldsdottir, A., "Descent profile options for continuous descent arrival procedures within 3d path concept," in *26th Digital Avionics Systems Conference*, 2007.

[69] Visser, H. G. and Wijnen, R. A., "Optimisation of noise abatement arrival trajectories," *Aeronautical Journal*, vol. 107, no. 1076, pp. 607–616, 2003.

[70] Wardi, Y., E. M. and Twu, P., "A controlled-precision algorithm for mode-switching optimization," in *51st IEEE Conference on Decision and Control (CDC)*, 2012.

[71] Wardi, Y., Twu, P., and Egerstedt, M., "On-line optimal timing control of switched systems," in *49th IEEE Conference on Decision and Control (CDC)*, 2010.

[72] Williams, D. H. and Green, S. M., “Airborne four-dimensional flight management in a time-based air traffic control environment,” *NASA Technical Memorendum 4249*, 1991.

[73] Wu, D. and Zhao, Y., “Optimization and sensitivity analysis of climb and descent trajectories for reducing fuel burn and emissions,” 2011.

[74] Xu, X. and Antsaklis, P., “Optimal control of switched systems based on parameterization of the switching instants,” *IEEE Transactions on Automatic Control*, vol. 49, no. 1, pp. 2–16, 2004.

[75] Zhao, Y. and Slattery, R. A., “Capture conditions for merging trajectory segments to model realistic aircraft descents,” *Journal of Guidance, Control, and Dynamics*, vol. 19, no. 2, pp. 453–460, 1996.

[76] Zhao, Y. and Tsiotras, P., “Analysis of energy-optimal aircraft landing operation trajectories,” *Journal of Guidance, Control, and Dynamics*, 2013.

[77] Zhao, Y. and Tsiotras, P., “Time-optimal path following for fixed-wing aircraft,” *Journal of Guidance, Control, and Dynamics*, vol. 36, no. 1, pp. 83–95, 2013.